

INTEGRATION OF FERROMAGNETIC METALS IN VERTICALLY ALIGNED NANOSTRUCTURES FOR SPINTRONICS

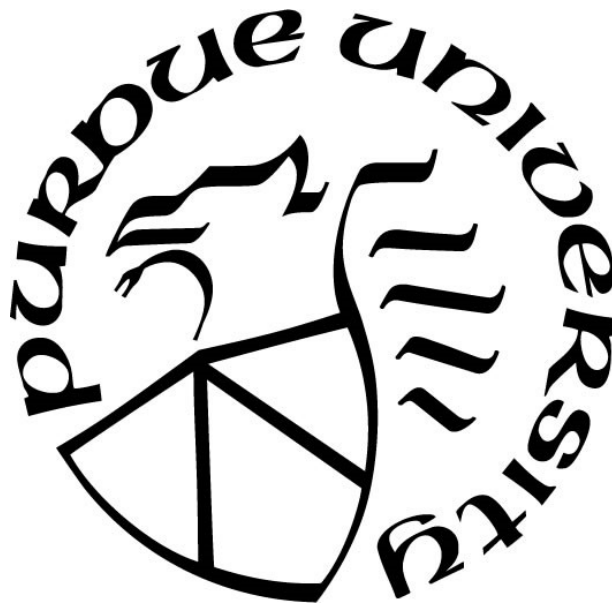
by
Bruce Zhang

A Dissertation

Submitted to the Faculty of Purdue University

In Partial Fulfillment of the Requirements for the degree of

Doctor of Philosophy



School of Electrical and Computer Engineering

West Lafayette, Indiana

August 2020

THE PURDUE UNIVERSITY GRADUATE SCHOOL
STATEMENT OF COMMITTEE APPROVAL

Dr. Haiyan Wang, Chair

School of Electrical and Computer Engineering
School of Material Science Engineering

Dr. Zhihong Chen

School of Electrical and Computer Engineering

Dr. Elliot B. Slamovich

School of Material Science Engineering

Dr. Peide Ye

School of Electrical and Computer Engineering

Approved by:

Dr. Dimitrios Peroulis

Dedicated to my friends and family.

ACKNOWLEDGMENTS

I would first like to thank my graduate advisor, Prof. Haiyan Wang, for her guidance and mentorship through my Ph. D. program. I benefited greatly from her enthusiastic approach to research and her infectious energy. These traits were able to rub off on me as I strove to complete my Ph. D. curriculum. She always encouraged and mentored me to complete my research ideas and provided a supportive environment which was conducive for me to complete my projects and to pursue my research ideas. Lastly, as I finish my Ph. D. program, I am extremely grateful for the advice and guidance that Prof. Wang gave me to both complete my thesis and to begin my professional career.

I also want to thank my committee members, Prof. Zhihong Chen, Prof. Elliot Slamovich, and Prof. Peide Ye, for their help in guiding my research projects. It was their input during our meetings that strove me to better my research project and research direction. Additionally, I would like to thank Dr. Aiping Chen, for guiding me during my time at Los Alamos National Lab. His guidance and encouragement were helpful in shaping my research direction and research views.

I would also like to thank my colleagues in Prof. Haiyan Wang's group for their support and their fruitful discussions: Dr. Jijie Huang, Dr. Jie Jian, Dr. Xingyao Gao, Dr. Zhimin Qi, Dr. Han Wang, Dr. Xing Sun, Dr. Leigang Li, Matias Kalaswad, Bethany Rutherford, Xin Li Phuah, Di Zhang, Dr. Shikhar Misra, Dr. Xuejing Wang, Zihao He, Juncheng Liu, Robynne Paldi, Juanjuan Lu, and Hongyi Dou.

Finally, I would like to thank my family for their love and supported through my entire education. I would also like to thank both the many friends that I made at Purdue and my friends at other places for their support and help. Lastly, I would like to thank my old college roommates for the many late-night conversations that were conducive to completing my Ph. D.

TABLE OF CONTENTS

LIST OF FIGURES	8
NOMENCLATURE	12
ABSTRACT.....	13
1. INTRODUCTION	14
1.1 Magnetism.....	15
1.1.1 Overview of Magnetism	15
1.1.2 Diamagnetism	16
1.1.3 Paramagnetism.....	17
1.1.4 Antiferromagnetism.....	17
1.1.5 Ferrimagnetism	17
1.1.6 Ferromagnetism	18
1.1.7 Exchange Bias	19
1.2 Magnetic Anisotropy	20
1.1.2 Overview of Magnetic Anisotropy	20
1.1.3 Magnetocrystalline Anisotropy	20
1.1.4 Stress Anisotropy	21
1.1.5 Shape Anisotropy.....	21
1.3 Magnetoresistance.....	22
1.1.6 Overview of Magnetoresistance	22
1.1.7 Colossal Magnetoresistance.....	22
1.1.8 Giant Magnetoresistance	24
1.1.9 Tunnel Magnetoresistance	25
1.4 Ferroelectricity	25
1.5 Tunnel Junctions	27
1.1.10 Ferroelectric Tunnel Junctions	27
1.1.11 Magnetic Tunnel Junctions	28
1.1.12 Perpendicular Tunnel Junctions	29
1.1.13 Multiferroic Tunnel Junctions.....	30
1.6 Optical Materials.....	30

1.1.14	Classification of Optical Materials.....	30
1.1.15	Metamaterials	31
1.1.16	Electromagnetic metamaterials	31
1.1.17	Hyperbolic Materials	32
1.1.18	Plasmonic Materials	34
1.7	Magneto-optical Coupling Effects	35
1.1.19	Faraday Effect	36
1.1.20	Magneto-Optic Kerr Effect	36
1.1.21	Plasmon-Enhanced Magneto-Optical Materials.....	37
1.8	Fabrication Approaches for Magnetic and Optical Nanostructures.....	37
1.1.22	Top-Down Fabrication	37
1.1.23	Bottom-Up Fabrication	38
1.9	Vertically Aligned Nanocomposites	39
1.1.24	Oxide-Oxide Vertically Aligned Nanocomposite	39
1.1.25	Metal-Oxide Vertically Aligned Nanocomposite	40
1.1.26	Selection Criteria and Growth Mechanisms for VANs.....	42
1.1.27	Three Phased VAN Systems	43
2.	EXPERIMENTAL METHODOLOGY.....	45
2.1	Pulsed Laser Deposition	45
2.2	X-ray Diffraction	46
2.3	Physical Property Measuring System and Magnetic Property measuring System	47
2.4	Transmission Electron Microscopy	48
2.5	Absorption Spectrophotometer	49
2.6	Magnetoelectro Coupling.....	49
2.7	Angular Dependence Ellipsometry	50
2.8	Atomic Force Microscopy	50
3.	RESEARCH CHALLENGES AND FUTURE DIRECTIONS	52
4.	TUNABLE MAGNETIC ANISOTROPY OF SELF-ASSEMBLED FE NANOSTRUCTURES WITHIN A LSFO MATRIX	54
4.1.	Summary.....	54
4.2.	Introduction	54

4.3.	Experimental.....	56
4.4.	Fe:LSFO Growth and Characterization.....	56
4.5.	Fe:LSFO Ferromagnetic Characterization	62
4.6.	Conclusion.....	63
5.	TUNING MAGNETIC ANISOTROPY IN CO-BZO VERTICAL ALIGNED NANOCOMPOSITES FOR MEMORY DEVICE INTEGRATION	64
5.1	Summary.....	64
5.2	Introduction.....	64
5.3	Experimental	67
5.4	Co-BZO Nanostructure Characterization	69
5.6	Co-BZO Multilayer Magnetoresistance Change	76
5.7	Conclusion	77
6.	TUNABLE, ROOM TEMPERATURE MULTIFERROIC FE-BATIO3 VERTICALLY ALIGNED NANOCOMPOSITE WITH PERPENDICULAR MAGNETIC ANISOTROPY	78
6.1	Summary	78
6.2	Introduction.....	78
6.3	Methods and experimental.....	80
6.4	Results and discussion	81
6.5	Conclusions.....	91
7.	AU ENCAPSULATED FE NANORODS WITH TUNABLE MAGNETIC OPTIC PROPERTIES.....	92
7.1	Summary	92
7.2	Introduction.....	92
7.3	Experimental	94
7.4	Discussion.....	96
7.5	Conclusion	105
8.	PRESENT AND FUTURE WORK.....	108
	REFERENCES	110
	VITA.....	134

LIST OF FIGURES

Figure 1.1 Electron spinning around the atom is the origin of the atomic magnetic moment[16].	15
Figure 1.2 Schematic demonstrating how different types of magnetic material react to an applied magnetic field[18].	16
Figure 1.3 Schematic showing the band splitting and elongation of the Mn-O bonds[46].	22
Figure 1.4 Normalized resistances of the Fe/Cr layers[52].	24
Figure 1.5 The double well free energy graph as a function of polarization calculated via using Laudau-GinzBurg-Devonshire theory, with two minima shown[59].	26
Figure 1.6 Tunnel junctions and the different resistive levels based on the switching direction for a) magnetic tunnel junctions, b) ferroelectric tunnel junctions, and c) multiferroic tunnel junctions[11].	27
Figure 1.7 Schematic demonstrating how the polarity direction of the ferroelectric alters the barrier height[60].	28
Figure 1.8 Schematic of the setup for the perpendicular magnetic junction. b) Top view of the magnetic tunnel junction taken using scanning electron microscopy[66].	29
Figure 1.9 Schematic demonstrating the equifrequency surface when the dielectrics in one direction is negative, resulting in the hyperbolic classification[83].	32
Figure 1.10 Schematics demonstrating the a) metal-dielectric stack, and b) metal nanopillars in a dielectric matrix with the darker blue being the metal and lighter blue being the dielectric.	33
Figure 1.11 The different configurations of MOKE are utilized.	36
Figure 1.12 HAADF image of the Fe nanopillars within the LSFO matrix. b) The out-of-plane and in-plane magnetic response of the film with c) coercive field tuning via thickness control[136].	41
Figure 1.13 Epitaxial Paradigm illustrating how strain compensation can be utilized to grow VAN films[141].	42
Figure 1.14 STEM and EDX images of the three phased growth with ZnO and Au grown within a BTO matrix[144].	43
Figure 2.1 Schematic set-up for a pulsed laser deposition[145].	45
Figure 2.2 Schematic demonstrating the electron diffraction caused by atoms[146].	46
Figure 2.3 Schematic demonstrating the difference between how the electron beam arrives at the sample for TEM and STEM[147].	48
Figure 2.4 Schematic of the typical setup of an ellipsometer[148].	50

Figure 4.1 Phase identification of metal-ceramic LSFO:Fe films grown at 5 Hz. (a) X-ray diffraction (XRD) h-2h patterns of the LSFO:Fe film grown at different deposition energies showing the presence of Fe (110) peaks. (b) Magnified XRD h-2h patterns centered around the Fe (110) peak displaying the peak shift.	56
Figure 4.2 Phase and composition demonstration of the LSFO:Fe film grown at 2 Hz. (a) Typical cross-sectional STEM HAADF image of the LSFO:Fe exhibiting Fe nanostructures within the oxide matrix. (b) Fe and (c) La atomic scale EDS elemental maps confirming metal within the oxide matrix.	58
Figure 4.3 Typical (a) plan-view and (b) cross-sectional TEM image of the metal-ceramic thin film grown at 2 Hz. These images clearly show the uniform distribution of the Fe nanostructures within the oxide matrix.	59
Figure 4.4 (a-c) Cross-sectional and (d-f) plan-view TEM images of Fe nanostructures within ceramic matrix grown at 5 Hz and different energies of 300 mJ, 400 mJ, and 450 mJ, respectively. (g-i) Diameter distribution of the Fe nanostructures within the oxide matrix.	60
Figure 4.5 Room-temperature (a) In-plane and (b) out-of-plane magnetic hysteresis loops of the metal-ceramic thin films deposited at different energies. (c) Plot of magnetizations along both in-plane and out-of-plane and deposition energies showing the relationship between the magnetic anisotropy and deposition energy.	61
Figure 5.1 Schematic showing the different thicknesses investigated to determine how thickness and, in extension, aspect ratio between the thickness of the film and diameter of the Co pillars affect the physical properties.	67
Figure 5.2 Typical θ -2 θ XRD scan of the different films deposited at different thicknesses with corresponding schematic to illustrate the aspect ratio.	69
Figure 5.3 Nanostructure study of the Co-BZO samples grown at different thicknesses. a-c. TEM images of the 4 nm, 20 nm, and 35 nm thick samples verifying the thicknesses. d-f) STEM images of the 4 nm, 20 nm, and 35 nm thick samples. g) Selected area electron diffraction (SAED) pattern of the 35 nm thick sample with a h) selected plan view area sample for the 35 nm thick sample. EDS images were taken with a i) Co spectrum map and an j) element map.	70
Figure 5.4 Magnetic study of the different films at a, b) low temperatures with in-plane and out-of-plane applied fields, and at c, d) room temperatures with in-plane and out-of-plane applied fields. Further plotting was done on the different coercive fields and magnetic saturations done for e) in-plane and f) out-of-plane applied magnetic fields at low and room temperatures.....	72
Figure 5.5 Nanostructure study of the device with an a) schematic of the device and its corresponding b) TEM image and c) STEM images. In addition, the d) HAADF was taken with the e-g) corresponding elemental mappings done.	74
Figure 5.6 Magnetoelectrical properties of the device with a a) M vs R with varying applied fields with its corresponding b) MR ratios. c) A schematic of how the spins align within the ferromagnetic layers as magnetic fields increase.....	75
Figure 6.1 a) Schematic demonstrating the proposed growth of Fe pillars within a BTO matrix. b) Schematic showing the different lattice parameters of BTO and Fe on STO. c) Typical θ -2 θ XRD	

scan of the different films deposited at different frequencies. d) The different lattice parameters for BTO and Fe grown at different frequencies..... 81

Figure 6.2 Schematic demonstrating the Fe-BTO film grown on STO. b-d) Plan view STEM images of Fe-BTO grown at 10 Hz. EDX mapping of the plan view images of Fe-BTO with e) O, f) Fe, and g) Ba mapping shown. h) GPA analysis of a single pillar to illustrate the strain distribution. i) and j) The STEM and Fe EDX mapping respectively of a cross-sectional view.. 83

Figure 6.3 Schematic demonstrating the how the pillar diameters vary with different frequencies. b, c, f, g, j, and k) Plan view TEM images demonstrating the pillar variation. d, h, and l) Histogram plots illustrating the nanopillar diameter distribution for the samples deposited under different laser frequencies. 85

Figure 6.4 a,b) Hysteresis loops of the Fe-BTO films grown at different frequencies with c and d) graphs magnifying the magnetic moments around the coercivities. e) Graph depicting the relationship between the coercivities for both in-plane and out-of-plane with deposition frequency. f) Different dielectric constants of the different frequencies as modeled using data from ellipsometer..... 87

Figure 6.5 a) Schematic of the multi-layer used to isolate the Fe regions within the film from the bottom conductor. b) TEM and c) STEM images of the multi-layer. d) and e) EDX mapping of the multi-layer with the f) ferromagnetic and g) ferroelectric properties. 89

Figure 6.6 Room temperature polarization vs applied magnetic field with the black line representing the linear fit for the data. 91

Figure 7.1a) Schematic demonstrating the growth of the Au-Fe-LSFO system. b) Typical θ - 2θ XRD scan of the different films deposited at different frequencies. c) A finer θ - 2θ XRD scan of the film between the 2θ values of 43 and 50° 95

Figure 7.2a) Schematic demonstrating the Au-Fe-LSFO film grown on STO. b-d) Plan view EDX mappings of the 5 Hz film with b) Fe and Au, c) Au, and d) Fe mappings shown. e, f) HRSTEM image of the 5 Hz Au-Fe-LSFO film with e) being plan view and f) being cross-sectional. g-i) Plan view EDX mappings of the 5 Hz film with g) Fe and Au, h) Fe, and i) Au mappings shown..... 97

Figure 7.3a, d, g) Plan-view TEM images of the different frequencies to demonstrate how the Fe pillars vary. Cross sectional b, e, h) TEM images and c, f, i) STEM images to better observe how the pillar structure vary with frequency. 99

Figure 7.4a, b) Low and c, d) room temperature hysteresis loops of the Fe-BTO films grown at different frequencies with magnified inserts for the room temperature loops..... 101

Figure 7.5a, b, c) Dielectric constants of the 2, 5, and 10 Hz sample modeled using data from the ellipsometer with the blue highlighting the hyperbolic region. d) Schematic demonstrating the polar and longitudinal directions of the MOKE measurements where the yellow is the light and the purple is the applied magnetic field direction. e) The MOKE readings for the polar and longitudinal directions for the 5 Hz measurement. 103

Figure 7.6 STEM and EDX images of Au-Fe-LSFO samples grown at a) 2 Hz and b) 10 Hz. . 106

Figure 7.7 STEM images of a) Fe-LSFO and b) Au-Fe-LSFO samples grown at 2 Hz at STO. 106

Figure 7.8 a, b, c) The measured reflectance data of the three different frequencies. d) The transmission data for the samples used to fit the model. 107

NOMENCLATURE

AFM	Antiferromagnetic
CMR	Colossal magnetoresistance
H _C	Coercive Field
T _C	Curie Temperature
DE	Double Exchange
EDX	Energy dispersive X-ray
FE	Ferroelectric
FM	Ferromagnetic
FTJ	Ferroelectric Tunnel Junction
GMR	Giant magnetoresistance
HAADF	High angle annular dark field
IP	In-plane
LSPR	Localized Surface Plasmon Response
MFTJ	Multiferroic Tunnel Junction
MR	Magnetoresistance
MPMS	Magnetic Measuring System
MTJ	Magnetic Tunnel Junction
OP	Out-of-plane
PLD	Pulsed laser Deposition
PM	Paramagnetic
PMA	Perpendicular magnetic anisotropy
PPMS	Physical Property Measuring System
M _R	Remnant magnetization
M _S	Saturation magnetization
STEM	Scanning transmission electron microscopy
TEM	Transmission electron microscopy
TMR	Tunnel magnetoresistance
VAN	Vertically aligned nanocomposites
VSM	Vibrating sample magnetometer
X _m	Magnetic Susceptibility

ABSTRACT

Vertically aligned nanocomposite (VAN) thin films are a promising thin-film platform that allows the combination of a highly desired material with another complementary oxide. Traditionally, VANs have been limited to combining an oxide with another oxide which has shown a wide range of functionality, and, by adjusting the different growth parameters, it has led to the tuning of their physical properties. While VANs have already shown to be an effective platform with immense potential, further enhancement of physical properties can be performed by replacing one of the oxides with a metal forming metal-oxide VANs.

In this dissertation, by the inclusion of the 3d transition metals, e.g., Fe and Co, into various oxide matrices, such as $\text{La}_{0.5}\text{Sr}_{0.5}\text{FeO}_3$, BaZrO_3 , and BaTiO_3 , strong, highly anisotropic, ferromagnetic properties have been achieved. By varying the growth parameters, tunable physical properties, mainly coercivity and anisotropic ratio, have been demonstrated. Furthermore, in the case of Co- BaZrO_3 , a multi-layer stack has been successfully grown and demonstrated a tailorable magnetoresistance. Additionally, a novel system by combining Fe pillars into a BaTiO_3 matrix has been demonstrated. This new system allows for the combination of the room temperature Fe ferromagnetic properties with the ferroelectric properties of BaTiO_3 , allowing for coupling between the two with coercivity tuning and tailorable ferromagnetic properties.

Lastly, it has been shown a possible framework by adding additional metals into the existing metal-oxide VAN platform. By adding the third phase, another metal, it opens up a new avenue to induce additional functionality while creating a method to introduce coupling between the different metals and physical properties.

1. INTRODUCTION

Magnetic materials have continued to attract considerable interests due to their wide range of applications such as memories [1,2], power electronics [3,4], sensors [5,6], etc. Magnets were first discovered in the ancient world with from the naturally occurring mineral called a lodestone which chemical composition consists of iron oxide. From suspending the lodestone, they were able to observe that the magnetism always point in one direction, leading to the first compasses[7]. It was not until much later in the late 18th century that the physics behind magnetism was more rigorously studied by notable figures such as Carl Gauss, Charles Coulomb, Hand Oersted, Michael Faraday, James Maxwell, Pierre Weiss, and many others, that led to our present-day understanding.

In a similar vein that magnetic materials have attracted considerable interest, ferroelectric materials have also attracted similar interest due to their wide range of applications[8]. Of recent interest however is integrating ferroelectric with ferromagnetic materials to produce a multiferroic system[9,10] creating additional avenues of control.

Next, a spintronic device that has been on the forefront of many different applications are tunnel junctions[11]. Tunnel junctions all operate utilizing resistive switching as the mechanism that caused the switching used to classify and identify different types of tunnel junctions. For these tunnel junctions, it is crucial to select the proper ferroelectric, ferromagnetic, or multiferroic materials to improve the performance of the device.

One possible classification of materials that can improve the performance of different spintronic devices are magneto-optical materials[12,13]. Magneto-optical are materials which combine optical and magnetic properties to create systems where magnetic fields can polarize light and where polarized light can affect magnetic fields. In order to create these materials though, specific structures must be made, which requires different fabrication techniques with each having advantages and disadvantages[14].

An interesting platform that have created novel ferromagnetic, ferroelectric, multiferroic, and magneto-optic films is Vertically Aligned Nanocomposites (VANs)[15]. VANs are a promising platform that grows highly anisotropic nanostructures via self-assembly which are further classified via the type of materials are used in the VAN. From these VAN, many different types of systems were created to address many different application and device needs.

The introduction will first cover a brief introduction to the mechanism of magnetism and the different classifications of magnetic materials and the different physical phenomena that are caused by these magnetic materials. In the second part, a brief introduction of ferroelectricity will be introduced, followed by an introduction to tunnel junctions with a brief overview on both the classifications and mechanisms. In the third part, optical materials and later, magneto-optical materials, are introduced with a short overview on the different fabrication techniques used to make these materials. Lastly, VANs are introduced with emphasis on both oxide-oxide and metal-oxide VANs.

1.1 Magnetism

1.1.1 Overview of Magnetism

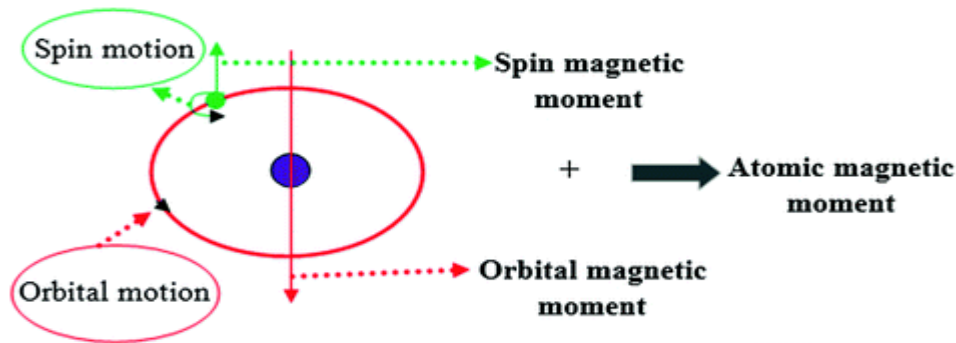
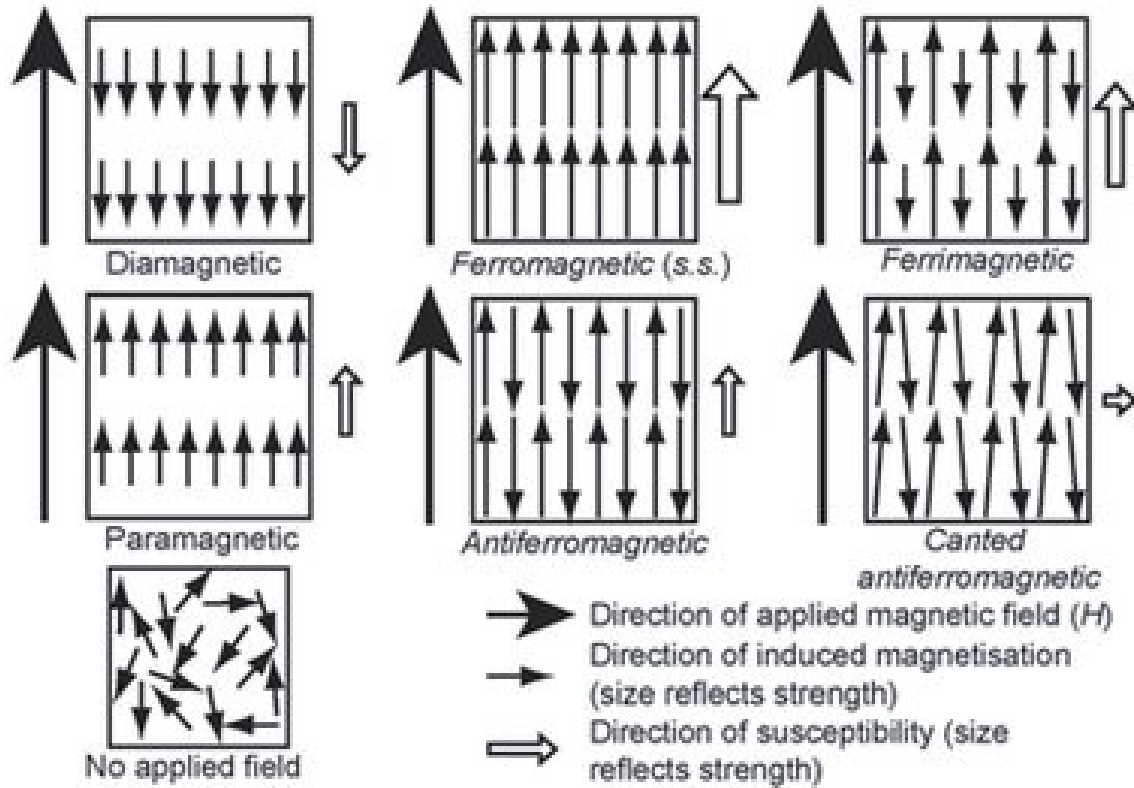


Figure 1.1 Electron spinning around the atom is the origin of the atomic magnetic moment[16].

Magnetism originates from the motion of the electron, or more specifically, the orbital spin and the orbital motion of the electron, as it travels around the nucleus. As the electrons orbit around the nucleus, the path they take act as solenoids causing a net magnetic moment to form. Although for most electron orbits, two electrons can fill one orbit with the electrons having opposite spins, thus resulting in a net zero magnetic moment. The magnetic material is classified into different categories based on its magnetic susceptibility, X_m , which is the ratio of the induced magnetization of the material to the applied magnetic field[17]. The different categories used to classify the materials are diamagnetic, paramagnetic, ferromagnetic, ferrimagnetic, and antiferromagnetic.



¹ Figure 1.2 Schematic demonstrating how different types of magnetic material react to an applied magnetic field[18].

1.1.2 Diamagnetism

The term diamagnetism was first coined by Faraday in 1845, where he found that magnetism was a universal part of matter[19]. Diamagnetism occurs when there are no unpaired electrons in a material, resulting in a less than zero X_m [20]. These electron pairs when exposed to an external magnetic field will distort the electrons resulting in a weak magnetic moment to be produced. However, this magnetic response will weakly oppose the applied magnetic field in a proportional fashion, causing a negative X_m . Since almost all materials will have paired electrons, this property will be present in all materials. Yet to be classified specifically as a diamagnetic material, the strongest magnetic response must be caused by this intrinsically weak diamagnetic property which occurs in certain materials as in bismuth[21] and antimony[22].

¹ Image reproduced with permission of the rights holder, Springer Nature.

1.1.3 Paramagnetism

Paramagnetism is one of the most common magnetic classification of inorganic materials. Paramagnetism comes from the existence of an unpaired electron in an energy level[23]. Since this electron is unpaired, the electron's movement will not be canceled out by another electron moving in the opposite direction. This imbalance results in the sole electron's spin being affected by an external magnetic field, resulting in a X_m above 0. For paramagnetic material, the magnetic response of the material will align in the same direction and increase linearly with the applied field, but once this external magnetic field is removed, the material will revert to a zero net magnetic moment[24]. Interestingly though, there is a subclass of paramagnetic materials called superparamagnetic materials. Superparamagnetism usually appear in ferrimagnetic or ferromagnetic nanoparticles that shrink below a certain size threshold[25]. Below this threshold, a single domain comprises the entire nanoparticle, causing the magnetism to fluctuate directions randomly due to temperature with the time between flips is referred as the Néel relaxation time[26].

1.1.4 Antiferromagnetism

In 1936, Nobel Prize winner Louis Néel, theorized an existence of two other magnetic phases called antiferromagnetic and ferrimagnetic[27]. Antiferromagnetic materials are a special case of materials which the neighboring electron spins will always be in opposite directions. The opposing directions will cancel out any net magnetic moment from the material in the absence of any magnetic field. When a magnetic field is applied, one of the spin directions may become stronger, resulting in a non-zero net magnetic moment. This material is sensitive to thermal fluctuations and have a temperature Néel temperature, T_N . Above this temperature, the thermal energy of the system can overcome the spin ordering in the electrons leading to the system becoming paramagnetic.

1.1.5 Ferrimagnetism

Ferrimagnetic material is similar to antiferromagnetic material in that there are opposing magnetic directions between neighboring electrons. The key difference between antiferromagnetic and ferrimagnetic is the magnitude of the magnetic directions are not equal. This results in a net magnetization to remain and this phenomenon can be seen in materials such as Fe_3O_4 [28]. This

critical difference causes some unique characteristics that is only present in ferrimagnetic materials. One characteristic, called magnetization compensation point, is when certain ferrimagnetic materials such as DyCo_5 , have a temperature below the Curie temperature, where the magnetic fields cancel out each other producing a net magnetic moment of zero[29]. Another characteristic, called angular momentum compensation point, is when the net angular momentum is at zero. When the net angular momentum is zero, there is no force that holds the magnetic direction in one specific direction. By having no preferred magnetic direction, this allows for the magnetic direction to be easily changed, resulting in potentially high frequency switching in these materials[30].

1.1.6 Ferromagnetism

Ferromagnetism is the most sought-after magnetic classification due to both their strength of their magnetism and their ability to remember magnetic moments resulting in permanent magnets. Ferromagnetism is similar to paramagnetism due to the tendency for both types of materials to align to an external magnetic field, but ferromagnetic materials differ in the mechanism to which the magnetic moments of the electrons align. For paramagnetic films, the alignment happens on an individual electron scale, while for ferromagnetic materials, groups of neighboring electrons, called magnetic domains, will align in the same direction and retain this direction. Thus, the material will remember the magnetic alignment even after the external magnetic field is reduced to zero up to a certain temperature. Of the ferromagnetic materials, the 3d transition metals, Ni, Co, Fe are among the magnets with the strongest dipole moments. This is due to them having unpaired electrons in their 3d orbitals, and it was found that the 3d orbitals are the least overlapping resulting more unpaired electrons when compared to other orbitals[31].

In the late 19th century, Pierre Curie discovered that temperature has an effect on the magnetization on different magnets, and he found that a certain temperature, the Curie temperature, T_C , the magnet ceases to act like a permanent magnet[32]. As the temperature increases, more thermal energy will be introduced into the ferromagnetic material system. As this thermal energy increases, it will arrive at the point, T_C , where the thermal energy will overcome the magnetic domains, resulting in only individual atom alignment as seen in paramagnetic films.

Ferromagnetic and ferrimagnetic materials are different from the other types, because even if the external magnetic field is removed, both types of materials are able to remember a magnetic

direction. The magnetic moment of the electrons will stay the same for an extended period until another external magnetic field or external force is applied. This degree of remembrance of the magnetic moment is generally classified by the hysteresis loop that can be plotted in a magnetic moment vs magnetic field or M-H graph. Generally, the hysteresis shape is classified by quantifying the magnetic saturation (M_s), magnetic remanence (M_r), and coercive field (H_c). Magnetic saturation is the value of the magnetic moment when every magnetic domain within the material is aligned to the applied direction. This value will depend on intrinsic qualities of the material with the transition 3d metals, such as Fe, Ni, and Co having the strongest magnetic values of all the elements. Magnetic remanence is the magnetic moment that is left after the external magnetic field is removed. This value is usually determined by the material's inherent characteristics. Coercive field is the magnitude of an external magnetic field applied in the opposite direction to zero out the remembered magnetic moment. The magnitude of the coercive field often is determined by the domain sizes, whereas the large domains will exhibit larger coercive field, and smaller domains will exhibit smaller coercive fields.

There are two different classifications of ferromagnetic materials that depend on the strength of their respectively coercivity: hard and soft. Hard ferromagnetic materials have long been used in permanent memory storage due to their ability to retain a magnetic direction for extended periods without any additional energy input, only requiring energy to change the memory state or read the memory state[33]. Soft ferromagnetic materials are used in transformers due to their susceptibility to AC current allowing for more efficient switching[34]. This type of material is also largely sought out for their applications within ferromagnetic memory, especially MRAM[35], due to the requirement for these circuits to switch at high frequencies, thus lower coercivity will lead to lower energy requirements.

1.1.7 Exchange Bias

Exchange bias was first discovered by Meiklejohn and Bean in 1956 in partially oxidized cobalt nanoparticles, where the ferromagnetic cobalt regions were surrounded by the antiferromagnetic cobalt oxide[36]. They discovered that by applying a magnetic field while cooling from temperatures above the Néel temperature of the cobalt oxide causes the hysteresis loop of the cobalt to shift laterally and causes an increase in the coercivity. This phenomenon was named exchange bias. Generally, exchange bias is typically found at interfaces between soft

ferromagnetic and antiferromagnetic regions[37]. When the antiferromagnetic material is cooled with an applied magnetic field from above its Néel temperature, the spins within the antiferromagnetic will be aligned perfectly in an antiparallel fashion. This alignment will alter the direction of the ferromagnetic spins that are near the interface. At smaller magnetic fields, the ferromagnetic spins will align more readily with the spins of the antiferromagnetic film near the interface, causing a smaller magnetization required to shift into this alignment. On the opposite portion of the hysteresis, where the ferromagnetic direction opposes the antiferromagnetic alignment, more applied field will be needed. This is because in addition to the flipping the moment in the ferromagnetic, the antiferromagnetic magnetic spins will oppose this flipping. By opposing the flipping, it will require more magnetization due to having to overcome both the preexisting alignment within the ferromagnetic and the spin pinning caused by the antiferromagnetic[38]. These two mechanisms in conjunction with each other causes the shifts seen in the magnetic hysteresis plot.

1.2 Magnetic Anisotropy

1.1.2 Overview of Magnetic Anisotropy

For many magnetic materials, magnetic anisotropy can be seen in their magnetic behavior. Magnetic anisotropy is when different directions have different magnetic hysteresis loops. Generally, for magnetic anisotropy, there is an easy and hard direction for magnetic moment. The soft direction is the direction, generally out-of-plane or in-plane for crystalline material where the material is easily saturated i.e. has a smaller field required for saturation. The hard direction is the opposite direction, where the material is harder to be fully magnetized, i.e. have a larger field required to be saturated. There are different ways in which magnetic anisotropy can arise with from magnetocrystalline anisotropy, stress anisotropy, shape anisotropy, and exchange anisotropy.

1.1.3 Magnetocrystalline Anisotropy

Magnetocrystalline anisotropy is anisotropy that arises from the inherent crystal structure of the material causing energy differences in the easy and hard directions. Magnetocrystalline anisotropy depends greatly from the spin-orbital coupling which describes an electron spin interaction with an energy potential with certain electron orbitals having more energetically

preferred spin directions[39–41]. This preferred spin directions for the orbitals causes a difference in the hard and soft magnetic directions, in that for the soft directions, the preferred spin direction is in the same direction as the applied while for the hard direction, the preferred spin direction is normal to the applied field's direction. In a cubic system, the formula to calculate the magnetocrystalline anisotropy energy for a cubic structure is:

$$E = K_0 + K_1(\alpha_1^2\alpha_2^2 + \alpha_2^2\alpha_3^2 + \alpha_3^2\alpha_1^2) + K_2(\alpha_1^2\alpha_2^2\alpha_3^2) + .. \quad \text{Equation (1)}$$

Where the K_0, K_1, K_2, \dots , are the constants for a particular material at a given temperature, $\alpha_1, \alpha_2, \alpha_3$, are the cosines of the angle between M_s and the a, b, and c axis in the cubic system, respectively[42].

1.1.4 Stress Anisotropy

Stress anisotropy is magnetic anisotropy that arises from magnetostrictive material. Magnetostriction is the effect that applied magnetic fields have on the mechanical properties of a ferromagnetic or antiferromagnetic material. As a field is applied to a magnetostrictive material, the field will induce a mechanical stress to the material resulting in a length change. Inversely, if a mechanical stress is applied to a magnetostrictive material, the material will produce a magnetic field.

1.1.5 Shape Anisotropy

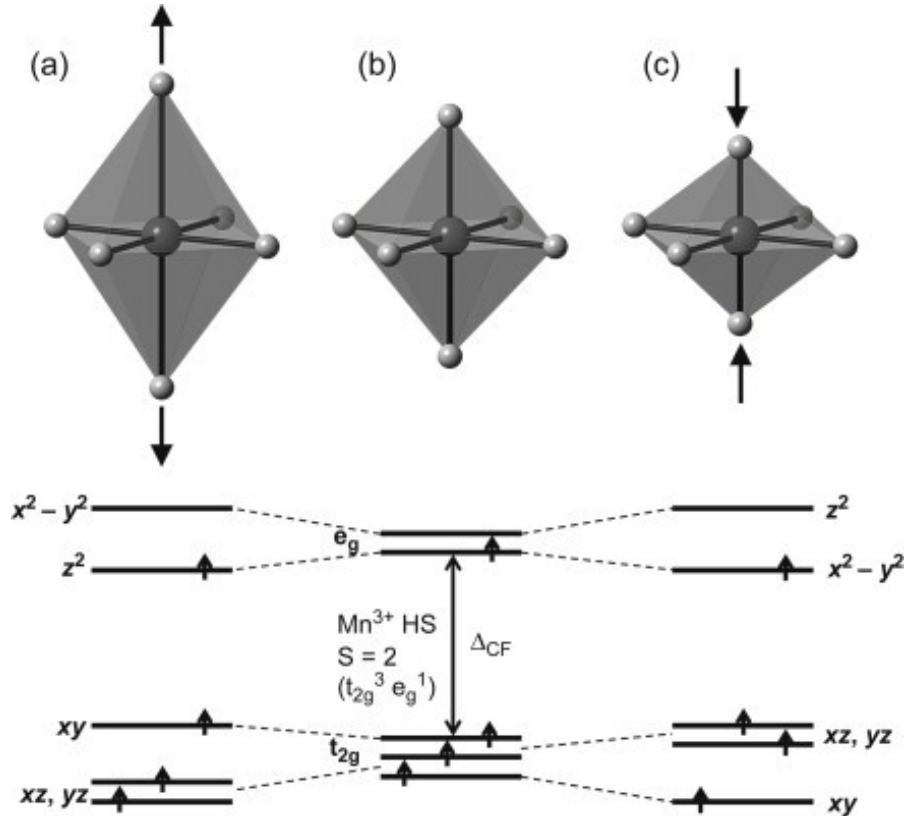
Shape anisotropy arises from dipole-dipole interactions[43]. In shape anisotropy, since not every magnet can be a perfect sphere, the overall shape of the magnet will cause a hard and easy direction to occur. This is most notable for thin films. For most single-phase epitaxial films, the in-plane coercive field will be much larger than the out-of-plane resulting in a soft out-of-plane direction and a hard in-plane direction. This is due to the geometry of the in-plane (parallel to the substrate) having a significantly larger dimension than the out-of-plane, and this shape anisotropy is extremely important for nanocomposite films, with the effect magnetic pillars embedded within a non-magnetic show been theoretically calculated to have a large shape anisotropy[44].

1.3 Magnetoresistance

1.1.6 Overview of Magnetoresistance

Magnetoresistance is when a material will change its resistance when exposed to an external magnetic field. This magnetoresistance was found by Lord Kelvin in 1856[45]. From There have been different types of magnetoresistance discovered since Lord Kelvin's initial discovery, and their classification of based on the underlying mechanism of how the electrons propagate through the material with the possible classifications of 1) colossal magnetoresistance 2) giant magnetoresistance 3) tunneling magnetoresistance.

1.1.7 Colossal Magnetoresistance

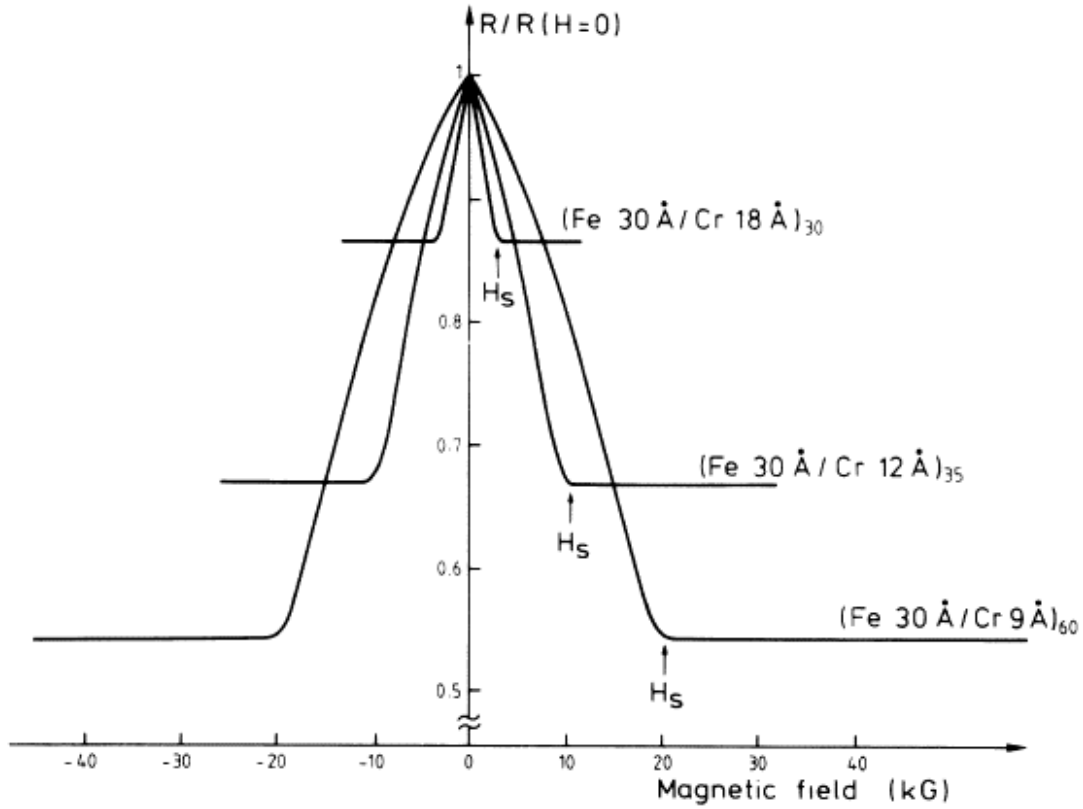


²Figure 1.3 Schematic showing the band splitting and elongation of the Mn-O bonds[46].

² Image reproduced with permission of the rights holder, Elsevier.

Colossal magnetoresistance is usually found in manganese-based perovskite oxides that is characterized by an immense decrease in their electrical resistance when an external magnetic field is applied near the ferromagnetic to paramagnetic transition point. The phenomenon was first discovered by G. H. Jonker and J. H. van Santen in the 1950s[47], and shortly after the double-exchange model was developed to explain the origin of the large change in magnetoresistance. In this model, it attributes the high resistance change to the jumping of electrons from a Mn^{3+} to Mn^{4+} facilitated by the jumping of e_g orbital electrons from Mn^{3+} to O p-orbital and at the same time an electron with the same spin jumping from O p-orbital to the now empty e_g orbital of Mn^{4+} . The applied magnetic field facilitates this jumping allowing for a change in resistivity[48]. However, the double exchange model does have its limitations, and recent work has been on to illuminate additional mechanisms that result in the resistance change[49–51].

1.1.8 Giant Magnetoresistance



³Figure 1.4 Normalized resistances of the Fe/Cr layers[52].

Giant magnetoresistance deals with the interaction between ferromagnetic layers separated by a thin non-magnetic metal. This phenomenon was first discovered by Nobel Prize winner A. Fert et al. in 1988 with Fe/Cr multilayers and Nobel Prize winner P. Grünberg et al. in Fe/Cr/Fe trilayers[52,53]. In the experiments, they found that two resistance states existed between the ferromagnetic layers. Since the middle layer is non-magnetic, the two surrounding ferromagnetic layers can be independently switched. When the spin alignment of the electrons within the ferromagnetic layers are parallel, a low resistance state exists, R_p , and when the spin alignment is antiparallel, a high resistance state exists, R_{ap} . The MR is calculated via the equation below:

$$GMR = \frac{R_{ap} - R_p}{R_p} * 100\% \quad \text{Equation (2)}$$

³ Image reproduced with permission of the rights holder, American Physical Society.

1.1.9 Tunnel Magnetoresistance

Tunnel magnetic resistance (TMR) typically is used to calculate the resistance switching exhibited in tunnel junctions (MTJ). There are three different type of tunnel junctions, ferroelectric, ferromagnetic, and multiferroic, with the classification being determined by what mechanisms causes the resistive switching[11]. MTJ consist of two ferromagnetic materials surrounding an insulating barrier. When the magnetic directions of the two ferromagnetic materials are in the same direction, it promotes electrons to tunnel through causing a “low” resistance state, R_p , and when the magnetic directions are biased in opposite directions, it hinders tunneling, causing a “high” resistance state, R_{ap} . The TMR is calculated via the equation below:

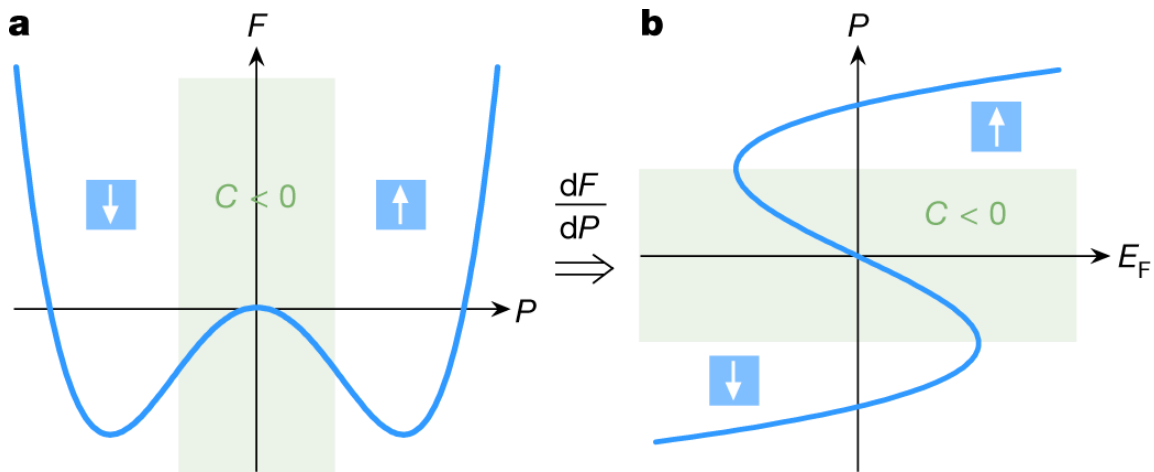
$$TMR = \frac{R_{ap}-R_p}{R_p} * 100\% \quad \text{Equation (3)}$$

The magnetic tunnel junction was first proposed by M. Julliere with a Fe/Ge-O/Co junction that exhibited a small TMR of only around 14% at 4.2 K, but nonetheless it was one of the first successful demonstrations of a tunnel junction[54]. Next, demonstrations of tunnel junctions that exhibited a non-zero, TMR at room temperature using aluminum oxide with TMR values of slightly larger than 10% were developed by T. Miyazaki in 1997[55]. As better fabrication techniques were developed, a main breakthrough that greatly benefited tunnel junction was the development of the growth of epitaxial, single-crystal, MgO[56].

1.4 Ferroelectricity

While magnetics have widespread use, ferroelectrics are also widely used in a variety of different devices and application. They are typically characterized as having a noncentrosymmetric crystal structure that enables spontaneous polarization[57]. Typically, some of the most well studied and widely utilized ferroelectrics are the perovskites. Perovskites are ideally identified by a chemical formula of ABO_3 where A and B are cations with A having a larger diameter than B, with examples being $BaTiO_3$ and $PbZr_xTi_{1-x}O_3$. The ferroelectricity derives from a combination of two different concepts, soft mode and the Landau-Ginzburg-Devonshire theory. In soft mode theory, the exhibited polarization comes from the instability of the lattice generated from its vibration due to temperature[58]. If the temperature decreases below a transition temperature, the

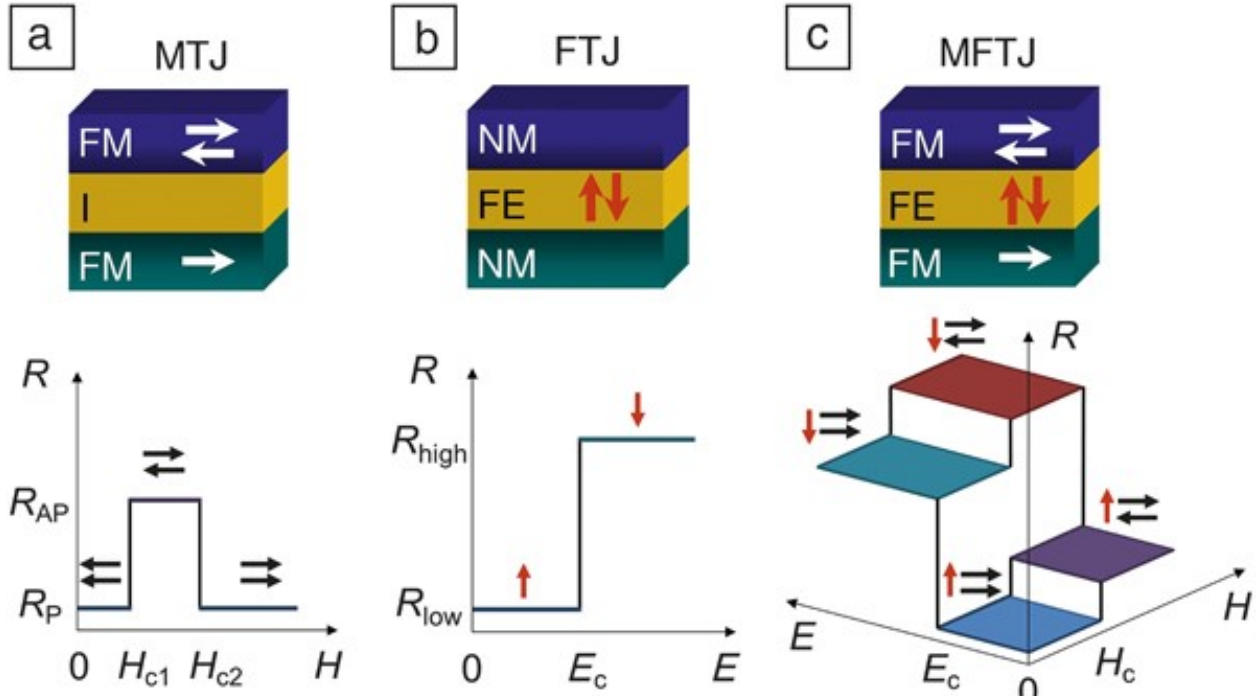
T_C , the B atom displacement is permanent, resulting in spontaneous polarization. Above this temperature, this property vanishes and turns the material into a paraelectric. As for the Landau-Ginzburg-Devonshire theory, at temperatures below the transition temperature, the free energy of the ferroelectric as a function of the polarization can be described as a double well. This double well has two energetic minimas corresponding to two different energetically stable spontaneous polarization states. In order to switch from one state to the other, energy will need to be added to the ferroelectric material to cause a polarization switch[59].



⁴Figure 1.5 The double well free energy graph as a function of polarization calculated via using Landau-Ginzburg-Devonshire theory, with two minima shown[59].

⁴ Image reproduced with permission of the rights holder, Springer Nature.

1.5 Tunnel Junctions



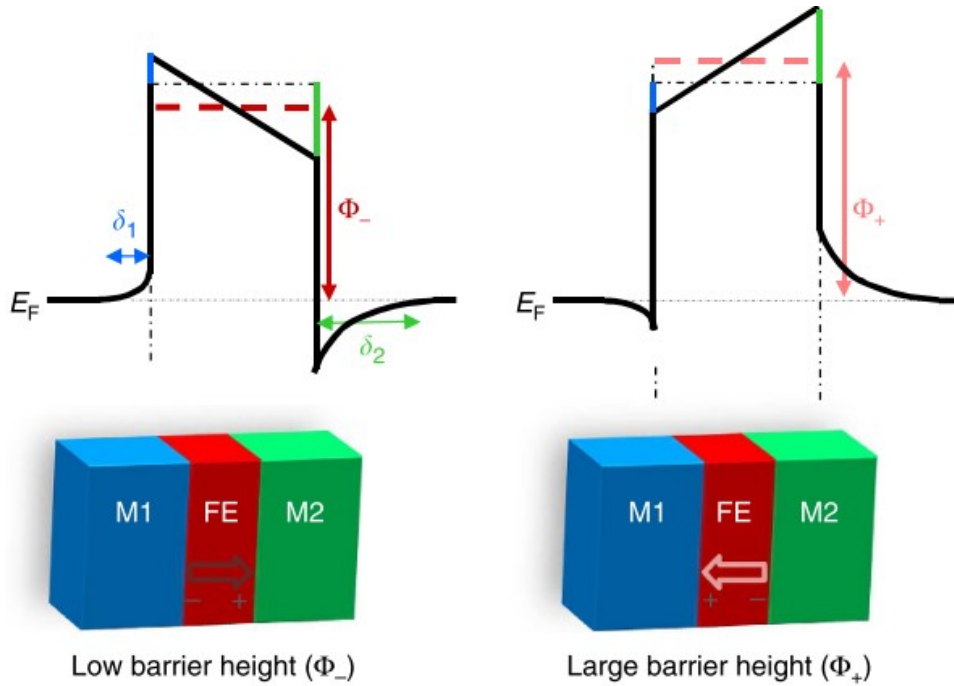
⁵Figure 1.6 Tunnel junctions and the different resistive levels based on the switching direction for a) magnetic tunnel junctions, b) ferroelectric tunnel junctions, and c) multiferroic tunnel junctions[11].

1.1.10 Ferroelectric Tunnel Junctions

One type of ferroelectric device is ferroelectric tunnel junctions. In FTJ, the layout typically is a ferroelectric material surrounded by a non-magnetic metal. In this device, the switching is performed via a middle ferroelectric layer that is able to switch polarization. By switching the polarization direction, the tunneling current will increase or decrease due to the ferroelectric barrier changing its work function, and thus the barrier height. As the barrier height decreases due to the polarization direction, the electrons have higher probability to tunnel through resulting in a higher current. While the other polarization direction will increase the barrier height, inhibiting the electron tunneling[60]. However, this is a simple explanation for the resistance variation, as other factors may contribute to the ratios between the two polarizations. One factor is that since the ferroelectrics will also be piezoelectric materials, the thickness of the barrier will change modulate with the applied voltage used to switch the polarization. Since the ferroelectric barrier thicknesses

⁵ Image reproduced with permission of the rights holder, Cambridge University Press.

are small to begin with, this modulation will influence the current across the ferroelectric, especially when a large read voltage is utilized[61].



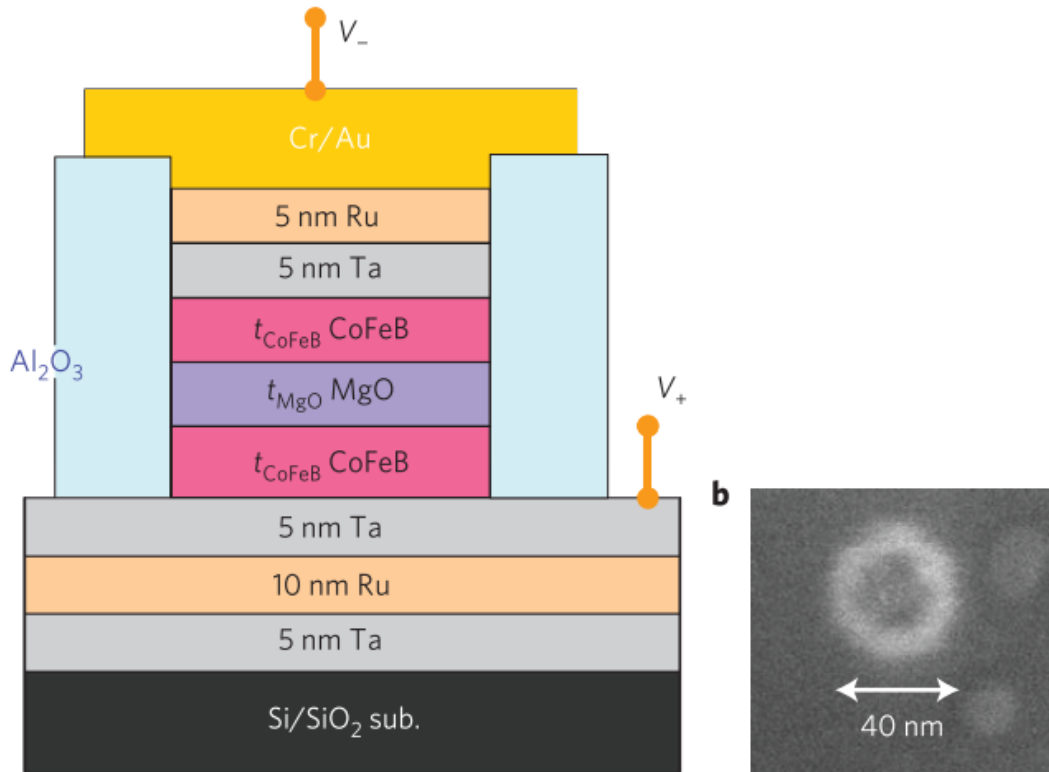
⁶Figure 1.7 Schematic demonstrating how the polarity direction of the ferroelectric alters the barrier height[60].

1.1.11 Magnetic Tunnel Junctions

In MTJ, the insulating layer between the ferromagnetic layers plays an essential role due to the fact the electrons need to tunnel through the layer. MgO was previously calculated to be able to create the tunnel junction structure of Fe/MgO/Fe with high switching behavior at room temperature by both J. Mathon and W.H. Butler in 2001 due to the unique band structure of MgO[62,63], and later that year, Bowen et al. was able to fabricate a Fe/MgO/FeCo device that demonstrated strong switching at room temperature with a TMR of above 60%[64]. Next, S. Yuasa made further improvements when the FeCo layer was replaced with Fe, resulting in even higher TMR of over 150% at room temperature[65]. These tunnel junctions though were all in the in-

⁶ Image reproduced with permission of the rights holder, Springer Nature.

plane direction with the layers growing directly on top of each other, but the next biggest breakthrough was when the ferromagnetic, switching layers had perpendicular anisotropy.



⁷Figure 1.8 Schematic of the setup for the perpendicular magnetic junction. b) Top view of the magnetic tunnel junction taken using scanning electron microscopy[66].

1.1.12 Perpendicular Tunnel Junctions

There is an ongoing preferential direction for perpendicular anisotropy because it allows for high density, low energy, and high frequency switching[67–69]. As the semiconductor industry keeps pursuing Moore’s law as a guideline for future technology, there comes an imperative need for high density electronics. As the density of devices increases, conventional semiconductor devices will consume more energy and radiate more heat resulting in substantial efficiency loss. To overcome this, a spin on the conventional in-plane MTJ must be developed. One of the first out-of-plane MTJ to be developed that showed promising room temperature properties was developed by H. Ohmori et al. where they grew TbFeCo/Fe/MgO/Fe/GdFeCo perpendicular MTJ

⁷ Image reproduced with permission of the rights holder, Springer Nature

that had a TMR of 64%[70]. Later, a perpendicular tunnel junction with a high TMR was developed by Ohno[66]. In this seminal work, Ohno developed a CoFeB/MgO/CoFeB MTJ with the CoFeB utilized as the ferromagnetic switching layers with additional metal layers to aide in the spin transfer. He found that below certain thicknesses, CoFeB switches from the usual preferred in-plane direction to out-of-plane and was able to successfully utilize this to grow a perpendicular MTJ. Using this design, he was able to successfully demonstrate a large perpendicular TMR of over 100 at room temperatures with thermal stability of CoFeB diameters of around 40 nm.

1.1.13 Multiferroic Tunnel Junctions

Multiferroic tunnel junctions (MFTJ) are a combination of the ferroelectric and magnetic tunnel junctions to create 4 resistive states. These four resistive states derive from the different combinations of ferromagnetic and ferroelectric orientations the switching materials can be in. There are two possible configurations that can result in the creation of this device. One of the common configurations is when the ferromagnetic materials, which are preferably conductive, surround a ferroelectric barrier[11]. In this configuration, the interface between the ferromagnetic and ferroelectric is important and crucial for the performance of the device. The less common configuration is a conductive electrode surrounds a multiferroic material. This configuration is less common, because multiferroic materials, in this case that are both ferromagnetic and ferroelectric are limited to few materials, and even less so at room temperature[71].

1.6 Optical Materials

Optical materials are utilized in a wide variety of applications[72]. Recently, the potential for these materials to improve the performance spintronic devices have been demonstrated, and there is ongoing work to both identify and create different optical, especially magneto-optical materials to improve device performance[73,74].

1.1.14 Classification of Optical Materials

Generally, there are two main classifications of materials, dielectric and metallic, that depend on the sign of the material's relative permittivity, ϵ_r . In the case of dielectric materials, the

ϵ_r of the materials will be positive. In these cases, the material will allow light to propagate through the material with the refraction of the light changing slightly based on the material's properties. Dielectric materials tend to be oxides or semiconductors in nature with some of the most well-known being materials such as SiO_2 , Al_2O_3 , BaTiO_3 , etc.

The other classification of materials, metallic, are materials that have a negative ϵ_r . In this case, the material will not allow light to propagate and instead the light will be reflected[75]. Metallic materials, as suggested by its name, are generally metals such as Au, Fe, Ni, etc. These two different classifications are broad and encapsulate nearly all known materials, yet by combining the two different properties of the classifications, interesting thin films and applications can be developed.

1.1.15 Metamaterials

Metamaterials are a classification of materials are artificially structured materials that give rise to properties not found in nature. Metamaterials were first proposed by Victor Veselago in 1967[76], where he proposed a theoretical material that will exhibit negative permittivity, ϵ , and negative permeability, μ . Prior to this publication, it has been largely accepted that the refractive index of materials can only be positive, yet in this paper he theoretically proves that the refractive index can have negative values. By having a negative refractive index, this will result in light entering a material to bend in an inside direction rather than the traditional outside direction. Next, Pendry first proposed the use of different artificial materials to achieve the negative index[77]. This led to the development and creation of a wide variety of metamaterials seen today. Now, metamaterials are widely used in a variety of different applications, with cloaking[78], superlens[79], and absorbers[80] being just a couple of application, with electromagnetic metamaterials being the most applicable to magnetic and optical applications.

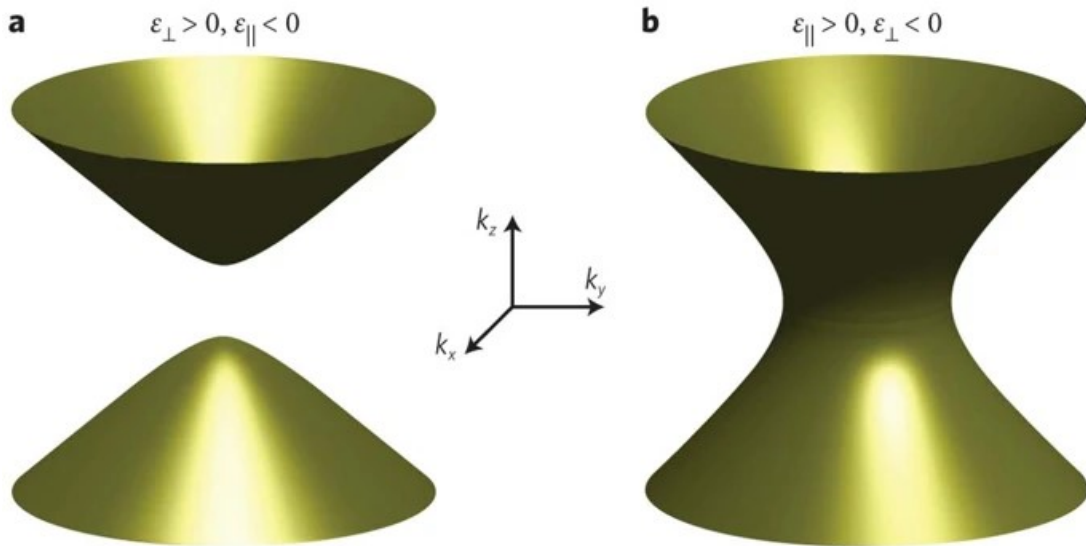
1.1.16 Electromagnetic metamaterials

Electromagnetic metamaterials are artificially made materials that can manipulate the electromagnetic waves. To classify the different number of metamaterials, the parameters of ϵ and μ are used with the different combination of signs of the parameters determining the classifications[81].

There are two possible classifications when the permeability, μ , is positive, based on the sign of ϵ . One is when $\epsilon > 0$, where the material is classified as dielectric, and the other is when $\epsilon < 0$, where the material is considered metallic. Now in the cases where the permeability is negative and the dielectric is positive, there exists natural materials called ferrites. In these ferrites, they exhibit negative permeability at low frequencies, but the magnetic properties fade away as the frequency increases to microwave regions[82]. The most interesting category, which this section will primary be discussing, is when the both the permeability and the dielectric is negative, .

When both μ and ϵ are negative, it indicates that it must be an artificial material since no natural material can have this combination of properties, and that the index of refraction is negative. Now this negative index of refraction is crucial in a variety of applications with some being perfect lenses, which allow for resolutions greater than $\lambda/2n$, perfect absorbers, which can absorb incident electromagnetic waves, and for switching and modulating electromagnetic waves[72]. One specific type of electromagnetic meta materials that have attracted considerable interest are hyperbolic materials.

1.1.17 Hyperbolic Materials



⁸Figure 1.9 Schematic demonstrating the equifrequency surface when the dielectrics in one direction is negative, resulting in the hyperbolic classification[83].

⁸ Image reproduced with permission of the rights holder, Springer Nature.

Hyperbolic materials are a type of metamaterial that is characterized by having highly anisotropic permittivity values, meaning that the out-of-plane and in-plane permittivity values differ greatly with one direction having a positive value and the other having a negative value[14]. This differs from metals in that in metals, all directions of the material have negative permittivity values, yet in hyperbolic material, this negativity is confined in one or two directions. This confinement of the negative permittivity is typically done by restricting the electron motion to these specific directions, which is why most of the hyperbolic materials have extreme geometric anisotropy. The most common structures that have been made into hyperbolic materials are layered metal-dielectric structures and nanowire arrays[83].

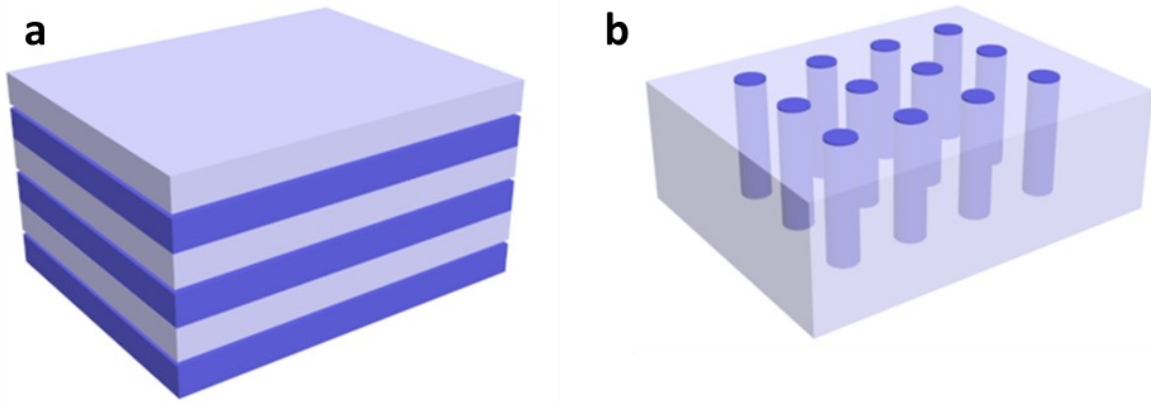


Figure 1.10 Schematics demonstrating the a) metal-dielectric stack, and b) metal nanopillars in a dielectric matrix with the darker blue being the metal and lighter blue being the dielectric.

Layered metal dielectric structures are multi-layer structures where a metal and dielectric are continuously stacked on top of each other. In this structure the effective dielectric tensors for parallel and perpendicular to the anisotropy axis is characterized by the equations[84]:

$$\epsilon_{\perp} = \frac{\epsilon_m d_m + \epsilon_d d_d}{d_m + d_d} \quad \text{Equation (4)}$$

$$\frac{1}{\epsilon_{\parallel}} = \frac{d_m/\epsilon_m + d_d/\epsilon_d}{d_m + d_d} \quad \text{Equation (5)}$$

where the ϵ_m and ϵ_d refers to the dielectric component of metal and dielectric, respectively and d_m and d_d stands for the thickness of the metal and dielectric layers, respectively. By manipulating the thicknesses and the material, it is possible to have one of the permittivity directions be negative

resulting in a hyperbolic material[85]. However, at certain wavelengths, the plasmonic response that appears at the interfaces between the metal and the dielectric may affect the index of reflection causing a positive index to occur. This structure has been fabricated in a variety of different systems that include Ag/Al₂O₃[86], Ag/TiO₂[87], and Au/Al₂O₃[88], etc[89,90].

Another common structure for hyperbolic materials is nanowire arrays. Nanowire arrays are when parallel metallic wires are embedded within a dielectric matrix, producing a hyperbolic metamaterial[91]. In this setup, the dielectric tensors for both the parallel and perpendicular to the length of the wire being[92]:

$$\epsilon_{\perp} = 1 \quad \text{Equation (6)}$$

$$\epsilon_{\parallel}(k_z) = 1 - \frac{\Omega_p^2}{\omega^2 - \delta^2 - c^2 k_z^2} \quad \text{Equation (7)}$$

where the $\Omega_p = c/a[\ln(a/2\pi R)/(2\pi) + 1/12]^{-1/2}$ and $\delta = \Omega_p a[\pi R^2(1 - \epsilon_{wire})]^{-1/2}$, where R refers to the wire radius, a refers to the period, and ϵ_{wire} is the dielectric constant for the material that composes the wire. By adjusting the radius of the wires, it will tune the dielectric constants, tuning the dielectric properties and by extension the hyperbolic transition points. This nanorod setup has shown promise in biosensors and optical fibers, because these the nanopillar structure have high sensitivity to the refractive index of a matrix, especially when compared to smooth metallic films[93,94].

1.1.18 Plasmonic Materials

Plasmonic materials have attracted recent interest due to their unique ability to modify density of states to create large density of states at select frequencies. The unique ability originates from the resonant oscillations of plasmons, a type of charge carriers, that are energetically excited by a light source, emitters, or thermal fluctuations. Furthermore, these oscillations can be tailored or controlled via changing the dimensions of the regions that interact with the electron plasma[95]. These materials are metallic in nature and have a negative permittivity, with Au and Ag being some of the most notable.

Surface plasmon resonance is a term that refers to electron resonant oscillations that occur between the interface of the metallic, or negative permittivity, and dielectric, or positive

permittivity[96]. When a light is shone on the interface, generally the metal will reflect most of the light back, but when the applied light's momentum and energy matches with the electrons at the interface, the electrons will start to resonant. This resonance will cause the light reflected to dip significantly, indicating surface plasmon resonance[97]. This technique and phenomena have applications in a variety of areas, with biosensors[98], and more recently fiber optics[99] being some of the most prominent.

Localized surface plasmon resonance is a specialized type of surface plasmon resonance has to generally deal with the interaction between a metallic nanoparticle and the surface plasmons[100]. Most commonly, Au and Ag are used for LSPR responses due to them being able to exhibit LSPR within the visible light spectrum. When the diameter of the metallic nanoparticles is below the wavelength of the incident light, the electrons at the surface and the light will interact forming coherent localized plasmon oscillations. These oscillations can be altered via changing the composition of the materials, the size and geometry of the nanoparticles, etc[101]. This phenomenon is useful in a variety of biosensor applications due to its ability to scatter light allowing for its usage in labeling of cells[102].

1.7 Magneto-optical Coupling Effects

Magneto-optical effects is when an electromagnetic wave that is traveling through a material is affected by a magnetic field. Magneto-optic effects have been discovered and documented since the 1840s[103], yet it was only in the recent decades that most of their applications have been developed with memory[104], sensors[105], microscopy[106], and spintronics[13] to name a few.

Light is an electromagnetic wave that can be polarized in two different directions, linearly, circularly, or elliptically polarized. When the light is linearly polarized, the light propagates in a single plane with the transverse electric field vector being perpendicular to the propagation direction. In an elliptically polarized light, the transverse electric field would be rotating in a plane perpendicular to the propagation forming a shape of an ellipse. Instead if the electric field magnitude remains constant while the rotation occurs, this will result in a circle and the light being circularly polarized. Two prominent magneto-optic effects that are well-studied and are of interest in a variety of fields are the Faraday Effect and Magneto-Optic Kerr Effect.

1.1.19 Faraday Effect

First discovered by Michael Faraday in 1845, Faraday was able to show that linearly polarized light can undergo a rotation of its polarization upon traversing through a medium that has an applied magnetic field applied along the axis of propagation[103]. The angle at which the polarization alters is proportional to the strength of the applied magnetic field and is modeled by the following equation.

$$\phi = V \int_0^l B \, dl = V l B \quad \text{Equation (8)}$$

Where ϕ is the angle of rotation, B is the magnitude of the magnetic field, l is the length of the sample, and V is the Verdet constant, which varies with the material of the medium, the temperature, and the wavelength of the light.

1.1.20 Magneto-Optic Kerr Effect

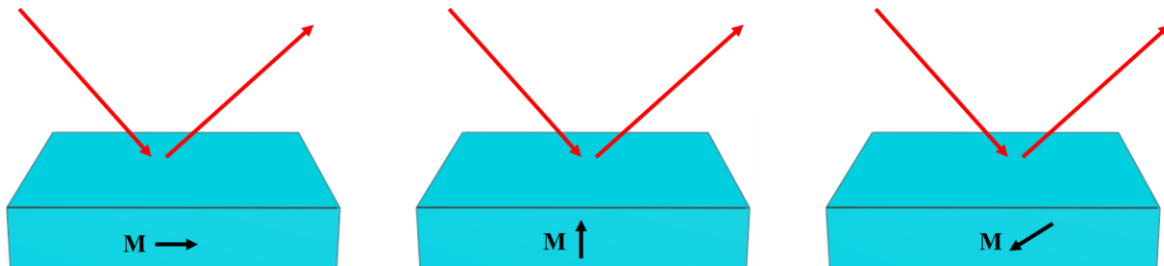


Figure 1.11 The different configurations of MOKE are utilized.

The Kerr effect was first discovered by John Kerr in 1875[107,108]. While the Faraday Effect alters the angle of polarity when light travels through a material, Magneto-Optic Kerr Effect is the change in polarization and reflected intensity when light is reflected from a magnetic material. This change in the angle of the polarization is proportional both the magnetic strength and the thickness of the material[109]. Generally, there are three different categories of MOKE that are characterized by the direction of the magnetization vector with respect to the surface of the reflecting material and the incident plane. Polar MOKE is when the magnetic field is perpendicular to the surface of the material and parallel to the incident plane. Longitudinal MOKE is when the magnetic field is parallel to the surface of the material and incident angle. Transversal MOKE is

when the magnetic field is the perpendicular to the incident plane and parallel to the surface of the material.

1.1.21 Plasmon-Enhanced Magneto-Optical Materials

Plasmon-enhanced magneto-optical materials and devices have been recently shown to great effect in a variety of different applications such as in magneto-plasmonic nanoantennas[110], detectors[111], and spintronic devices[112]. By using a plasmonic material, usually Au or Ag, with a magnetic material, it adds active control of the plasmons within the noble metals that can be manipulated. These materials show large magneto-optical properties that shows promise for ultrafast control of light that can be used for high frequency applications. One such study was performed by Dutta et al. in 2017 that showed that by designing and simulating a device that included a ferromagnetic and plasmonic layer, it was able to show a near one magnitude increase in performance due to the surface plasmon resonance and ferromagnetic coupling[74].

1.8 Fabrication Approaches for Magnetic and Optical Nanostructures

The fabrication of nanostructures is essential for a variety of magnetic and optical devices. These nanostructures generally improve performance and/or add additional functionalities due to their unique structure and design. By designing and fabricating a highly anisotropic nanostructure, such as nanopillars, it creates highly anisotropic physical properties. While perpendicular anisotropy is highly coveted, fabricating systems with them is a technical and engineering challenge. Generally, for the fabrication process, there are generally two different fabrication classifications, top-down and bottom-up, each having their own advantages and disadvantages[113].

1.1.22 Top-Down Fabrication

For today's IC's and devices, top-down fabrication and patterning is an essential tool. Top-down is typically when lithography and patterning is done after the different materials are grown. This fabrication method is widespread throughout the semiconductor industry and has shown precision in the case of fabricating devices such as MEMs[114], nanoantennas[115], and field

effect transistors[116]. Although there are numerous different ways to perform patterning and lithography, two of the most common are methods are optical lithography and e-beam lithography.

Optical lithography, one of the most utilized fabrication techniques in the semiconductor industry, was first introduced in the 1960s[117]. In optical lithography, light is focused through a quartz plate onto a photoresist covered wafer. Photoresists are typically a light sensitive polymer that reacts to the light in two different manners based on their classifications of negative or positive. In a positive photoresist, when light is exposed to the photoresist, the photoresist's solubility increases allowing for solution to remove the photoresist. On the other hand, for negative photoresists, when light is shone on the photoresist, the photoresist becomes cross-linked, resulting in the areas where light was not shone to be washed in away in a solution[118]. By developing the masks and the photoresists properly, it creates the necessary layouts for the devices and the wafers for current semiconductor technology. This allows for a wide range of variability, in that to change the layout of the wafer, it only requires the changing of the mask to the desired shape. By performing conventional optical etching, it is possible to create feature sizes down to 1 μm [119]. But as the demands for technology becomes more stringent, other engineering solutions were made. By including other optical apertures to focus the light and an additional mask, it was able to scale the resolution to even smaller resolutions of $<32\text{ nm}$ [120].

While optical lithography is commonly and widely used, another top-down fabrication technique that is widely utilized is e-beam lithography. Rather than the optical lithography that uses light to perform the patterning, e-beam uses electrons to perform the etching. This results in the e-beam lithography to not suffer from having to deal with the light diffraction index, helping to create smaller feature sizes within the nanometer range rather than the micron. Normally, the e-beam process occurs when an electron beam is applied to the surface of the wafer with the areas that are not to be etched covered by a photoresist. While this process is much more precise than conventional optical lithography, with feature sizes of around 40 nm being developed utilizing e-beam lithography, it suffers from the speed at which the etching occurs.

1.1.23 Bottom-Up Fabrication

Bottom-up fabrication, when the nanostructures is primary driven by the self-assembly and nucleation of the atoms, allows for smaller feature sizes than the top-down approaches. There are

numerous methods that are utilized for this type of growth but some of the more prominent growth methods are vapor phase deposition for ceramic thin films.

In vapor phase deposition, there are two different types based on how the vapor arrives, Physical Vapor Deposition and Chemical Vapor Deposition. Chemical Vapor Deposition involves the dissociation of gaseous reactants that react chemically together to form various structures. Of recent interest is the growth of ZnO nanostructures via using metal oxide chemical vapor deposition with various growth conditions[121,122]. In PVD methods, the materials are evaporated by a high energy source and the vapor travels to a substrate and deposits. By changing the different growth conditions and the concentration of the materials, it is possible to grow different structures that have much smaller feature sizes with some being ~10 nm large in both the PVD and CVD techniques[123,124]. This growth method allows for much smaller feature sizes that can be used in current day devices but currently have limitations in controlling the exact placement of the different nanostructures that the top-down technique does not.

1.9 Vertically Aligned Nanocomposites

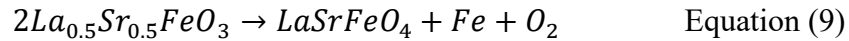
1.1.24 Oxide-Oxide Vertically Aligned Nanocomposite

Vertically aligned nanocomposites (VAN) are a bottom-up growth platform that allow for an unprecedented amount of anisotropy control and tuning of physical properties. VAN was first developed in 2002 by O. I. Lebedev when he grew a LCMO:MgO system[125]. VAN consists of multiple phases of different materials that are grown in a single step process, with the phases aligning in a vertical column manner. Of particular interest is the amount of vertical interface strain coupling that occurs between the different phases. By engineering the strain, it opens up new avenues for physical property tunability and property coupling. VAN that consists of two separate oxides have been developed with one phase typically containing a highly desired physical property with another oxide that allows for ideal strain matching and allows for highly desired anisotropic properties[126–134]. Strain matching is essential to selecting the proper phases and it has been reported and shown that when the strains of the different phases are in opposite directions; one tensile and one compressive, allows for more uniform and epitaxial VAN[135].

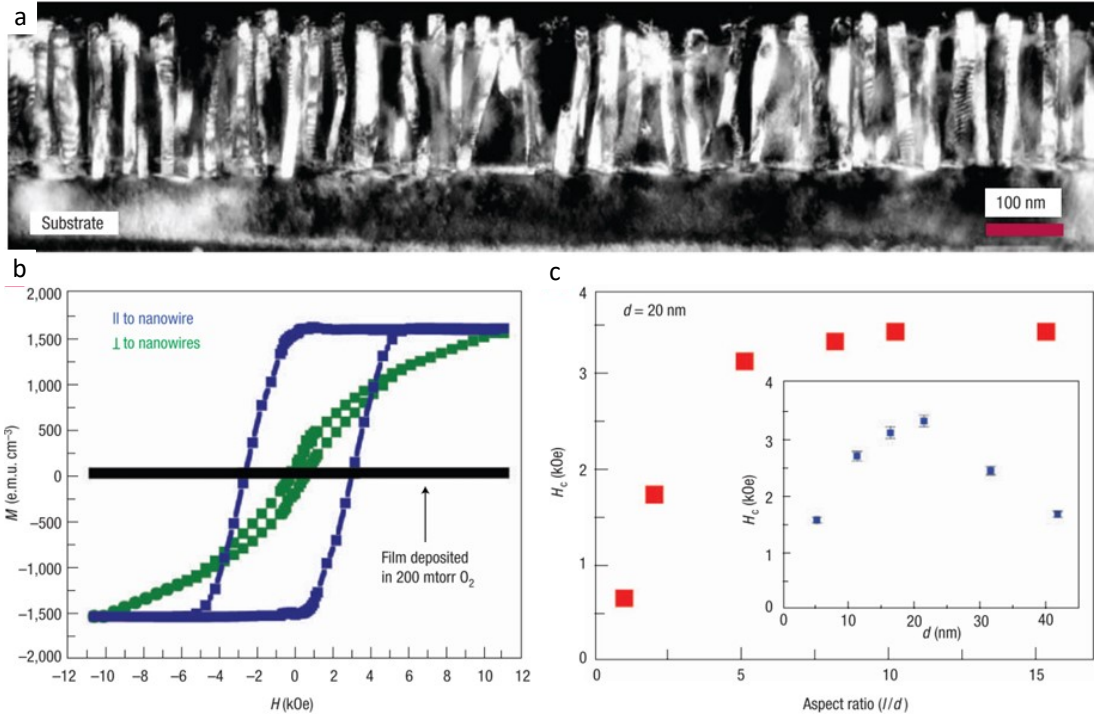
1.1.25 Metal-Oxide Vertically Aligned Nanocomposite

While oxide-oxide VAN allows for tunable physical properties, metals have one substantial advantage over oxides when it comes to their highly sought out room temperature properties. With most ferromagnetic oxide materials have a significantly lower T_C than room temperatures, it presents a pressing issue for integration into memory and devices. Electronic devices typically operate at temperatures above 30 °C, thus while oxide-oxide VAN does offer a plethora of advantages, this one disadvantage necessitates the metals to replace one of the oxide phases. In metallic VAN, one of the oxide phases will be replaced by a metal with desirable room temperature properties. The metals will then lead to strong room temperature properties with shape anisotropy induced by the unique vertical alignment of the VAN. These films typically exhibit strong out-of-plane anisotropic properties with a degree of ordering. For ferromagnetic materials, some of the most widely known materials for magnetic applications are the 3d transition metals of Ni, Co, and Fe. These metals are highly used due to their known high T_C 's and their strong intrinsic magnetic properties. Additionally, other widely sought metals such as Au have been integrated into VAN to introduce plasmonic properties into the VAN. VAN unique geometry allows for columns of metals to be grown. This results in shape anisotropy within the VAN system due to the length of the metals vastly exceeding the diameter.

One of the first reported metal VAN was Fe-LSFO. In this work, L. Mohaddes-Arbalili et al. was able to grow self-assembled Fe nanowires in a LSFO oxide matrix[136]. They were able to grow the material system utilizing a LSFO target in vacuum condition. In a vacuum condition, the redox reaction shown below occurred causing the formation of Fe (110) pillars from the LSFO target.



The resultant Fe pillars led to a vast improvement in the physical properties of the original LSFO system. It showed extremely strong, highly anisotropic, ferromagnetic response. Additionally, they were able to demonstrate a tunable coercive field by changing the thickness of the film.

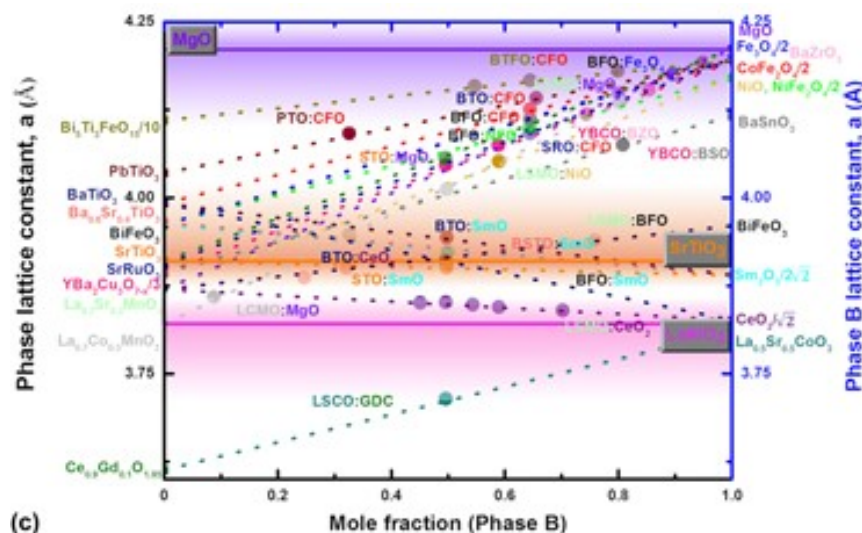


⁹Figure 1.12 HAADF image of the Fe nanopillars within the LSFO matrix. b) The out-of-plane and in-plane magnetic response of the film with c) coercive field tuning via thickness control[136].

Next, by incorporating the metal within the oxide in the target to make a single oxide with metal doping target led to a host of other highly desired ferromagnetic films such as Ni-CeO₂[137], Ni-Ba_{0.8}Zr_{0.2}Y₃[138], and Co-BaZrO₃[123]. Co-BaZrO₃. J. Huang et al. was able to grow regular Co pillars within BZO that showed regular density throughout the surface of the film. Additionally, he was able to show highly anisotropic, room temperature, ferromagnetic properties with a strong out-of-plane direction. Furthermore, by adjusting the frequency of the deposition, the diameter of the Co pillars was able to be tuned, which changes the coercivity of the ferromagnetic hysteresis. Not only has the integration of ferromagnetic metals with oxides in VAN has been demonstrated, other metals with highly desired properties has also been integrated, such as Au. Au is a well-known plasmonic material and it has been integrated into a variety of oxides such as Au-BaTiO₃[139] and Au-TiO₂[140]. In these systems, they were able to show optical tuning via changing the Au nanostructure shapes.

⁹ Image reproduced with permission of the rights holder, Springer Nature.

1.1.26 Selection Criteria and Growth Mechanisms for VANs



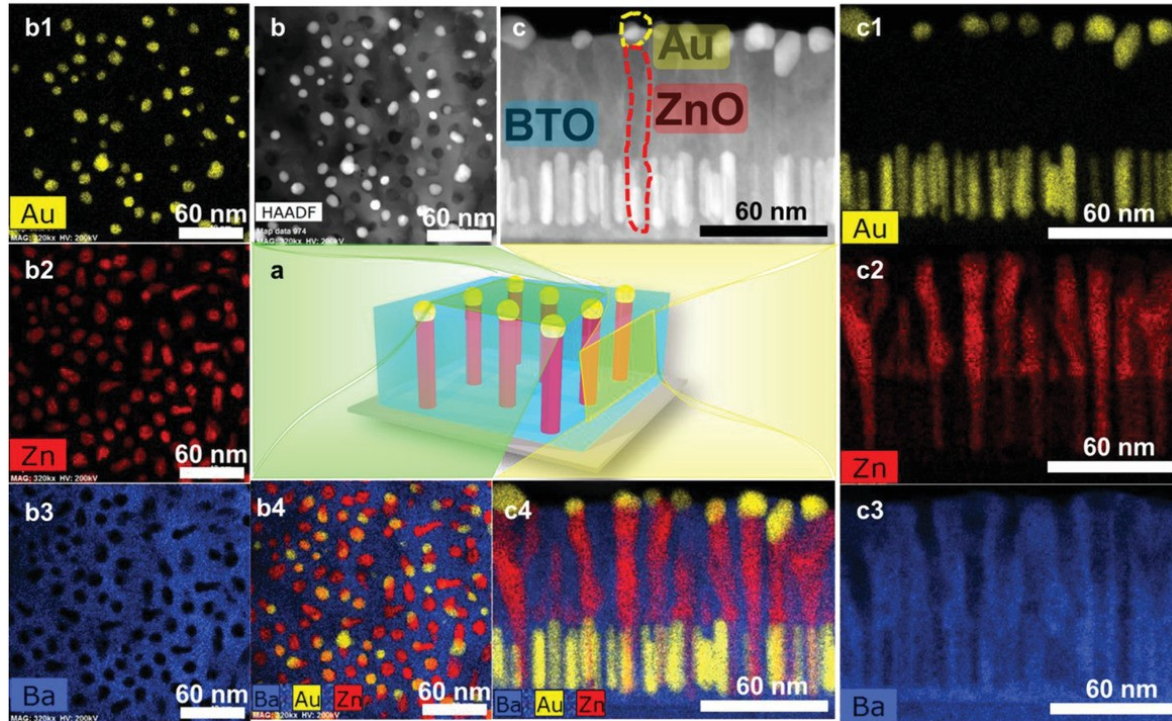
¹⁰Figure 1.13 Epitaxial Paradigm illustrating how strain compensation can be utilized to grow VAN films[141].

The growth of the VAN is a delicate balance between the nucleation and diffusion of the adatoms and the surface energy interactions between the different phases and the substrate. Generally, as mentioned in the strain compensation paradigm, strain is an indicator of what phases may grow into VANs with each other[142]. It is highly desirable to have the two phases be in opposite strain states with each other, with one being compressive and the other being tensile[135]. This strain dichotomy enables the two different phases to grow into ordered nanostructure with the interfacial strain used to compensate the differing strain state. While for oxide-oxide VAN this tends to be the case, for metal-oxide VAN the growth mechanism is typically more complex. The surface energy for metals and oxides tend to be greatly different, with metals such as Co, having a much lower surface energy than the oxides[123,143]. This results in two different growths modes when relating to the substrate. The metallic adatoms will clump together forming island growths due to their lower surface energy when compared to the oxide substrate. While the oxide adatoms, will grow in a layer growth, due to their similar surface energy values when compared to the substrate. This leads to the metal-oxide VAN forming an oxide layer with metal island growth causing the metal nanopillars to form. To ensure the pillars form correctly for both oxide-oxide

¹⁰ Image reproduced with permission of the rights holder, Cambridge University Press.

and metal-oxide VAN, careful consideration must be taken on selecting the phases and the substrates. This will lead to ordered pillar growth throughout the film.

1.1.27 Three Phased VAN Systems



¹¹Figure 1.14 STEM and EDX images of the three phased growth with ZnO and Au grown within a BTO matrix[144].

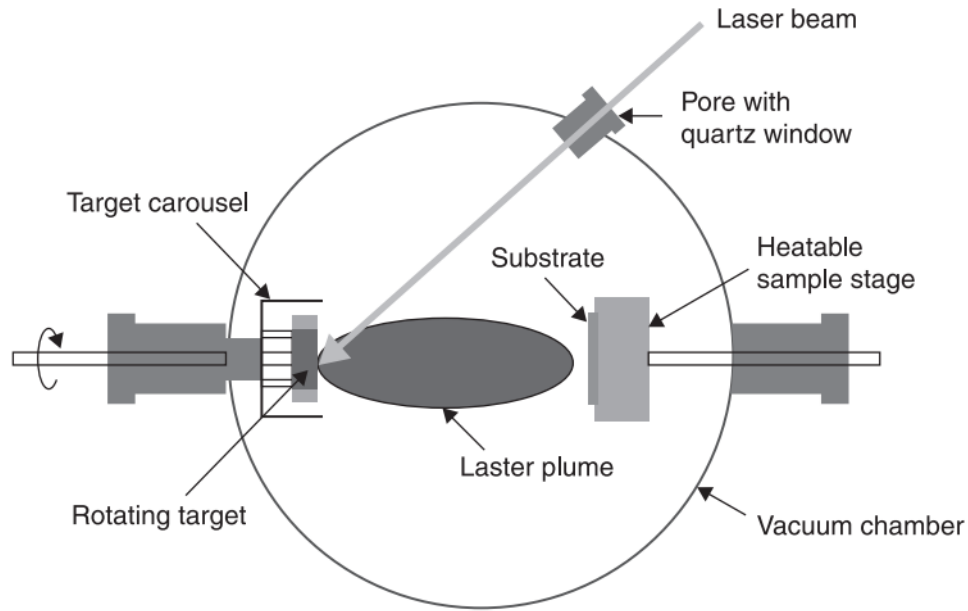
While two-phased growth is being investigated and explained in past literature, a new twist to the growth has been introduced. By including another metallic phase, it is possible to grow a three phased system. The benefits of having a three phased system instead of a two phased system is that by adding an additional phase, especially one with strong physical properties, to an existing two-phased system, it will lead to additional physical properties. This was shown by Shikhar Misra et al. that demonstrated the growth of Au and ZnO nanostructures within a BaTiO_3 matrix[144]. Au-BaTiO_3 already has shown strong plasmonic responses, but by including the ZnO with the Au it increases the hyperbolic response in the visible wavelengths. Interestingly though, the Au caps

¹¹ Image reproduced with permission of the rights holder, John Wiley and Sons.

the ZnO regions, showing a preferential nucleation of the metal phases together, showing potential other materials that will be able to grow a three-phased VAN system.

2. EXPERIMENTAL METHODOLOGY

2.1 Pulsed Laser Deposition



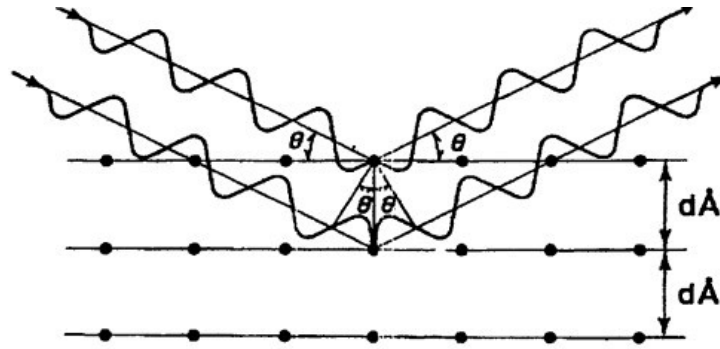
¹²Figure 2.1 Schematic set-up for a pulsed laser deposition[145].

Pulsed laser deposition (PLD) is a physical vapor technique that allows for a high level of deposition control. PLD works by ablating a target with a powerful laser (KrF excimer laser, $\lambda = 248$ nm) that ejects the target particles as plasma consisting of energetic ions deriving from the target composition. These ions travel through the chamber to land on the substrate. Once the ions land on the substrate, they are referred to as adatoms and undergo kinematic reactions to create the film. In pulsed laser deposition, there exists many parameters that are able to be tuned that will affect the kinematics from temperature to deposition frequency. In the case for the multiple phase VAN films, the growth conditions will play essential roles in tuning the strain and structures of the different phases, and by extension, the physical properties. For example, it has been extensively reported that deposition frequency plays a critical role in the diffusion and creation of the phases. Higher frequency will lead to a lower diffusion time, resulting in a lower diffusion length leading to lower diameters, and vice versa for lower frequencies. This elongation and narrowing of the

¹² Image reproduced with permission of the rights holder, Elsevier.

diameter of the different pillars allowing for the tuning of physical properties, especially in the case of the metallic VAN. Another key parameter that will play a factor in the growth kinematics is the laser energy. The laser energy will affect the plasma dynamics with the higher energies allowing for a higher degree of diffusion and will alter the nanostructure of the different phases.

2.2 X-ray Diffraction



¹³Figure 2.2 Schematic demonstrating the electron diffraction caused by atoms[146].

X-ray diffraction (XRD) is a powerful tool that allows for non-destructive composition analysis for a material. XRD utilizes a non-ionizing electron source to fire electrons at a certain angle at a material and counts the number of electrons that arrive at a detector after being reflected off the material. One of the most widely used scans to determine crystal orientation and composition is the theta-2theta scan. In this scan the detector moves at double the angular speed of the emitter. From Bragg's law, it is possible to calculate the vertical d spacing of the lattice allowing for the calculation for out-of-plane strain, and by extension, in-plane strain.

Not only can XRD be used to calculate the strain and find the orientation, it can be used to determine the crystallinity of the film. Amorphous films will not have a distinct diffraction peak, because there is no lattice for the electron to deflect off of. Polycrystalline film will have multiple peaks with irregular spacing. Lastly, crystalline films will have peaks with regular spacing. Additionally, more crystalline films will have a smaller full width half maximum (FWHM) than films with lower degree of crystallinity. From PDF cards, it is also possible to determine the correct orientations of the different peaks and to determine peak shifts to calculate strain.

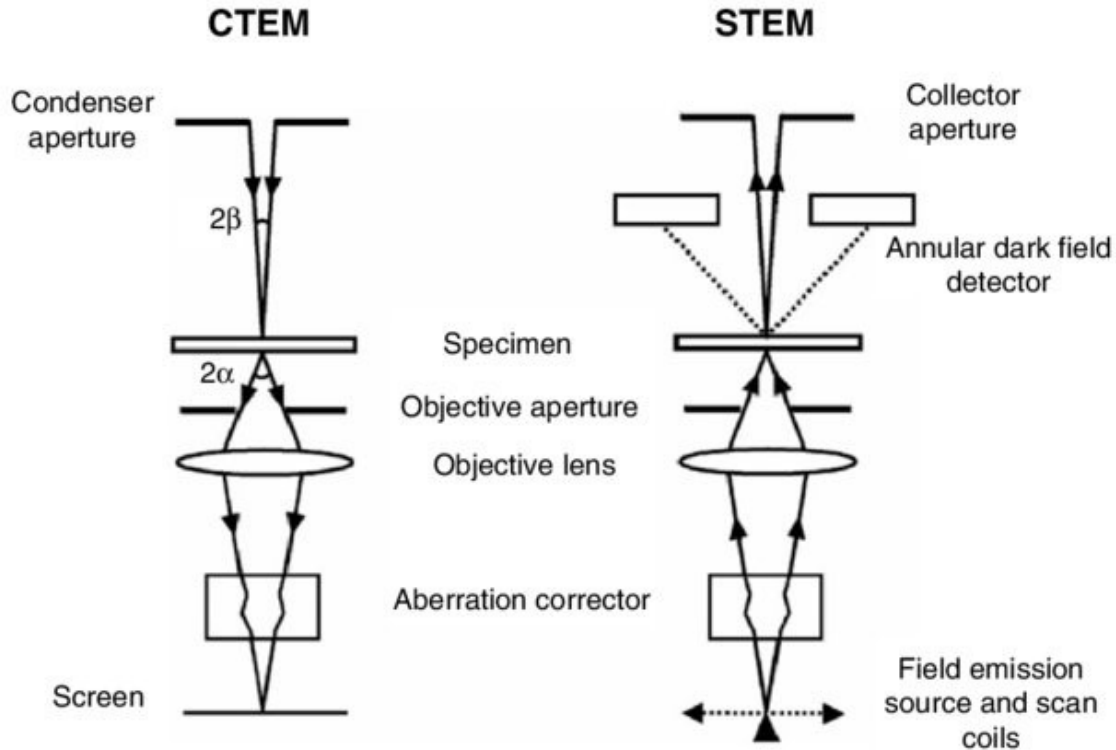
¹³ Image reproduced with permission of the rights holder, Elsevier.

2.3 Physical Property Measuring System and Magnetic Property measuring System

Physical Property Measuring System (PPMS) (Quantum Design) and Magnetic Property Measuring System (MPMS) (Quantum Design) are essential tools that allow for a wide range of electrical and magnetic measuring system. It allows for temperature control from 1.9 K to 400 K and allows for a wide array of magnetoelectrical and electrical testing in the case of the PPMS, and magnetic testing for the MPMS. The vibrating sample module (VSM) for the PPMS is similar to the MPMS system in which it uses a pair of electromagnets that can generate a DC magnetic field of up to 9 T. As the sample vibrates through a coil, it produces a magnetic flux change which induces an AC voltage that can be used to pick up the signal.

For the electron transfer option in the PPMS, it allows for both two and four wire measurements. The four-wire measurement system is reliable up to 1 MOhm, while the two-wire measurement system is reliable above that threshold. In the option, it allows to see the phase of the measurement and if it is above a few degrees, then a bad contact or the measurement settings is off. The four-wire measurement supports four connections and biases via current, and the two-wire measurement supports two connections and biases via a voltage. For the out-of-plane magneto transport measurements, the measurements were measured using the four-wire method with the two wires of V+ and I+ connected to the same contact on the surface and V- and I- connected to the same contact on the bottom conductive layer.

2.4 Transmission Electron Microscopy



¹⁴Figure 2.3 Schematic demonstrating the difference between how the electron beam arrives at the sample for TEM and STEM[147].

Transmission electron microscopy is used to image the nanostructure and study the overall crystal structure of the different films. TEM works by passing a powerful, electron beam through an electron transparent sample allowing for the imaging of the films. TEM was developed to replace the visible light used to magnify the sample with an electron beam allowing for much higher magnification. The TEM allows for atomic level magnification allowing for a detailed study on the nanostructure of the film and the crystal arrangement.

Presently, many TEMs have incorporated many other techniques in a single instrument besides the conventional imaging technique, such as high-angle annular dark field (HAADF), scanning transmission microscope (STEM), and energy-dispersive X-ray spectroscopy (EDX). The STEM mode focuses the beam as it hits the sample, allowing for a high contrast image, where the contrast is correlated to the atomic number. EDX mode allows for a detailed chemical

¹⁴ Image reproduced with permission of the rights holder, Springer Nature.

composition study of the film by analyzing the X-rays emitted by the atoms as the electron beam ionizes them.

2.5 Absorption Spectrophotometer

Absorption spectroscopy measures the percentage a material absorbs as light with varying wavelengths are shown through the sample. In this test, a focusing lens will focus a beam of light into a sample covering a pinhole. The amount of light that goes through the sample relative to the light being focused will be recorded and plotted. In the system that was used, the light wavelength ranged from the near infrared to the ultraviolet spectrum with the transmission percentages at different wavelengths being catalogued and plotted. This is especially important for plasmonic materials. At certain wavelengths in plasmonic materials, plasmonic resonance will occur at specific wavelengths of light, resulting in a dip in the transmission at these wavelengths due to the light being absorbed into the sample to produce the resonant oscillations. By quantifying the local minima along these dips, the plasmonic resonance point can be measured and detected.

In order to achieve accurate measurements utilizing this instrument though, sample preparation is a must. In thin film samples, the measured material is typically grown on a substrate that is typically single side polished. This will lead to the substrate blocking most of the incoming light. To only measure the film, it is necessary to polish the other side using diamond lapping paper until the substrate is optically transparent.

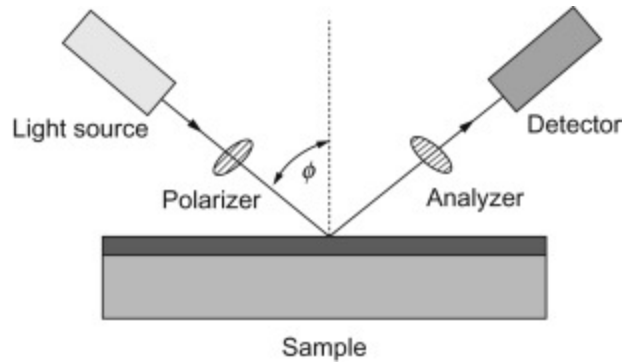
2.6 Magnetoelectro Coupling

In magneto-electric testing, the setup that was used was putting a sample in-between Helmholtz coils and wired in such a way to be able to measure the charge the sample generates within the coils. In this case, the samples had a contact on a conductive layer below the film to be measured and on the surface of the film. By utilizing the coils to produce a varying magnetic field, the instrumental setup will measure the charge generated by the film in response to the magnetic field. Based on the data from the varying magnetic field, it becomes possible to determine the magneto-electric coupling coefficient to quantify the coupling between the ferromagnetic and ferroelectric portions of the film. The magneto-electric coupling coefficient is calculated by using the equation below.

$$\alpha_{ME} = \partial E / \partial H \quad \text{Equation (10)}$$

Where α is the magnetoelectric coupling coefficient, E is the measured electric field across the sample, and H is the applied magnetic field.

2.7 Angular Dependence Ellipsometry



¹⁵Figure 2.4 Schematic of the typical setup of an ellipsometer[148].

Ellipsometry is a non-destructive instrument that measures the optical reflectance of a material to determine its optical properties. In ellipsometry, a polarized light is shone onto a sample and is refracted into a detector. As the polarized light is refracted, the sample will change the polarization of the light, and with the ellipsometer measuring the amplitude ratio of the different polarized light before and after being refracted the sample. For many different setups though, the angle of the incidence and the wavelengths of light can be varied. By varying these different parameters, it becomes possible to measure more data points from a single sample, allowing for more detailed characterization of a specific sample.

2.8 Atomic Force Microscopy

Atomic Force Microscopy (AFM) is a high-resolution type of scanning probe microscopy with resolutions in nanometers. The configuration of the AFM is that it consists of a cantilever that has a sharp tip that is utilized to scan the surface of the sample. When the cantilever reaches

¹⁵ Image reproduced with permission of the rights holder, Elsevier.

near the surface of the sample, a force is exerted between the tip and the sample which is characterized by Hooke's law.

There are a couple of different contact modes which are used to characterize the surface of the sample, with them being contact mode, tapping mode, and non-contact mode. In contact mode, the tip is moves at a constant height at the surface of the sample and the morphologies of the surface is mapped by indexing the force required to keep the cantilever at a constant height. In tapping mode, the cantilever is made to oscillate up and down near a resonant frequency. This mode is mainly utilized for films that develop a liquid meniscus layer. By oscillating up and down near the resonant frequency, the tip is able avoid being stuck to the surface of the sample, and it also reduces the amount of impact the tip will have when compared to the contact mode. The topology of the sample is measured by seeing the magnitude difference in the oscillations that are caused by the interactions between the surface and the tip. The last mode is non-contact mode. In this mode, the tip does not actually encounter the surface of the sample. This mode is mainly used for either soft or biological samples. In this mode, the cantilever is oscillated at a certain frequency at a set height above the sample. As the cantilever moves along the surface, forces between the surface and the sample interact changing the oscillating frequency. This change is compensated by the AFM and mapped to produce a topology map.

Of importance to measuring ferroelectric materials is piezoresponse force microscopy (PFM). This is a type of AFM that enables the imaging and the measuring of piezoelectric, and by extension, ferroelectric domains. This measurement is performed by putting a sharp tip in contact with the surface of a sample and applying an AC signal. This will induce a deformation in the sample surface due to the converse piezoelectric effect. This deformation will then cause a deflection in the cantilever which is measured using a laser diode in conjunction with a lock in amplifier. Generally, the piezoelectric properties are characterized by the phase and the magnitude of the piezoresponse of the sample to an AC signal. As the AC signal is applied with a sweeping DC bias, as the DC bias switches the polarization direction of the sample, the piezoresponse will have a phase difference from the AC signal with the phase change being 180° as the polarization changes from one direction to another. Additionally, the magnitude of the piezoresponse indicates the strength of the ferroelectric response which will lead to the calculation of the d_{33} .

3. RESEARCH CHALLENGES AND FUTURE DIRECTIONS

Metallic VAN has been shown to have extremely promising physical properties, from optical to ferromagnetic. Additionally, it has been shown that a single metal with highly desired room-temperature properties can be included into different oxides. There are still needs to be an understanding of the growth mechanics of the metallic VAN is needed to better tune their physical properties by changing the metallic nanostructure and to better select the two phases that leads to better crystallinity and by extension, better properties.

As more and more metallic VAN are discovered and fabricated, there comes an interesting possibility of introducing another physical property into the system. There are two different methods to add more properties into the metallic VAN system. One method is by changing the oxide into a material that has highly desired properties, such as BTO with its strong ferroelectric properties. There needs to be careful consideration into which oxide to integrate into the metallic VAN, because if the lattice parameter of the oxide leads to a highly strained state, the VAN might not successfully grow. The second option is to integrate another material phase into the metallic VAN phase. If one was to introduce another material with highly desired physical properties into a metallic VAN to form a third phase that will lead to improve functionality. For example, adding Au to the metallic VAN will allow for the introduction of a highly coveted plasmonic, leading to interesting optical properties into the original two-phase metallic VAN.

In order to utilize the metallic VAN growth for devices, more work needs to be done on patterning and long-range ordering. Array of devices and circuits require precise control of the spacing. To integrate these metallic VAN where each metallic VAN can be a location of a device, there needs to be a more detailed study on a method. It has been showing that by templating the substrate, the pillars are able to be concentrated along lines across the substrate[149]. The main drawback it suffers from is the limitation that it still not possible to accurately predict the location of each pillar. As more studies are done on etching and patterning on substrates, it may eventually be feasible to control individual growth locations of the metallic VAN.

Finally, despite the limitations, VAN remains a promising candidate for anisotropic applications. Its single step growth allows for a simplicity that does not exist in patterning and etching to achieve its unique column geometry. As work continues on VAN, it will be possible to

introduce even more tuning and properties into the VAN system and leading to promising VAN films for spintronic integrations.

4. TUNABLE MAGNETIC ANISOTROPY OF SELF-ASSEMBLED FE NANOSTRUCTURES WITHIN A LSFO MATRIX¹⁶

4.1. Summary

Metallic nanostructures within ceramic matrices provide a unique platform for integrating magnetic, optical, and electrical properties for device applications. Currently, hurdles still exist for the integration of metallic nanostructures within conventional devices, including the incompatible growth conditions between metals and ceramics and control of the overall physical properties. In this study, we demonstrate the tunability of a one-step growth method to fabricate magnetic and metallic nanostructures embedded within an oxide matrix, $\text{La}_{0.5}\text{Sr}_{0.5}\text{FeO}_3\text{:Fe}$, from a composite target using pulsed laser deposition. The metal-ceramic nanocomposite films demonstrate tunable nanostructures and anisotropic magnetic response by varying deposition energy, presenting a mechanism for tuning the physical properties of vertically aligned ferromagnetic metallic nanopillars in an oxide matrix. This study also opens avenues towards the integration of nanoscale, vertical, metallic ferromagnetic contacts for anisotropic magnetic tunneling junctions which may not be easily realized by single-phase thin films.

4.2. Introduction

Spintronics is based on the interaction between the spin of electrons and the magnetic properties of materials[150,151]. This interaction is used for spin-dependent applications in semiconductor devices such as memory devices[5,152–154] and sensors[5,155]. Among these devices, tunnel junctions are especially prominent because of their potential applications as low-current, high density, and non-volatile memory devices[1,156]. Tunnel junctions can be classified into three different types based on the mechanism for resistive switching: ferroelectric-[61], ferromagnetic-[157], and multiferroic-tunnel junctions[71,158], which use a ferroelectric barrier[159], a ferromagnetic contact surrounded by a non-ferromagnetic barrier, and a ferroelectric-ferromagnetic barrier, respectively[71]. There has been recent interest in anisotropic

¹⁶ This chapter is reprinted with permission from “Tunable magnetic anisotropy of self-assembled Fe nanostructures within a $\text{La}_{0.5}\text{Sr}_{0.5}\text{FeO}_3$ matrix” by B. Zhang, et al., Appl. Phys. Lett., **2018**, 112, 013104. © 2018, American Chemical Society.

ferromagnetic materials with an out-of-plane easy axis for room-temperature ferromagnetic tunneling junctions. These materials have the potential to reduce both the size and the current of devices while maintaining large tunnel magnetoresistance switching[66,160,161]. Metals with ferromagnetic response (e.g., Fe, Co, and Ni) are the preferred anisotropic ferromagnetic materials owing to their strong magnetic responses and high Curie temperature (e.g., $T_C = 1043$ K and saturation magnetization ~ 1700 emu/cc for Fe).

Oxide-oxide vertically aligned nanocomposites (VANs) represent a unique platform to tune and enhance physical properties such as low-field magnetoresistance and ionic conductivity[130,162–165]. For example, Chen et al. reported a peak magnetoresistance of 30% in $\text{La}_{0.7}\text{Sr}_{0.3}\text{MnO}_3:\text{ZnO}$ via controlling the nanostructures[130]. Recently, advancements in VANs allowed for the growth of highly uniformed, epitaxial metallic pillars (e.g., Au and Ni) embedded within a ceramic matrix[138,139] by pulsed laser deposition (PLD) using a composite metal-ceramic target. However, the deposition of composite metal-ceramic materials faces difficulties due to the oxidation nature of metals especially for Fe, which is easy to be oxidized during the high temperature growth[166]. One promising solution is the formation of Fe pillars embedded in the $\text{La}_{0.5}\text{Sr}_{0.5}\text{FeO}_3$ (LSFO) matrix through self-decomposition of LSFO. LSFO is a well-studied material system with an epitaxial LSFO film grown on single-crystalline (STO) SrTiO_3 (001) by pulsed laser deposition (PLD) under certain oxygen pressure. Instead, under vacuum, Fe pillars can be formed within the LSFO matrix on STO (001). The composite LSFO with epitaxial Fe pillars embedded exhibits a high magnetization of 1600 emu/cc at room temperature. This composite film is a promising candidate due to its high anisotropic magnetic response at room temperature.[167]

In this study, we utilized a $\text{LSFO}:\text{Fe}_2\text{O}_3$ composite target to fabricate high density Fe nanoinclusions in the LSFO matrix. Laser energy is tuned to vary the Fe inclusion morphologies from nanopillars to nanodots, and thus, tunable anisotropic magnetic properties can be achieved in these nanocomposite systems. Detailed microstructural characterization studies including TEM/STEM (transmission electron microscopy/scanning transmission electron microscopy) are coupled with magnetic property measurements to explore the impacts of the overall kinetic energy on the growth morphologies and physical properties of $\text{LSFO}:\text{Fe}$ nanocomposites.

4.3. Experimental

A composite target $\text{La}_{0.5}\text{Sr}_{0.5}\text{FeO}_3\text{:Fe}_2\text{O}_3$ (molar ratio 94:6) was prepared using a conventional ceramic sintering method. Two sets of epitaxial films were grown on single-crystal SrTiO_3 (STO) (001) substrates by PLD (KrF excimer laser, $\lambda = 248$ nm) with a laser fluence of 1.9 J/cm^2 at 750°C under high vacuum and laser frequencies of 2 and 5 Hz, respectively. The 2 Hz sample has a thickness of 25 nm, and the subsequent set of films' thicknesses is between 80 and 100 nm. After deposition, the films were cooled to room temperature under high vacuum.

The epitaxial quality of the films was characterized using X-ray diffraction (XRD, PANalytical Empyrean). The nanostructure and its phase separation were further investigated via transmission electron microscopy (TEM, FEI TECNAI G2 F20), electron-dispersive X-ray spectroscopy (EDS), and scanning transmission electron microscopy (STEM, FEI TALOS T200X). The magnetic measurements were performed at 300 K using a commercial physical property measurement system (PPMS 6000, Quantum Design) coupled with the vibrating sample magnetometer (VSM) option. A magnetic field of 5000 Oe was applied perpendicular and parallel to the film plane for out-of-plane and in-plane measurements, respectively.

4.4. Fe:LSFO Growth and Characterization

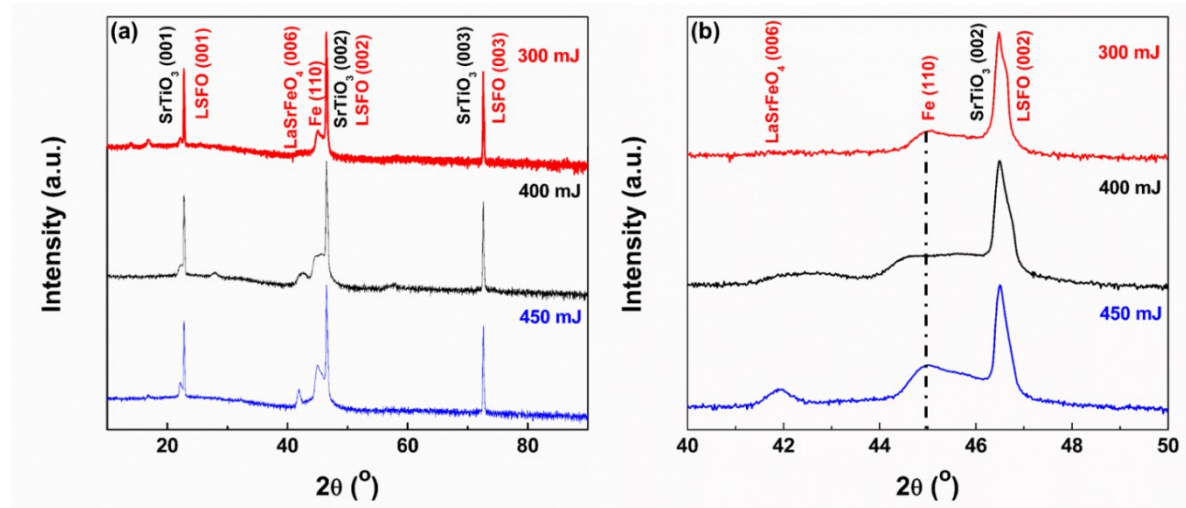


Figure 4.1 Phase identification of metal-ceramic LSFO:Fe films grown at 5 Hz. (a) X-ray diffraction (XRD) h-2h patterns of the LSFO:Fe film grown at different deposition energies showing the presence of Fe (110) peaks. (b) Magnified XRD h-2h patterns centered around the Fe (110) peak displaying the peak shift.

To characterize the phase and investigate the composition of the LSFO-Fe films deposited at different laser energies, XRD θ - 2θ patterns were collected for the samples. Figure 1 shows the XRD θ - 2θ patterns of the thin films deposited on STO (001) substrates at 300, 400, and 450 mJ with a laser frequency of 5 Hz, respectively. From Fig. 1(a), the diffraction peaks located at $2\theta = 45.035^\circ$ or 44.600° and $2\theta = 41.7^\circ$ for the films deposited at different laser energies are attributed to Fe (011) and LaSrFeO₄ (006). The position of the Fe (011) peak shifts with various deposition energies as shown in Fig. 1(b), indicating a structural difference between the films deposited at different energies. For the samples deposited at 300 and 450 mJ, the Fe (011) peak is located at 45° with a corresponding d spacing value of 2.103 nm. For the sample deposited at 400 mJ, however, the Fe (011) peak shifts left to 44.600° with a corresponding d spacing value of 2.030 nm. This peak shift indicates a -0.163% strain compared to the bulk value of Fe (110) d-spacing of 44.673° (pdf card: 06-0696). For the sample deposited at 400 mJ, additional peaks of LaSrFeO₄ (004) and LaSrFeO₄ (008) located at $2\theta = 27.92^\circ$ and 57.74° have been observed, respectively. The film deposited at 400 mJ displays distinct peaks of Fe (011), LaSrFeO₄ (004), and La_{0.5}Sr_{0.5}FeO₃ (002), which may indicate that a reaction $2\text{La}_{0.5}\text{Sr}_{0.5}\text{FeO}_3 \rightarrow \text{LaSrFeO}_4 + \text{Fe} + \text{O}_2$ occurs as previously reported[136].

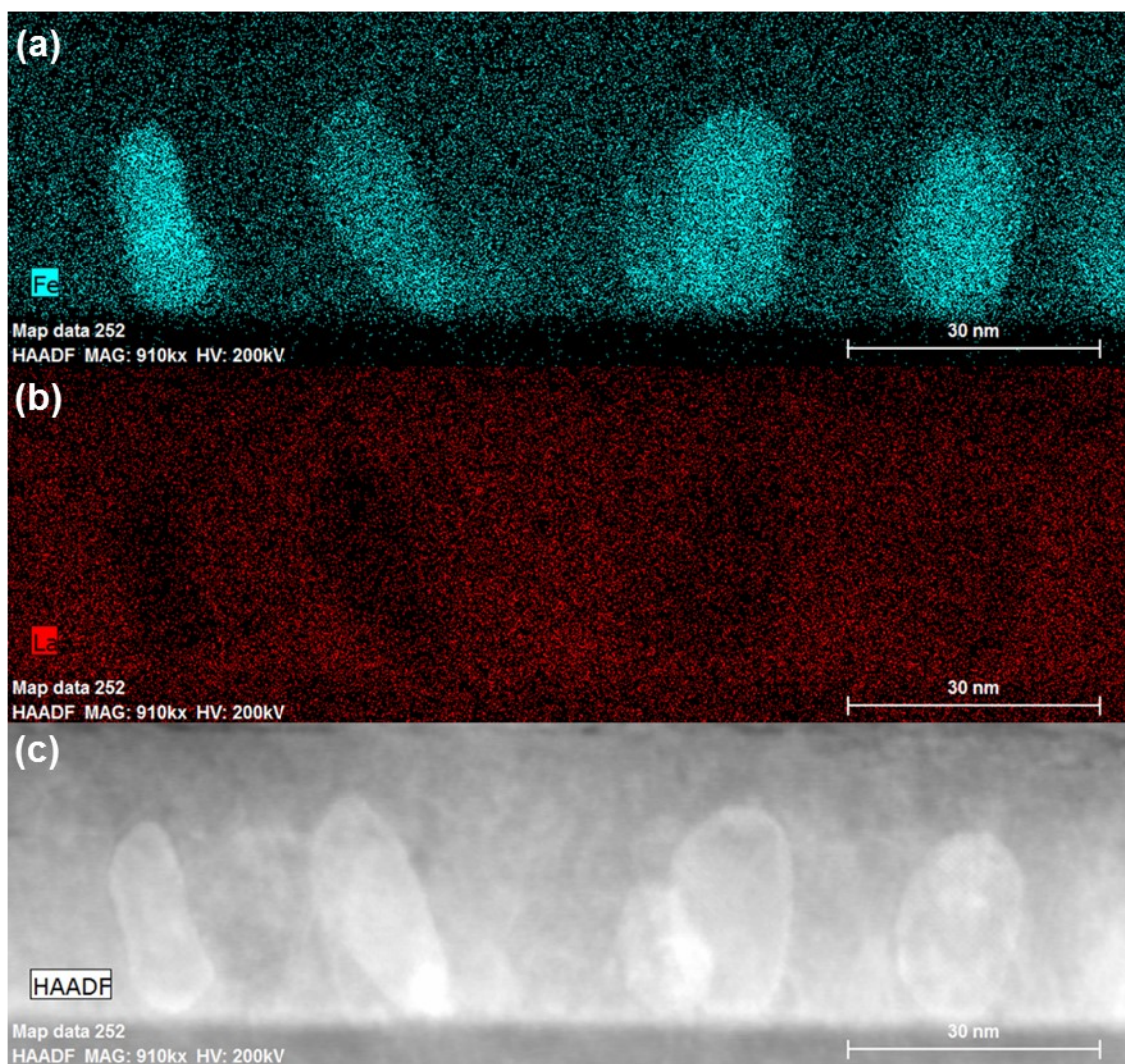


Figure 4.2 Phase and composition demonstration of the LSFO:Fe film grown at 2 Hz. (a) Typical cross-sectional STEM HAADF image of the LSFO:Fe exhibiting Fe nanostructures within the oxide matrix. (b) Fe and (c) La atomic scale EDS elemental maps confirming metal within the oxide matrix.

STEM coupled with EDS mapping was applied to further verify the phase separation and composition of the LSFO:Fe thin film. The STEM image of the film deposited at 2 Hz in the high angle annular dark-field (HAADF) mode (Fig. 2) displays uniformly distribution of Fe pillars with clear phase separation from the surrounding matrix. The average pillar diameter is 15 nm. The EDS mapping of La and Fe confirms a clear separation and the presence of Fe nanostructures within the matrix. Cross-sectional and plan-view TEM images of the 2 Hz sample were taken to further characterize the nanostructure as shown in Fig. 3. The plan-view image in Fig. 3(a) shows

the uniform distribution of the Fe nanostructure in the matrix with a diameter of ~ 15 nm. The cross-sectional image in Fig. 3(b) shows that Fe nanostructures grow in a pillar fashion throughout the film thickness.

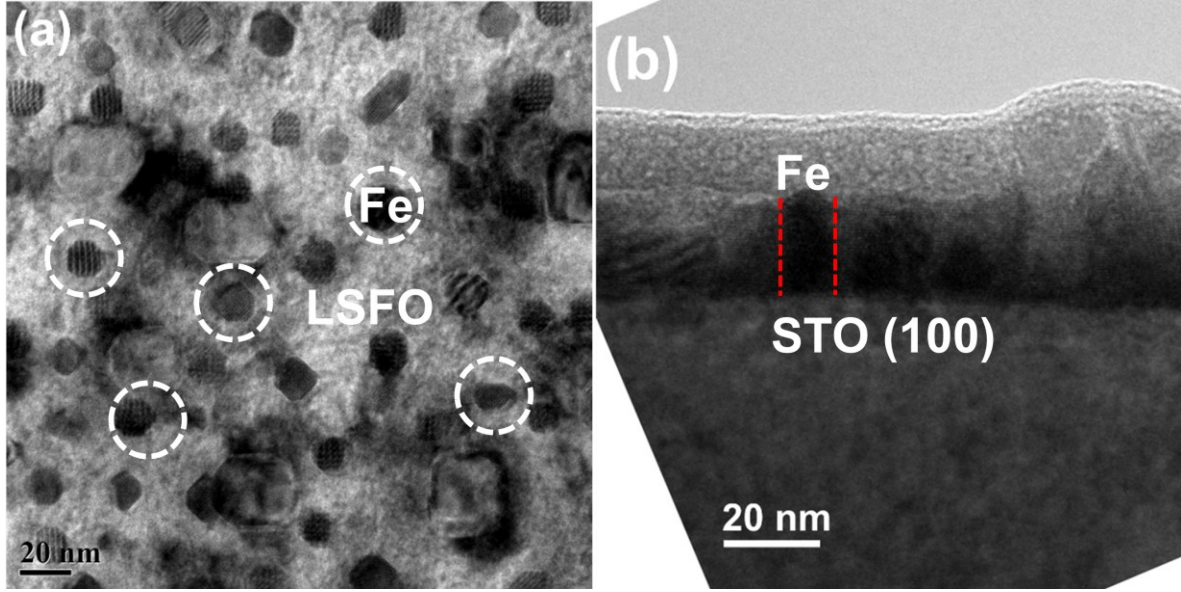


Figure 4.3 Typical (a) plan-view and (b) cross-sectional TEM image of the metal-ceramic thin film grown at 2 Hz. These images clearly show the uniform distribution of the Fe nanostructures within the oxide matrix.

To further investigate the relationship between the nanostructure of the metal-oxide thin films and the deposition energy, both cross-sectional and plan-view TEM images were obtained for samples deposited under different deposition energies, as shown in Fig. 4. Figures 4(a)–4(c) show the cross-sectional TEM images of the composite thin films deposited under 300 mJ, 400 mJ, and 450 mJ, respectively. The LSFO matrix displays brighter contrast, while Fe shows darker contrast. For the 300 mJ sample, the film exhibits multiphase growth consisting of polycrystalline, column structures with a diameter of ~ 80 nm and smaller Fe nanoparticles with a diameter of around 25 nm. Within the 400 mJ sample, Fe predominantly grows in two modes: the ordered epitaxial column growth and the less-ordered particle growth. The diameter of the columns is ~ 15 nm, and the diameter of the particles is ~ 80 nm. The 450 mJ sample shows substantial Fe growth with the diameter in the order of 100 nm. Additionally, these particles do not go through the film thickness.

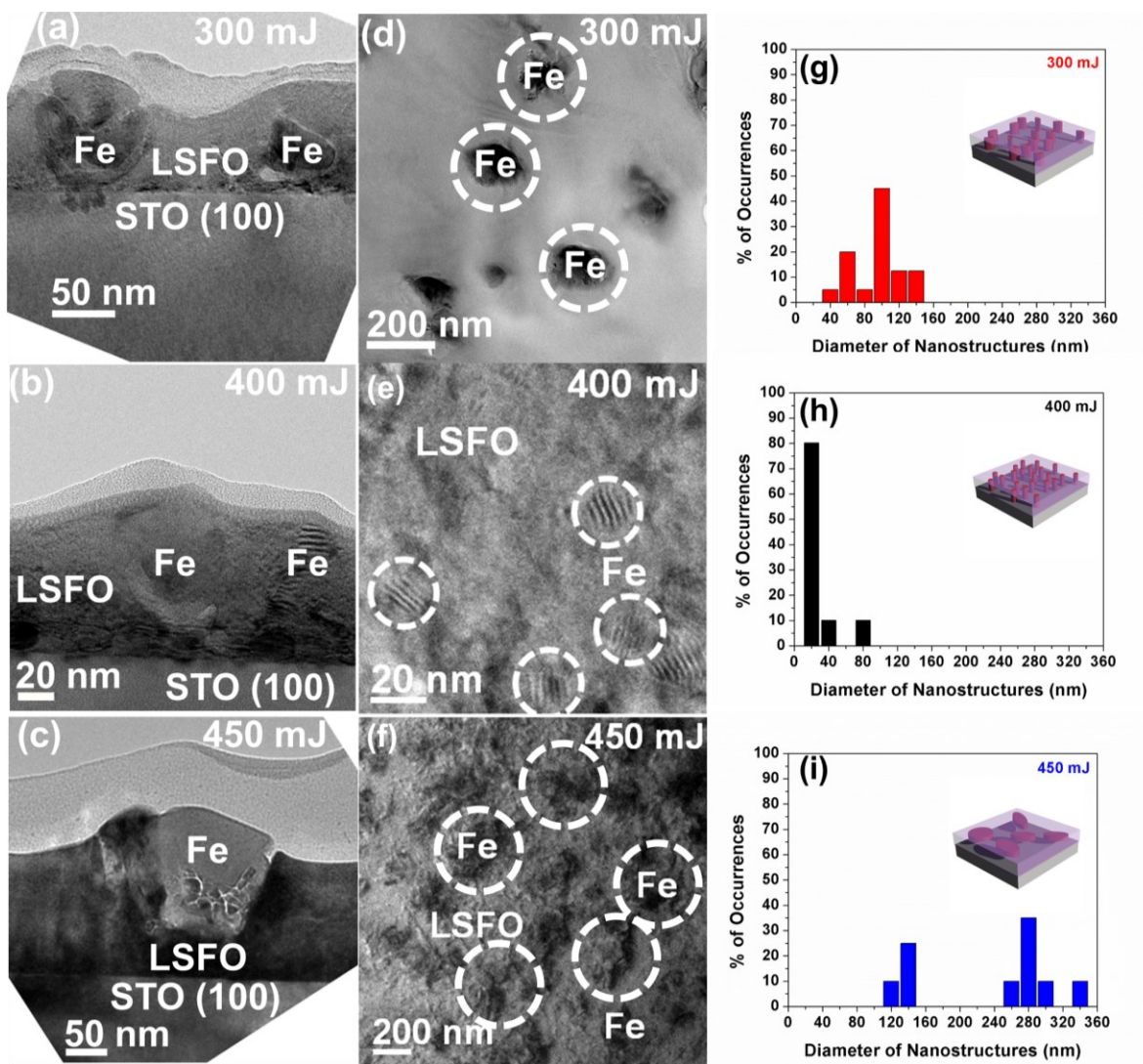


Figure 4.4 (a-c) Cross-sectional and (d-f) plan-view TEM images of Fe nanostructures within ceramic matrix grown at 5 Hz and different energies of 300 mJ, 400 mJ, and 450 mJ, respectively. (g-i) Diameter distribution of the Fe nanostructures within the oxide matrix.

Figures 4(d)–4(i) show the plan-view TEM images of the films and the corresponding histogram plot of the Fe nanoparticle diameter distribution. It is obvious that the lateral diameter and morphology of the Fe nanoparticles vary with laser energy. In the case of the 300 mJ sample, the Fe particles have an ellipsoid shape with the lateral dimension of around 100 nm. For the 400 mJ sample, the Fe phase shows two distinct growth morphologies. A majority of Fe particles have the hexagonal, more ordered Fe (110) growth with a diameter of around 15 nm as shown in the 2 Hz run, and the others are the less ordered agglomerations with over 100 nm in diameter. For the 450 mJ sample, most of the Fe particles grow as large agglomerations with random orientation.

Such a difference in the nanostructure can be correlated with the laser energy variation and the resultant different growth kinetics. For the samples deposited under lower laser energy, the adatoms have less kinetic energy to grow in an epitaxial manner and thus result in large, polycrystalline Fe particles. For the 400 mJ sample, the higher kinetic energy allows high diffusivity of adatoms and thus results in the ordered epitaxial growth of the Fe nanoparticles. With the highest laser deposition energy, the adatoms have much excess kinetic energy, which promotes diffusion and results in large Fe particles.

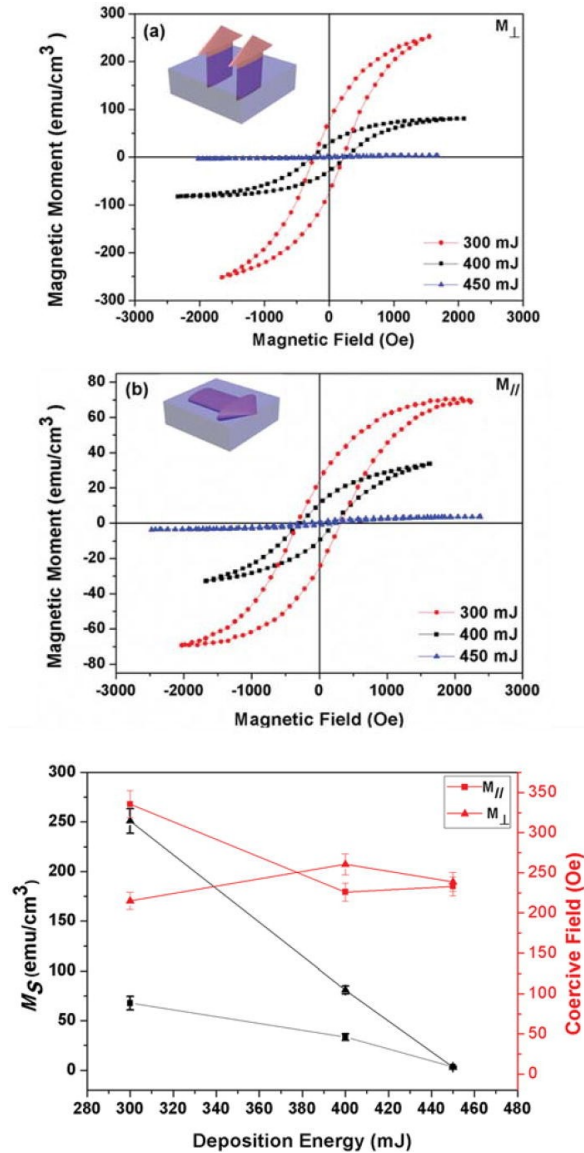


Figure 4.5 Room-temperature (a) In-plane and (b) out-of-plane magnetic hysteresis loops of the metal-ceramic thin films deposited at different energies. (c) Plot of magnetizations along both in-plane and out-of-plane and deposition energies showing the relationship between the magnetic anisotropy and deposition energy.

4.5. Fe:LSFO Ferromagnetic Characterization

To explore the structure and property correlation, the magnetizations of the films were measured along both the in-plane ($M_{//}$) and out-of-plane (M_{\perp}) directions with the magnetic field parallel and perpendicular to the film, respectively. The room-temperature out-of-plane and in-plane magnetic hysteresis loops are shown in Figs. 5(a) and 5(b), respectively. The saturation magnetic moment (MS) along both the in-plane and out-of-plane directions decreases with increasing deposition energy, i.e., the highest out-of-plane magnetic response (251 emu/cm^3) for the 300 mJ sample and the lowest value (3 emu/cm^3) for the 450 mJ sample. This trend may be attributed to the difference in both the nanostructure and growth crystallinity of the Fe nanostructures embedded within the ceramic matrix. The LSFO:Fe film in this study has highly anisotropic magnetic properties due to the vertical Fe nanostructures that vary with the deposition energy. The magnetic anisotropy follows the trend as the MS values with the highest energy (450 mJ) having the lowest ratio of 1.0 and the lowest energy (300 mJ) having the largest ratio of around 3.8. For the 300 mJ sample, the average diameter of the Fe nanostructures ($\sim 80 \text{ nm}$) is significantly larger than the 400 mJ sample ($\sim 15 \text{ nm}$). The larger Fe nanoparticles result in a higher density of Fe within the film, explaining the difference in magnetic properties. For the 450 mJ sample, the diameter of the Fe nanoparticles is slightly larger than the 300 mJ sample, but the magnetization of the sample is significantly lower. The adatoms of the 450 mJ sample have sufficient kinetic energy for diffusion, thus resulting in the larger diameters of the Fe nanoparticles with more isotropic shape and similar magnetization values for both in-plane and out-of-plane directions. However, the excess kinetic energy results in epitaxial quality reduction, which also accounts for the dramatic decrease in magnetic properties. In the case of the 450 mJ, multiple grains have been observed within the Fe nanostructures. Granular structures have been previously shown to influence magnetic properties[167,168] compared to single crystalline samples.

By adjusting the laser energy, one can adjust the morphology of the nanostructure, the nanoinclusion density, and thus, the magnetic properties. The 400 mJ sample shows semi-regular distribution of uniform, ordered pillars with anisotropic magnetic properties. The 300 mJ sample shows less ordered nanostructures but higher MS. This self-assembled metal-oxide nanocomposite has potential applications in spintronic devices, especially within tunnel junctions as a ferromagnetic contact. Future work is needed to better tune the nanocomposite morphology to

combine the superior magnetic properties of the 300 mJ samples and the ordered nanostructure growth of the 400 mJ sample.

4.6. Conclusion

In summary, we have investigated the effects of laser deposition energy on the nanostructure and magnetic properties of the LSFO:Fe (oxide: metal) nanocomposite films using the target composition of $(\text{LSFO})_{0.94}:(\text{Fe}_2\text{O}_3)_{0.06}$. The laser energy significantly influences both the dopant morphology and the magnetic properties of the metal-oxide nanocomposite thin films. Lower laser energy leads to the samples with higher magnetic moments and vice versa. This confirms the tunability of the metallic nanostructure in the oxide matrix and the subsequent physical properties. This work demonstrates the feasibility of growing Fe nanoparticles in VAN form as anisotropic magnetic materials and the ability to tune the physical properties for future magnetic data storage devices and non-volatile memory devices.

5. TUNING MAGNETIC ANISOTROPY IN CO-BZO VERTICALLY ALIGNED NANOCOMPOSITES FOR MEMORY DEVICE INTEGRATION¹⁷

5.1 Summary

Ferromagnetic nanostructures with strong anisotropic properties are highly desired for their potential integration in spintronic devices. Several anisotropic candidates, such as CoFeB and FePt, have been previously proposed, but many of them have limitations such as patterning issues or thickness restrictions. In this work, Co-BaZrO₃ (Co-BZO) vertically aligned nanocomposite (VAN) films with tunable magnetic anisotropy and coercive field strength, have been demonstrated to address this need. Such tunable magnetic properties are achieved through tuning the thickness of the Co-BZO VAN structures and the aspect ratio of the Co nanostructures, which can be easily integrated into spintronic devices. As a demonstration, we have integrated the Co-BZO VAN nanostructure into tunnel junction devices and demonstrated resistive switching alluding to Co-BZO's immense potential for future spintronic devices.

5.2 Introduction

Spintronics[151] cover a wide range of devices that operate via electron spins, such as neuromorphic memory[169], MRAMs[69,156,170], Spin Torque Transfer (STT) devices[69,160], etc. In spintronics, ferromagnetic materials are of great interest due to them being a primary in spintronic devices. Taking a typical group of spintronic devices as an example, magnetic tunnel junctions have received great interest due to their potentials for high performance memories and various other applications[6,171–173]. Magnetic tunnel junctions typically consist of ferromagnetic films that play pivotal roles in the resistive switching[67]. To create higher resistive switching ratios and more responsive magnetic tunnel junctions, extensive work has been done on tuning and fabricating ferromagnetic material. To this end, two approaches to improve the tunnel junction performances for low energy and high frequency applications are by adjusting the coercive field of the ferromagnetic material[174–178] and to integrate anisotropic ferromagnetic

¹⁷ This chapter is reprinted with permission from B. Zhang, J. Huang, J. Jian, B. X. Rutherford, L. Li, S. Misra, X. Sun and H. Wang, *Nanoscale Adv.*, 2019, **1**, 4450–4458. - Published by The Royal Society of Chemistry.

films[179]. For the second approach, various ferromagnetic materials, such as SmCo₅[180], CoFeB[181–183], Fe-Pt[184], and Pd/Co layered structures[185] have been explored by using strain[186,187] and patterning[188] to achieve their anisotropic magnetic properties. For example, CoFeB and Fe-Pt[181–184] have shown anisotropic physical properties with certain thicknesses, while others[180,185] require numerous layers or patterning to achieve anisotropic magnetization. Overall the techniques and modifications to tune the perpendicular anisotropy materials have shown success, but they require either stringent deposition conditions or post-processing techniques.

Vertically aligned nanocomposites (VAN) are self-assembled nanocomposite thin films with nanopillars (phase 1) embedded in a matrix (phase 2) allowing for tunable anisotropic physical properties without extensive processing and patterning requirements and thickness constraints[135,189], which allows the single-step growth of a wide range of 2-phase materials. In addition, VAN are of particular interest due to their versatile material combinations toward enhanced or new physical properties. For example, oxide-oxide VAN systems are widely reported to achieve highly desirable physical properties such as low field magnetoresistance[129,130], exchange bias[127,164,190], and multiferroic properties[134]. Their unique physical properties of VAN, especially their tunable magnetic anisotropy, are of particular importance to magnetic tunnel junctions. Very recently, the development of metal-oxide based VAN systems[123,137,138,191] extend the ferromagnetic material candidates in the VAN designs from oxides to metals allowing for stronger ferromagnetic properties. Despite the challenges in the co-growth of metal-oxide due to the largely different growth conditions and possible oxidation of the metal, several metal-oxide VAN structures have been successfully achieved by pulsed laser deposition (PLD) with careful growth condition control. Such examples are Ni-CeO₂[137], Ni-Ba_{0.8}Zr_{0.2}Y₃[138], Co-BaZrO₃[123], Fe-La_{0.5}Sr_{0.5}FeO₃[191], Au-BaTiO₃[139], Au-TiO₂[140]. All of the films are metal nanopillars in oxide matrix and show very strong anisotropic physical properties with tunable coercive fields, ideal for integration into spintronic devices.

In this work, Co-BZO VAN thin films with well controlled nanopillar shape anisotropy (i.e., the aspect ratios of the Co nanopillars) has been demonstrated with the goal to achieve tunable magnetic anisotropy and tunable coercive field strength of the magnetic nanostructures. Previous work has shown tuning the physical properties via altering the deposition frequency[123], while this work demonstrates tunable physical properties, e.g., magnetic anisotropy, via tuning the

aspect-ratio of the Co nanopillars. This study also allows the investigation of the growth mechanism of metal-oxide VAN. Such tunability was achieved by controlling the film thickness from 4 nm to 35 nm, as shown in Figure 1, with the thinnest being smaller than the diameter of the Co nanopillars and the thickest being significantly larger than the pillar diameter. Ferromagnetic properties in both in-plane and out-of-plane were subsequently measured and compared with the shape anisotropy in the Co-nanopillars. Finally, different from previous work, the Co-BZO thin films in this work were grown significantly under 100 nm, for the purpose of Co-BZO VAN integration in a spintronic device. The device demonstrates resistive switching properties under applied magnetic field that highlights the potential of the Co-BZO VAN towards integrated tunnel junction devices.

5.3 Experimental

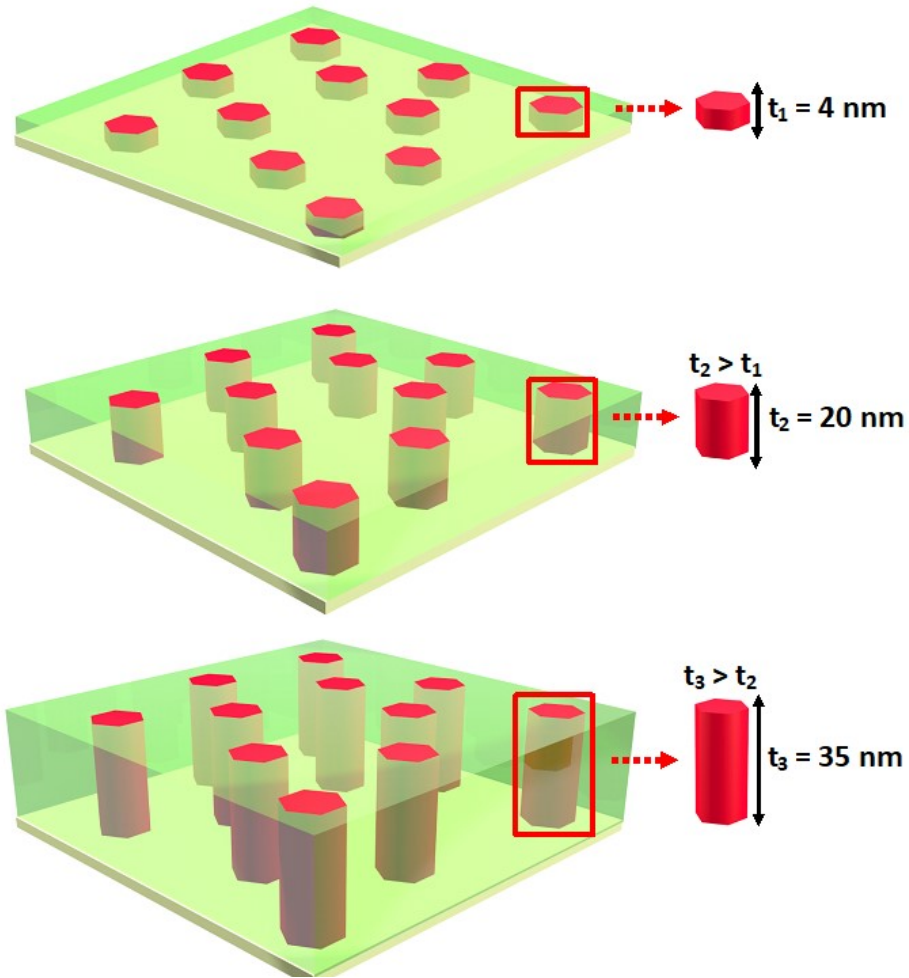


Figure 5.1 Schematic showing the different thicknesses investigated to determine how thickness and, in extension, aspect ratio between the thickness of the film and diameter of the Co pillars affect the physical properties.

The Co-BZO (Co-BaZrO₃) target was prepared following the standard solid-state target processing steps. Initially, a BaZrO₃ target was prepared via conventional powder pressing and sintering methods using BaCO₃ and ZrO₂ powders. Next, the BaZrO₃ target was crushed and further grinded into powder, and then combined with Co powders following a molar ratio of BZO:Co 60:40 and sintered at 1100 °C, with inflowing Ar/H₂. The Co-BZO nanocomposite thin films were grown on SrTiO₃ (STO) (001) via a pulsed laser deposition (PLD) system (KrF laser, 248 nm) with varying thicknesses of 4 nm, 20 nm, and 35 nm. The depositions were performed at a frequency of 5 Hz

under high vacuum conditions ($<1 \times 10^{-6}$ Torr) at 750 °C with a target-to-substrate distance of 5 cm.

The crystal structure and nanostructure of the films were studied by X-ray diffraction (XRD) (Panalytical X'Pert X-ray diffractometer) and transmission electron microscopy (TEM), scanning transmission electron microscopy (STEM), and energy-dispersive X-ray spectroscopy (EDX) (FEI Talos-200X). The magnetization properties of all the samples were measured both in-plane and perpendicular to the thin film surface in a Magnetic Property Measuring System (MPMS, Quantum Design). The electrical properties of the multilayer structure were measured using Au contacts deposited via PLD on the film using a Physical Property Measuring System (PPMS, Quantum Design).

5.4 Co-BZO Nanostructure Characterization

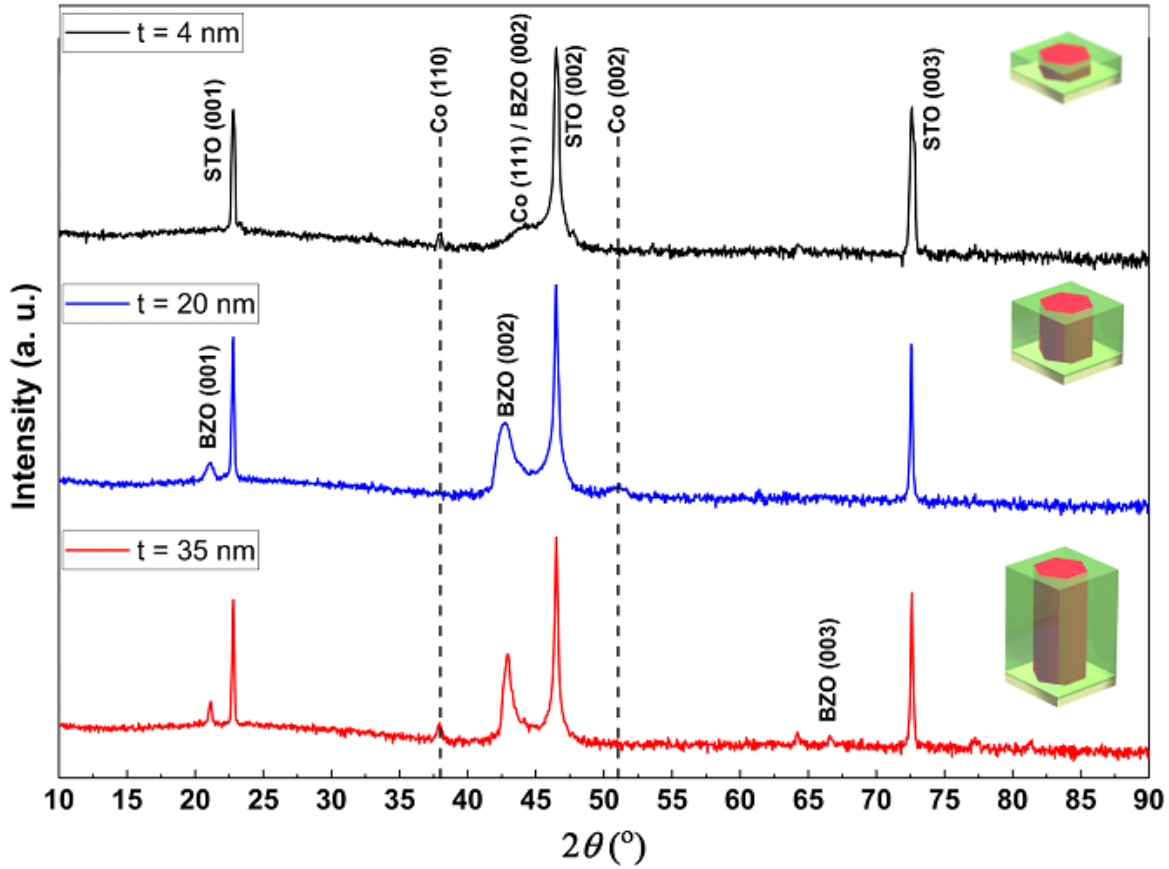


Figure 5.2 Typical θ - 2θ XRD scan of the different films deposited at different thicknesses with corresponding schematic to illustrate the aspect ratio.

Microstructure characterization by XRD was first conducted to analyze the growth orientation and growth morphology of the Co-BZO nanocomposite thin films with different thicknesses (4 nm, 20 nm and 35 nm). θ - 2θ XRD scans are shown in Figure 2 for all Co-BZO films. BZO (001) peaks can be identified in the 20 nm and 35 nm films, but not in the 4 nm sample. The lack of BZO (001) peaks in the 4 nm sample is possibly due to the ultrathin film and small amount of BZO within in the film. The BZO (002) is located at around 42.81° with a corresponding d-spacing of 2.11 Å. All the Co peaks overlap well with the Face Centered Cubic Co PDF card (PDF #15-0806) with the Co (111) peak (reference $2\theta = 44.216$, $d = 2.0467$ Å) in all samples, Co (200) peak (reference $2\theta = 51.522$, $d = 1.7723$ Å) in the 20 nm sample, and a Co (110) peak (reference $2\theta = 37.927$, $d = 1.2532$ Å) in the 35 nm sample. The Co (111) peak is located at 43.96° with a corresponding d spacing of 2.06 Å for the 4 nm film only, indicating a tensile out-of-plane strain (0.68%) for Co

due to the larger d-spacing of BZO (2.11 Å). For the 35 nm sample, the BZO (002) peak intensity is the sharpest, indicating better crystallinity of the BZO within the 35 nm sample, and the Co (110) peak has the highest intensity indicating a preferred Co growth direction of Co (110) as the film thickness increases.

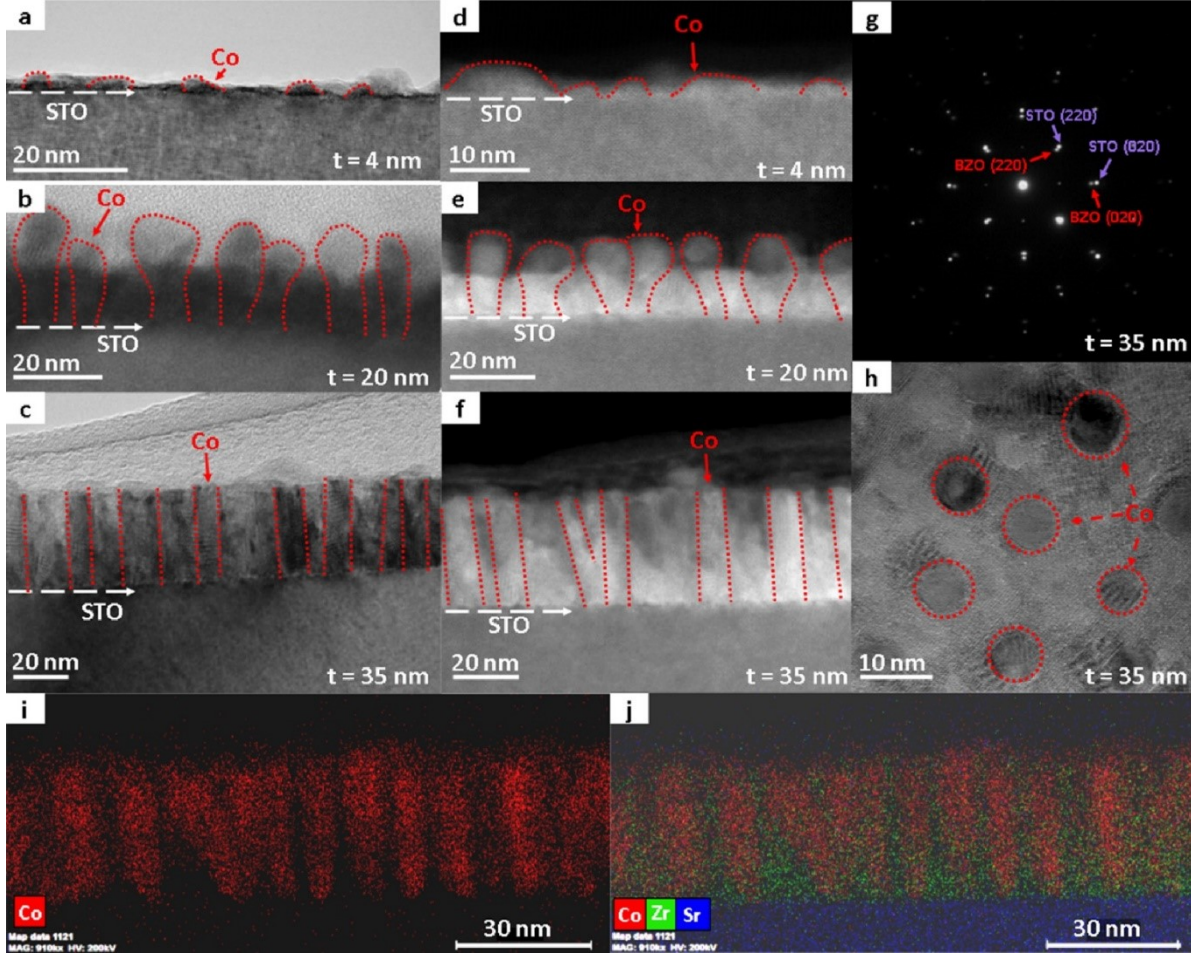


Figure 5.3 Nanostructure study of the Co-BZO samples grown at different thicknesses. a-c. TEM images of the 4 nm, 20 nm, and 35 nm thick samples verifying the thicknesses. d-f) STEM images of the 4 nm, 20 nm, and 35 nm thick samples. g) Selected area electron diffraction (SAED) pattern of the 35 nm thick sample with a h) selected plan view area sample for the 35 nm thick sample. EDS images were taken with a i) Co spectrum map and an j) element map.

To further verify the composition and investigate the epitaxial quality of the Co-BZO samples, TEM study was conducted for all the samples with varying thickness. In Figure 3a-c, low magnification cross-sectional TEM images of the 4 nm, 20 nm, and 35 nm samples are shown. The 4 nm sample presents island growth with the islands being Co and with BZO as the matrix, which is consistent with the XRD data and the EDX data shown in Figure 7a. As the film continues

to grow, as seen in the 20 nm film, the film exhibits Co nanopillars with the top portion protruding through the surface of the film. In contrast, the 35 nm film exhibits a more uniform growth throughout the thickness of the film with more ordered Co regions within the Co-BZO nanocomposite. The structural tuning from Co island to Co nanorods to uniform nanopillar growth arise from the overall interactions between the metal and the oxide adatoms on the substrate. Initially, the Co adatoms nucleate as islands, as seen in the 4 nm sample, due to that the Co and BZO adatoms tend to coalesce due to their different surface energies ($2.595\text{--}3.19\text{ J m}^{-2}$, 1.185 J m^{-2} , and 1.26 J m^{-2} for Co, BZO, and STO, respectively)[192–195] with Co having a higher surface energy when compared to STO. As the growth continues, since the BZO has lower surface energy than STO, the BZO grows layer-by-layer growth. Thus, as the Co island continues to grow, the BZO layer growth continues and form a 2-phase nanocomposite film between the two, as seen within the 20 nm sample. As the film continues to grow thicker, the BZO layer becomes more prominent and forms a smooth 2-phase nanocomposite with Co nanopillars well embedded in the oxide matrix, as seen in the 35 nm sample. Figure 3d-f are the corresponding STEM images of the films obtained in high angle annular dark field (HAADF) mode to further highlight the Co nanostructures within the BZO film. To further verify the growth quality, a typical diffraction pattern of the Co-BZO thin film, shown in Figure 3g, was taken that further shows that cubic BZO grew epitaxially on the STO substrate. To acquire a rough distribution of the Co pillars, a plan view of the 35 nm sample was taken and shown in Figure 3h. The plan-view image shows a regular distribution of Co pillars within the BZO matrix with the pillars having an average diameter of 8 nm. Verifying the phase separation of the Co and BZO, an EDX image of the 35 nm sample was shown in Figure 3i, j to show that Co nanopillars are well separated from the BZO matrix. Overall, the thickness variation results in the structure anisotropy as proposed in the Co-BZO system, with the thinnest having just Co islands with small BZO layers and the thickest, the 35 nm sample, having a film with more uniform thickness with regular Co pillars.

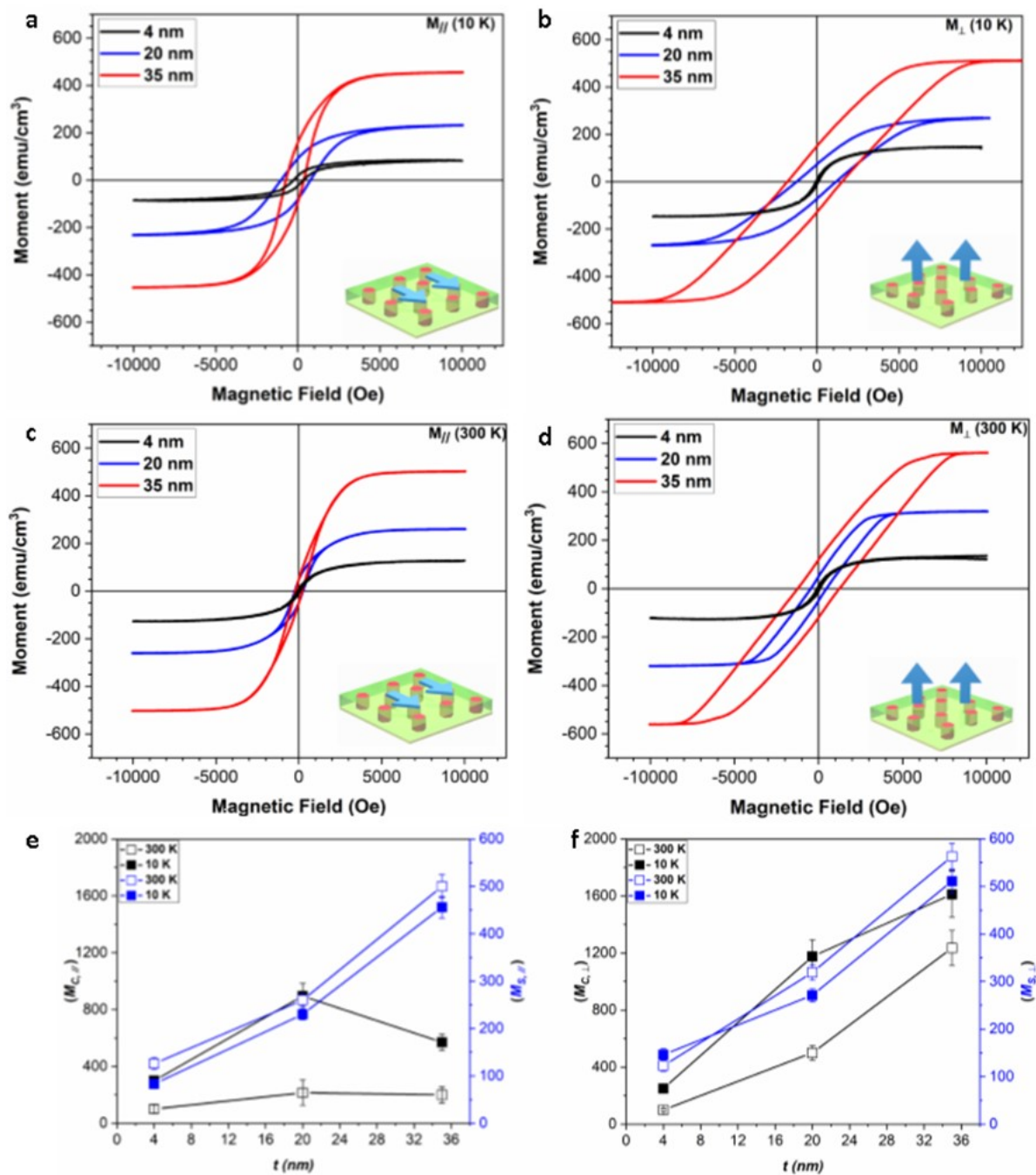


Figure 5.4 Magnetic study of the different films at a, b) low temperatures with in-plane and out-of-plane applied fields, and at c, d) room temperatures with in-plane and out-of-plane applied fields. Further plotting was done on the different coercive fields and magnetic saturations done for e) in-plane and f) out-of-plane applied magnetic fields at low and room temperatures.

5.5 Magnetic Anisotropy of the Different Thicknesses

To investigate how the shape anisotropy affects the magnetic properties of the Co nanostructures in Co-BZO, the magnetic responses of all the samples were measured by VSM in MPMS. Initially, the M-H response was measured at 10 K and 300 K for both the in-plane and out-of-plane directions, as shown in Figure 4a, c and Figure 4b, d respectively. It is important to note that the units on the y axis is emu/cm^3 and the volume used is the entire film as opposed to the volume of only the Co regions. Thus, the actual magnetization values of the Co regions could be much higher than the ones plotted. The overall shape and saturation values of the magnetization data agrees well with previous work of Co-BZO grown on STO35. In the in-plane direction (i.e., parallel to the film surface), it shows a saturation magnetization of 83, 230, 456 emu/cm^3 at 10 K and 126, 260, 500 emu/cm^3 at 300 K for the 4 nm, the 20 nm, and the 35 nm films, respectively. Additionally, comparing to the in-plane properties, the out-of-plane direction (i.e., perpendicular to the surface) shows much stronger magnetic properties, with saturation magnetization of 146, 271, and 511 emu/cm^3 at 10 K and 123, 319, 563 emu/cm^3 at 300 K for the 4 nm, the 20 nm, and the 35 nm films, respectively, showing comparable saturation values from low to room temperature. The very similar MS values are possibly attributed to the weak temperature dependence of M_s in Co from 10 K to 300 K and the strong strain coupling along the vertical oxide-metal interfaces in the samples. Furthermore, in the out-of-plane direction, an obvious increase in coercivity occurs with increasing thicknesses at 10 K with values of 250 Oe, 1175 Oe, and 1612 Oe for the 4 nm, the 20 nm, and the 35 nm sample respectively, and at 300 K with values of 100 Oe, 500 Oe, and 1235 Oe for the 4 nm, the 20 nm, and the 35 nm sample respectively.

As the thickness of the Co-BZO layer increases, the ferromagnetic properties of the samples also vary. In the case of coercive field and saturation magnetization, they increase with increasing thickness. For coercive field specifically, the trend is due to the change in grain size, and domain size. Specifically, if each Co nanostructure is a single magnetic domain when the film reaches magnetic saturation, larger Co nanopillars or nanoparticles will require larger magnetic fields to saturate. As the Co pillars grow in height, the domain sizes increase. This subsequent increase in domain size causes the applied magnetic field required to align the magnetization to increase. In addition, as the temperature increases from low temperature to room temperature, the coercive field decreases dramatically, especially for the thinner samples which is typical for ferromagnetic materials.

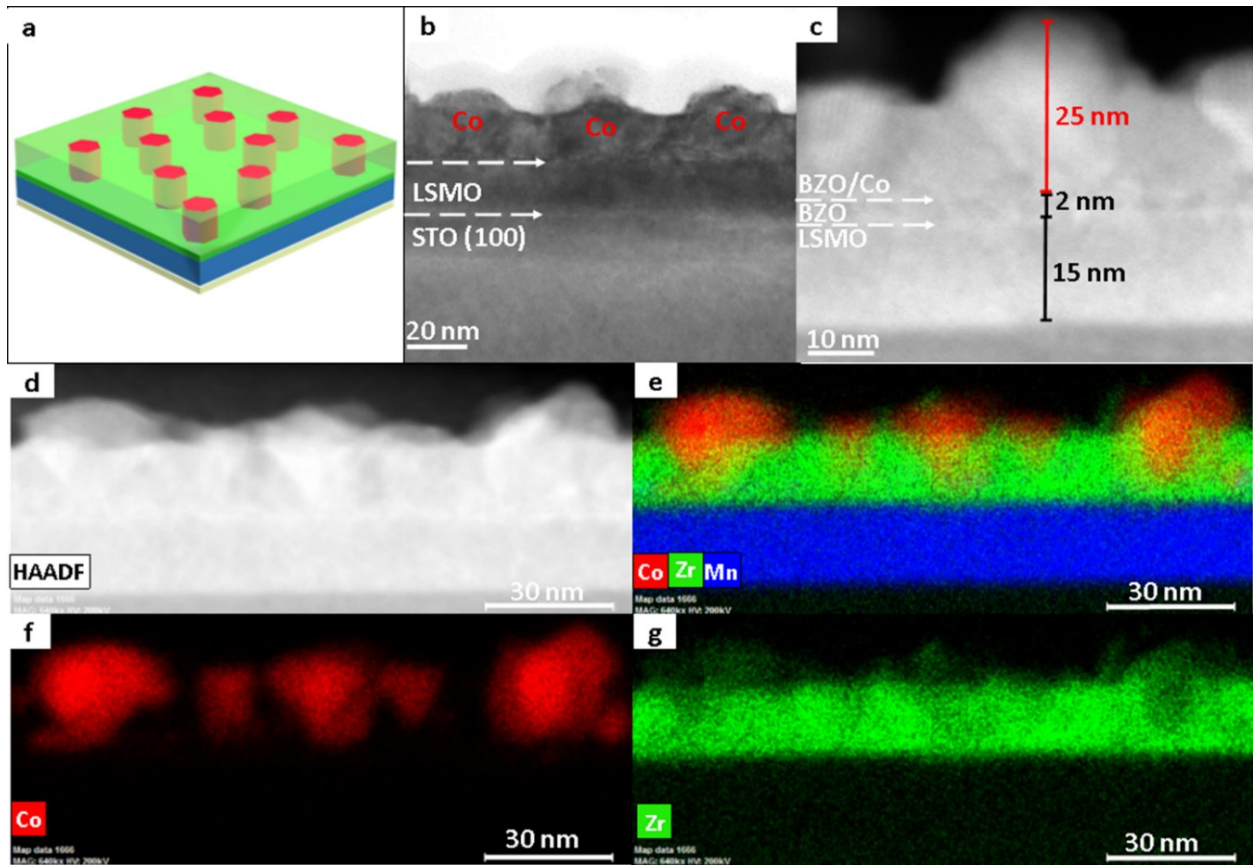


Figure 5.5 Nanostructure study of the device with an a) schematic of the device and its corresponding b) TEM image and c) STEM images. In addition, the d) HAADF was taken with the e-g) corresponding elemental mappings done.

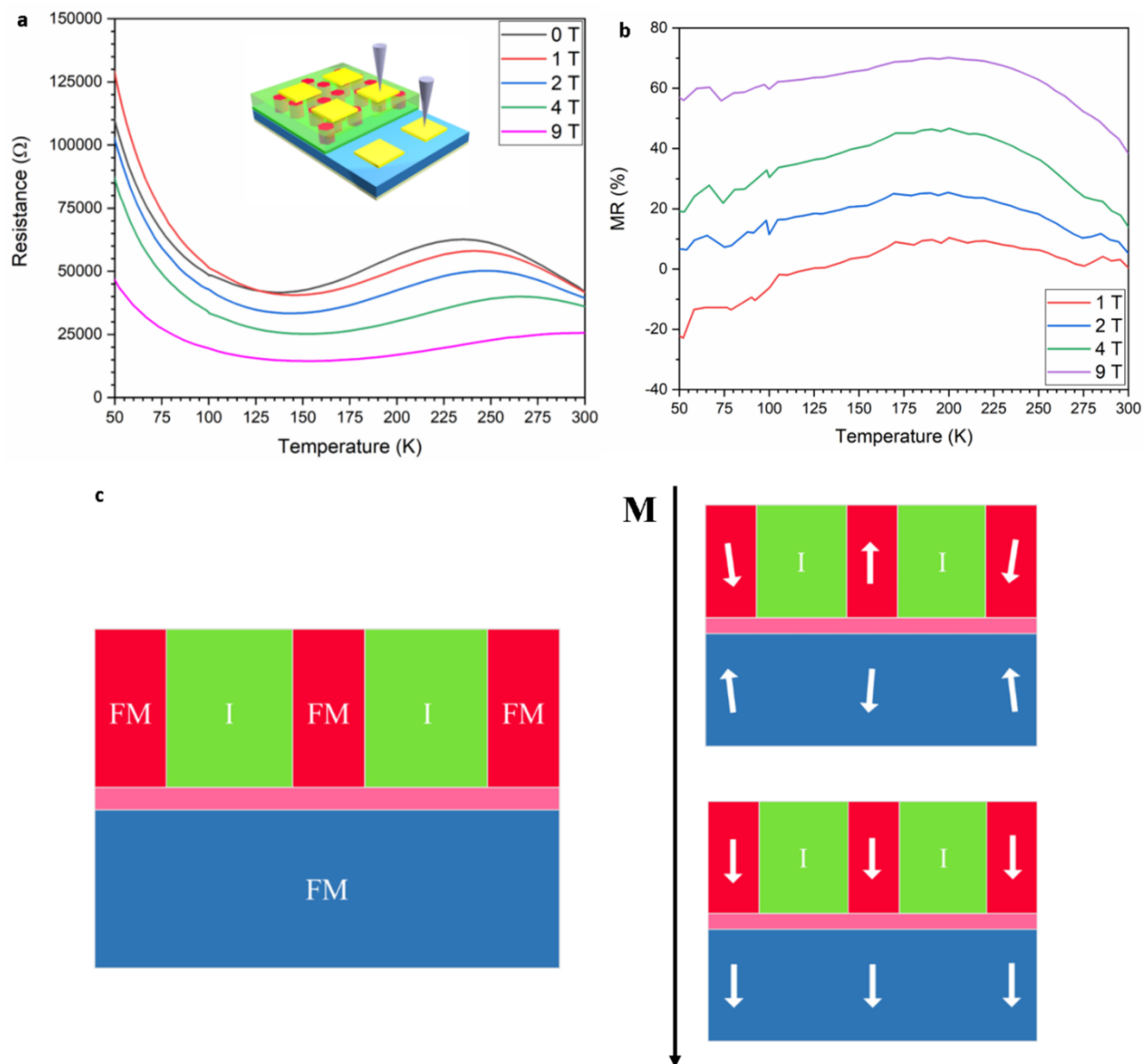


Figure 5.6 Magneto-electrical properties of the device with a) M vs R with varying applied fields with its corresponding b) MR ratios. c) A schematic of how the spins align within the ferromagnetic layers as magnetic fields increase.

5.6 Co-BZO Multilayer Magnetoresistance Change

The Co-BZO nanocomposite film was further integrated into a device for resistive switching and magnetoresistance effects. A Co-BZO sample with the thickness of around 20 nm was selected because of the combination of its soft magnetic properties and its magnetic anisotropy. Figure 5a shows the proposed device structure and TEM, STEM, and EDX of the tunnel junction was shown to verify the growth quality. The 2 nm BZO layer serves as an insulating layer between the two ferromagnetic layers of Co-BZO and $\text{La}_{0.7}\text{Sr}_{0.3}\text{MnO}_3$ (LSMO). BZO was selected owing to its lattice matching of the oxide matrix of Co-BZO. The Co-BZO layer shows similar nanostructure as seen when grown directly on STO. LSMO was selected as the bottom electrode layer due to both its semi-metal conducting behaviour, allowing for a bottom electrode, and its room temperature ferromagnetic behaviour. This configuration allows for the ferromagnetic coupling between the top Co-BZO layer and the lower LSMO, semi-metal layer. Thus, allowing for electrical tunnelling across the interface to be controlled by an applied magnetic field. Since BZO is an effective insulator, temperature will also play a crucial role in the electron transport properties of the multilayer stack. As seen in Figure 6a, the device shows resistance switching with an applied magnetic field that is perpendicular to the film. The resistance was measured from taking R-T measurements from both the top electrode on the Co-BZO and bottom electrode on the LSMO film. The magnetoresistance (MR%) was calculated using Equation (11)[196]. The MR shows correlation between the magnetic field and the resistance with a peak of 10, 25, 47, and 70% under a 1 T, 2 T, 4T, and 9 T, respectively, at a temperature of 200 K.

$$MR = \frac{R_{ap} - R_p}{R_{ap}} \times 100\% \quad \text{Equation (11)}$$

As the magnetic field increases, the MR value increases due to the interaction seen in Figure 6c, where at zero applied field, the magnetic orders for both the top Co-BZO and the bottom LSMO layer are not aligned. Increasing the magnetic field to 1 T results in the Co-BZO reaching magnetic saturation and the LSMO to not be strongly aligned in the out-of-plane direction resulting in higher resistances than at zero applied field as seen in Figure 6a, b. As the applied magnetic field continues to increase, the magnetic domains become more ordered resulting in the ferromagnetic layers to be aligned in the same direction. The increase in ordering allows for electrons to pass through the barrier more readily, which decreases the resistance and causes a

change in magnetoresistance. This is seen by the subsequent increases in the MR% as the magnetic field increases from 1 to 9 T in Figure 6b. The direct correlation between MR and applied magnetic field whereas the field increases the MR increases demonstrates a successful ferromagnetic device that allows for the tuning of resistance via magnetic field. Thus, the growth of Co-BZO VAN on top of a ferromagnetic semi-metal and insulator resulted in a MR change with changing magnetic field. This shows successful integration into a spintronic device and allows potentials for metal-oxide VAN for device applications and, especially as the tunability of the Co-BZO is further investigated, allowing for eventual integration into tunnel junction devices.

5.7 Conclusion

In summary, a strong anisotropic ferromagnetic material, Co-BZO nanocomposite thin films, have been demonstrated with tunable coercive field, and the thin films have been integrated into a spintronic device. Their strong magnetic anisotropy and coercive field tuning properties address the need for low energy, high density, and energetically stable devices. The successful integration of such Co-BZO nanostructure in a device structure opens new avenues for metal-oxide VANs and their future integration into devices towards low power tunnel junction devices and many other spintronic devices.

6. TUNABLE, ROOM TEMPERATURE MULTIFERROIC FE-BATIO₃ VERTICALLY ALIGNED NANOCOMPOSITE WITH PERPENDICULAR MAGNETIC ANISOTROPY¹⁸

6.1 Summary

Room-temperature ferromagnetic materials with perpendicular magnetic anisotropy are widely sought after for spintronics, magnetic data storage devices, and stochastic computing. To address this need, a new Fe-BaTiO₃ vertically aligned nanocomposite (VAN) has been fabricated—combining both the strong room-temperature ferromagnetic properties of Fe nanopillars and the strong room-temperature ferroelectric properties of the BaTiO₃ matrix. Furthermore, the Fe-BaTiO₃ VAN allows for highly anisotropic magnetic properties with tunable magnetization and coercivity. In addition, to demonstrate the multiferroic properties of the Fe-BaTiO₃ system, the new metal-oxide hybrid material system has been incorporated in a multilayer stack. This new multiferroic VAN system possesses great potential in magnetic anisotropy and property tuning and demonstrates a new material family of oxide-metal hybrid systems for room-temperature multiferroic material designs.

6.2 Introduction

Ferromagnetic thin films are well studied materials with a wide-range of applications in electronic devices[179], especially in spintronic devices[151]. One such spintronic device, the magnetic tunnel junction, uses magnetically susceptible materials to alter electron currents to enact a resistance change[150]. For these applications, Fe, a strong ferromagnetic metal, has been well studied and integrated into a variety of spintronic devices and applications, most notably in tunnel junctions[62,166,197]. Traditionally, tunnel junctions have a preferred in-plane (IP) direction, but perpendicular anisotropy is highly desired for vertical tunnel junction development owing to these tunnel junctions having higher frequency, higher density, and lower power requirements. For these vertical tunnel junctions, work is needed to develop magnetic materials that exhibit a perpendicular anisotropy[6,176]. In addition, the magnetic material must present a perpendicular anisotropy with

¹⁸This chapter is reprinted with permission from “Tunable, Room Temperature Multiferroic Fe-BaTiO₃ Vertically Aligned Nanocomposite with Perpendicular Magnetic Anisotropy” by B. Zhang, et al., *Mat. Today Nano.*, **2020**, 100083. © 2020, Elsevier

a small enough feature size allowing for integration into current integrated circuits. A promising platform that addresses both needs of creating small feature sizes and a strong perpendicular magnetic direction is vertically aligned nanocomposites (VANs)[137].

VANs enable the single-step growth of two different materials that are self-assembled into two-phase vertical structures, including pillar-in-matrix and nanocheckerboard structures[123,133,134,189,198]. The VAN structures present two main advantages compared with the traditional, single-phase films. First, the unique, vertical pillar structure creates highly anisotropic physical properties while accommodating significant amounts of vertical interfacial strain between the two phases. This interaction creates a large degree of property tunability[198–201]. Second, because VANs typically consist of two different phases, the structure introduces the possibility of combining two materials with highly desirable properties into a hybrid material. To this end, it has been shown that it is possible to combine ferroelectric oxides and ferromagnetic oxides to form multiferroic films[134,190,199,202]. Although VANs consisting of two oxide phases with desired properties have been widely demonstrated, metals have been long sought after for their strong, room-temperature, ferromagnetic properties, which are typically much stronger than their oxide counterparts. Thus, by replacing one of the oxide phases with metals, such VAN films could present strong anisotropic, metallic, physical properties under room-temperature conditions[138,202–205].

Metal oxide-based VANs are uniquely equipped for multiferroic material designs owing to their ability to combine both oxide and metal phases and their respective properties. Various metal-oxide VAN systems, including Ni-CeO₂[137], Ni-Ba_{0.8}Zr_{0.2}Y₃[138], Co-BaZrO₃[123], Fe-La_{0.5}Sr_{0.5}FeO₃[191], Au-BaTiO₃[139], and Au-TiO₂[140], have previously demonstrated that the integration of metals with oxides that have relevant room-temperature properties is possible. These metal-oxide VANs integrate either the strong plasmonic or the ferromagnetic properties of the metal phase with the oxide phase to create a highly anisotropic material system.

To achieve excellent epitaxial quality of the two phases, a new epitaxial paradigm for the two-phase nanocomposite system was used[135] for this work, i.e., the two phases shall present opposite strain states when compared with the substrate lattice. For this work, BaTiO₃ (BTO) was selected as the matrix, and Fe was selected as a magnetic secondary phase, as shown in Fig. 1a. With BTO being one of the most well-studied ferroelectric oxide[206–208], it has recently

attracted interest owing to its non-linear optical properties [209–212], and its potential applications in different optical devices[213,214], especially wave guides[215,216].

Despite the previous work on Fe-BTO nanocomposite systems, wherein the geometries have been focused on bilayer, multilayer films with Fe on BTO or vice versa[217–220], or on embedding Fe nanoparticles within a BTO matrix[221], this work proposes integrating Fe as nanopillars into a BTO matrix. This proposed structure will allow for unprecedented strong anisotropic, ferromagnetic and ferroelectric properties, coming from Fe and BTO, respectively. In addition, this unique structure will incorporate large vertical interface strain that will enhance coupling between the Fe and BTO phases. For the Fe-BTO nanocomposite system, a large range of tunability will also be achieved, such as going from a soft ferromagnet to a hard ferromagnet, by simply controlling the Fe pillar length (i.e., film thickness), pillar density, and pillar morphology. Such tunable nanoscale ferromagnetic systems could find a wide range of applications in spintronic devices and neuromorphic computing[222], and are a promising candidate for the on-going search for soft magnetics for stochastic computing schemes[223,224].

6.3 Methods and experimental

The Fe-BTO target preparation was made by mixing Fe and BTO powders in a 1:1 M ratio. The mixture was pressed and sintered with inflowing Ar/H₂ into a conventional pellet target. The films were grown on single-crystalline SrTiO₃ (STO) (001) substrates via the pulsed laser deposition system (KrF excimer laser) (LambdaPhysik, $\lambda = 248$ nm). Multiple deposition frequencies of 2 Hz, 5 Hz, and 10 Hz were used to tune the nanostructure.

The nanostructure of the films was investigated using X-ray diffraction (XRD) (Panalytical X'Pert X-ray diffractometer). The different films were imaged by transmission electron microscopy (TEM) and scanning transmission electron microscopy (STEM), and energy dispersive X-ray spectroscopy (EDS) elemental mapping was performed by using a FEI Titan G2 80-200 STEM with a Cs probe corrector and ChemiSTEM technology (X-FEG and SuperX EDS), and additional TEM, STEM, and EDS images of the different frequencies were taken (FEI Talos-200X).

The magnetic properties of the nanocomposite thin films were analyzed both parallel (IP) and perpendicular (out-of-plane [OP]) to the film surface in the vibrating sample mode in a Magnetic Property Measurement System (MPMS 3, Quantum Design). The piezoelectric

properties were measured by Bruker atomic force microscopy. Magnetoelectrical (ME) coupling was measured using a magnetoelectric bundle (Radiant Technologies, Inc.).

Dielectric permittivity was calculated using a spectroscopic ellipsometer (JA Woollam RC2), with an anisotropic model to fit the ellipsometer parameters ψ and Δ . The IP permittivity was modeled using two Lorentz oscillators, whereas OP permittivity was modeled using a Drude-Lorentz model to enforce Kramers-Kronig consistency.

6.4 Results and discussion

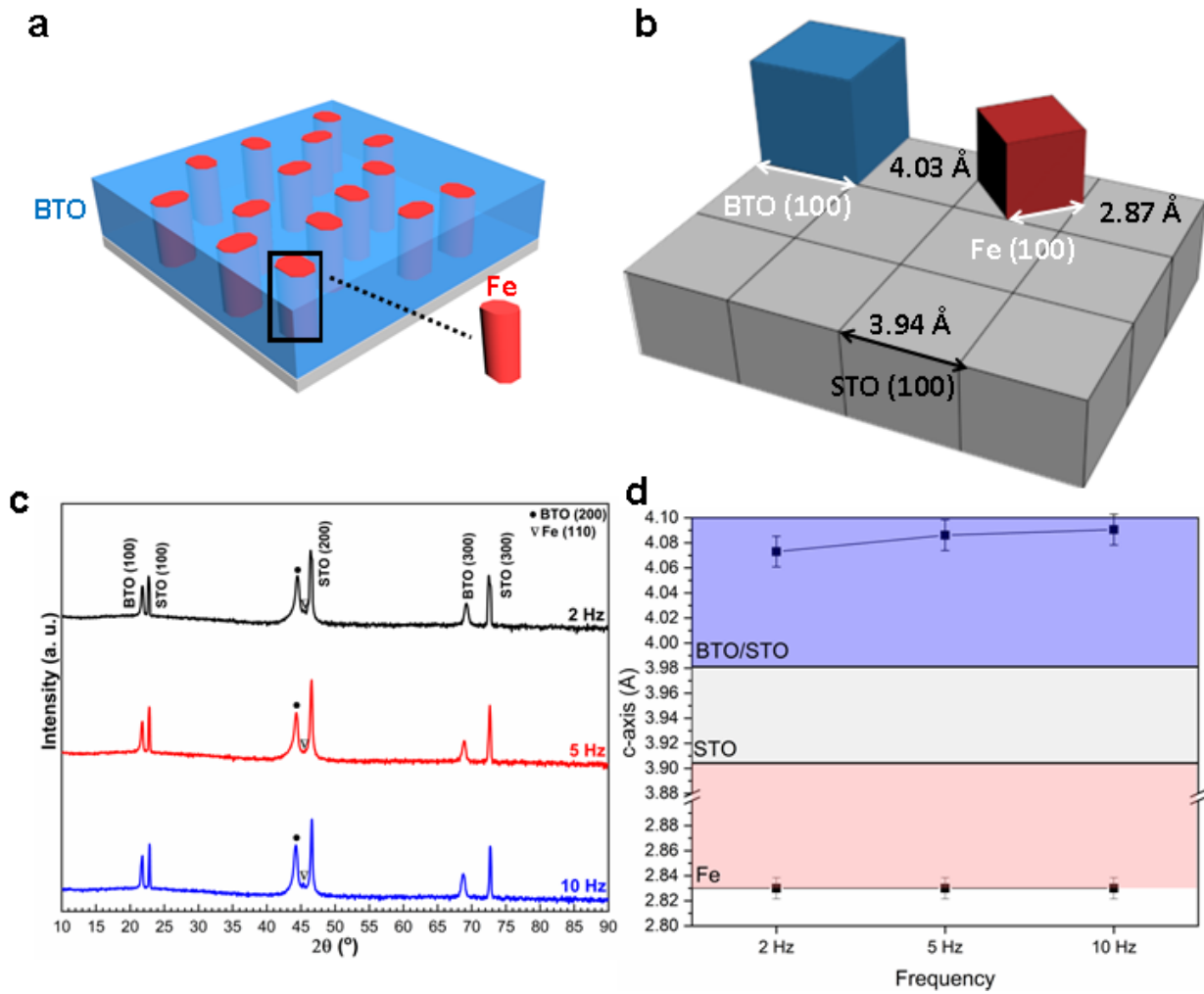


Figure 6.1 a) Schematic demonstrating the proposed growth of Fe pillars within a BTO matrix. b) Schematic showing the different lattice parameters of BTO and Fe on STO. c) Typical θ -2 θ XRD scan of the different films deposited at different frequencies. d) The different lattice parameters for BTO and Fe grown at different frequencies.

θ - 2θ XRD scanning was first performed on the Fe-BTO VAN thin films grown under different laser frequencies (2 Hz, 5 Hz, and 10 Hz) to investigate the material composition and the phase distribution. From the XRD data, BTO (001) and STO (001) peaks can readily be identified from Fig. 1c in all samples indicating (001) BTO texturing on the (001) STO substrate. In addition, for all samples, the Fe (110) peaks exist at a 2θ value of 45.3° corresponding to a d-spacing of 2.00 Å, indicating a compressive strain of 1.3% compared with reported bulk Fe d-spacing (PDF card# 06-0696) of 2.0268 Å. Meanwhile, the BTO (200) peaks shifts from 44.45° to 44.3° to 44.25° for the 2, 5, and 10 Hz samples, respectively, corresponding to a tensile strain of 2.3%, 2.7%, and 2.8% when compared with the measured BTO (200) peak located at 45.55° in pure BTO/STO samples, with the lattice parameter as seen in Fig. 1b. This highly strained state is created via the two different materials within the metallic VAN forming distinct areas and hints at a strong interface strain between Fe and BTO, with the strong BTO tensile strain compensating for the large Fe compressive strain. In addition, as the laser frequency varies, the BTO peak position shifts, indicating a morphology change, with the lowest frequency having the least tensile strain and the highest frequency with the highest tensile strain.

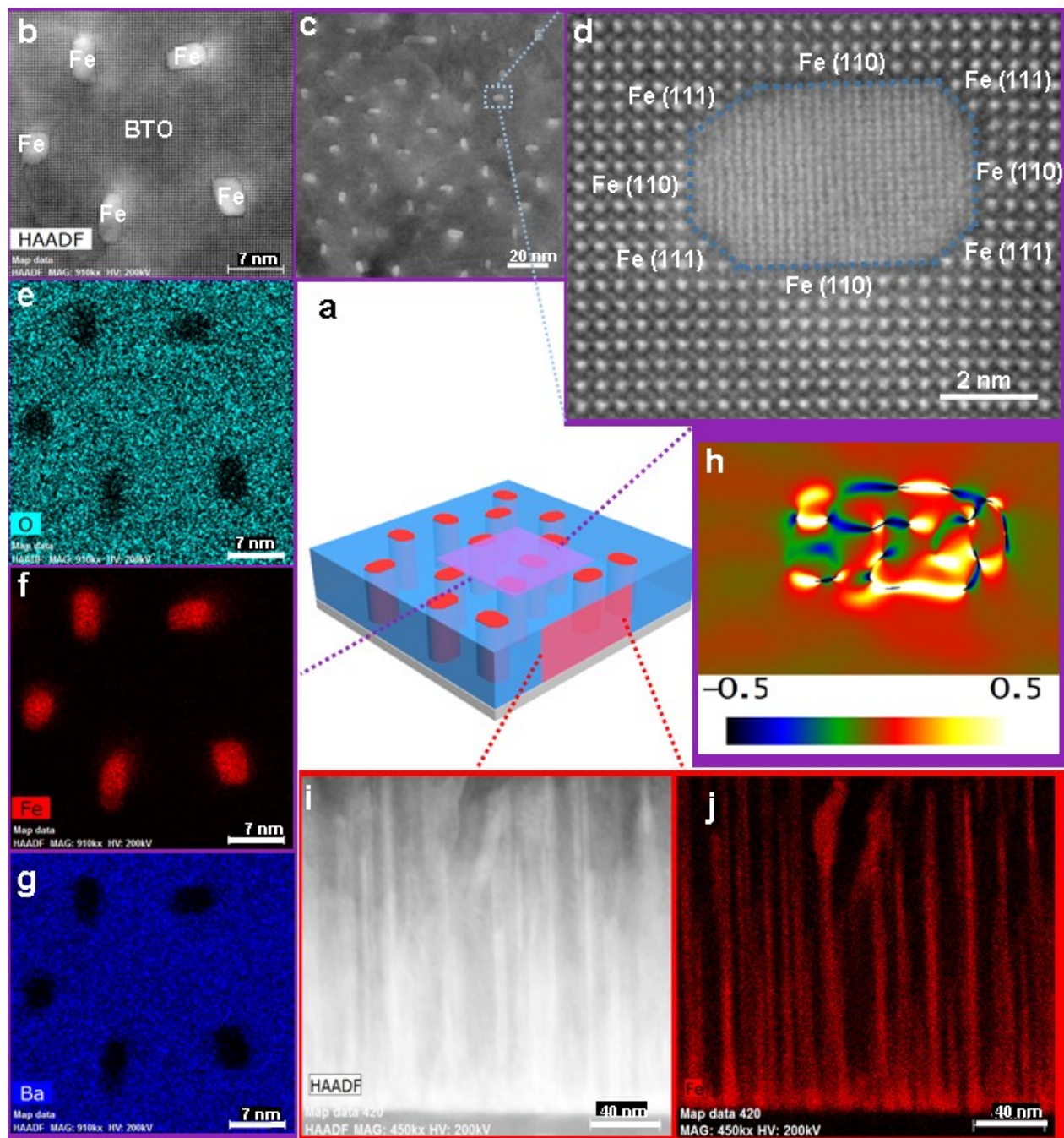


Figure 6.2 Schematic demonstrating the Fe-BTO film grown on STO. b-d) Plan view STEM images of Fe-BTO grown at 10 Hz. EDX mapping of the plan view images of Fe-BTO with e) O, f) Fe, and g) Ba mapping shown. h) GPA analysis of a single pillar to illustrate the strain distribution. i) and j) The STEM and Fe EDX mapping respectively of a cross-sectional view.

To verify whether the frequencies affected the nanostructure, TEM, STEM, and EDS analyses were conducted. The expected morphology of the Fe-BTO nanocomposite is illustrated in Fig. 2a, wherein uniformly distributed Fe nanopillars grow within a BTO matrix. The plan-view STEM images in Fig. 2b–d demonstrate the excellent epitaxial growth of the film, with the average pillar diameter of around 5 nm. The pillars show an overall shape of a rectangle, with sides being in the $\{110\}$ plane family and with faceted edges being the (111) planes. Fig. 2e–g presents the chemical composition of the nanocomposite with Fe pillars in the BTO matrix. The rectangular shape with facets can be explained by the strain mapping results using geometrical phase analysis (GPA) in Fig. 2h. The GPA analysis of the individual pillar shows an alternating pattern of strain states between tensile (yellow) and compressive (blue) strain. This alternating strain states serve to minimize the total strain energy of the Fe region with alternating strain states. On a closer look, it reveals that the smaller facets have a singular strain state, with the larger one having a combination, resulting in the faceted rectangular shape.

The cross-sectional images in Fig. 2i of the Fe-BTO film demonstrate the high uniformity and high density of the Fe pillars within the BTO matrix, and on further investigation, they demonstrate highly oriented growth, with the pillars growing in a vertical fashion throughout the film thickness. To demonstrate phase separation, EDS mappings in Fig. 2j again confirm the pillars throughout the film thickness were indeed pure Fe, not iron oxide. This is significant owing to the high susceptibility that different metals—especially ferromagnetic ones such as Fe, Ni, and Co—are likely to oxidize. For Fe, the oxidation process is highly detrimental to physical properties, e.g., resulting in smaller coercive fields, magnetic saturation, and a critical temperature significantly lower than room temperature. In addition, from the plan-view images, it is possible to ascertain the high density of Fe regions that exist with the Fe-BTO film and the uniformity of the distribution throughout the film. This regular distribution is highly sought after for future device applications, allowing for easier fabrication of device arrays. The Fe nanopillars are nearly equally spaced resembling an Fe nanoarray, which could be patterned as arrays of spintronic devices.

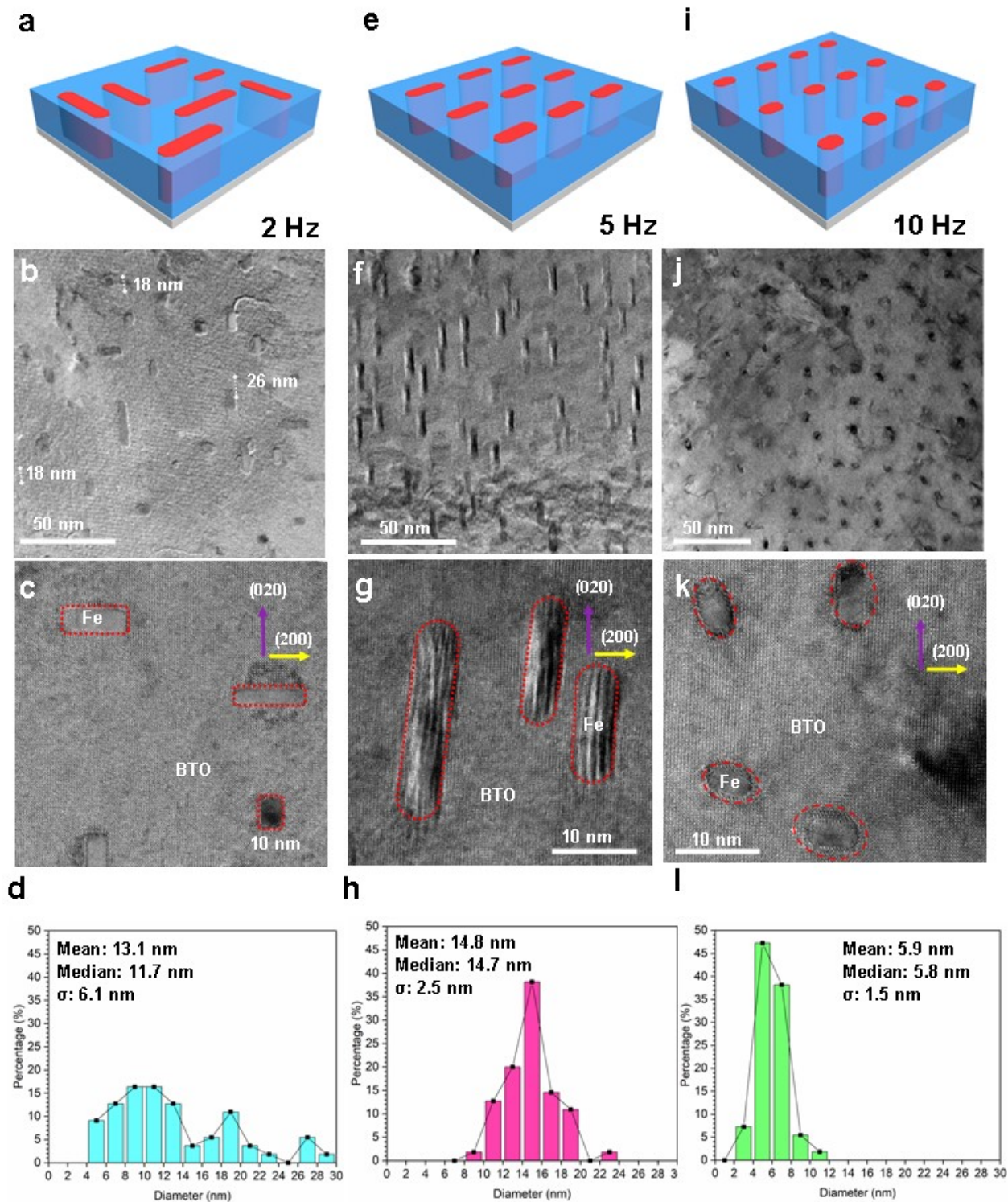


Figure 6.3 Schematic demonstrating the how the pillar diameters vary with different frequencies. b, c, f, g, j, and k) Plan view TEM images demonstrating the pillar variation. d, h, and l) Histogram plots illustrating the nanopillar diameter distribution for the samples deposited under different laser frequencies.

To further investigate the underlying growth mechanisms of the Fe-BTO hybrid film, different laser frequencies of 2 Hz, 5 Hz, and 10 Hz were used to grow the Fe-BTO films. In the TEM plan-view images in Fig. 3b–k, it is noted that as frequency increases, Fe dimension changed from isotropic morphology to elongated rectangles and then again to squares. While there is a typical Gaussian distribution for the 5-Hz and the 10-Hz samples, the 2-Hz sample does not present such distribution. Instead, it shows a bimodal distribution of nanopillar diameters, i.e., the mixture of large-and small-diameter nanopillars. Such non-uniform nanopillar diameters might be attributed to the non-optimum growth and incomplete nucleation owing to the insufficient flux of Fe adatoms under 2 Hz. This leads to the formation of small nuclei of Fe nanopillars in Fig. 3b–d. The 5-Hz sample has unique rectangular shaped nanopillars with preferred orientation along the IP direction of BTO [010]. The preferred orientation suggests that there is an underlying factor during the growth and nucleation of the Fe adatoms within the Fe-BTO film. One possible explanation may be the interaction between the lattice strain and the adatom diffusion process. When frequency decreases, the adatom diffusion time increases, and the adatoms have sufficient time to diffuse in both the (110) directions, producing an elongated, faceted, rectangular, IP morphology in the 2-Hz sample. For the 5-Hz sample, the diffusion time is in the range allowing the perfect alignment along a preferred crystallographic plane of [020]. This alignment mainly arises from interactions between the surface energies of the Fe, BTO, and STO substrate and the growth kinetics, which mainly include the incoming flux of adatoms and the nucleation and diffusion of the adatoms. More specifically, diffusion of the adatoms and the perfect nucleation/growth of the adatoms have been achieved under the 5-Hz growth condition. The strain compensation model suggests that Fe ($a = 0.287$ nm) and BTO ($a = 0.483$ nm) present opposite strain states compared with the STO substrate ($a = 0.394$ nm). Such IP strain compensation leads to the highly ordered, uniform distribution of Fe nanopillars within the BTO matrix. Such a strain compensation model can be best demonstrated in perfect epitaxial growth of 2-phase VAN systems. Thus, highly ordered and aligned Fe nanopillar distribution has been achieved in the 5-Hz sample. However, the 2-Hz sample clearly shows both very small nanopillars and regular-sized nanopillars (a bimodal distribution), which suggest that there might be insufficient Fe adatoms under the 2-Hz condition and thus leads to various nanopillar diameters. Although 10 Hz leads to high growth rate, it could cause deterioration of epitaxial quality and pillar distribution.

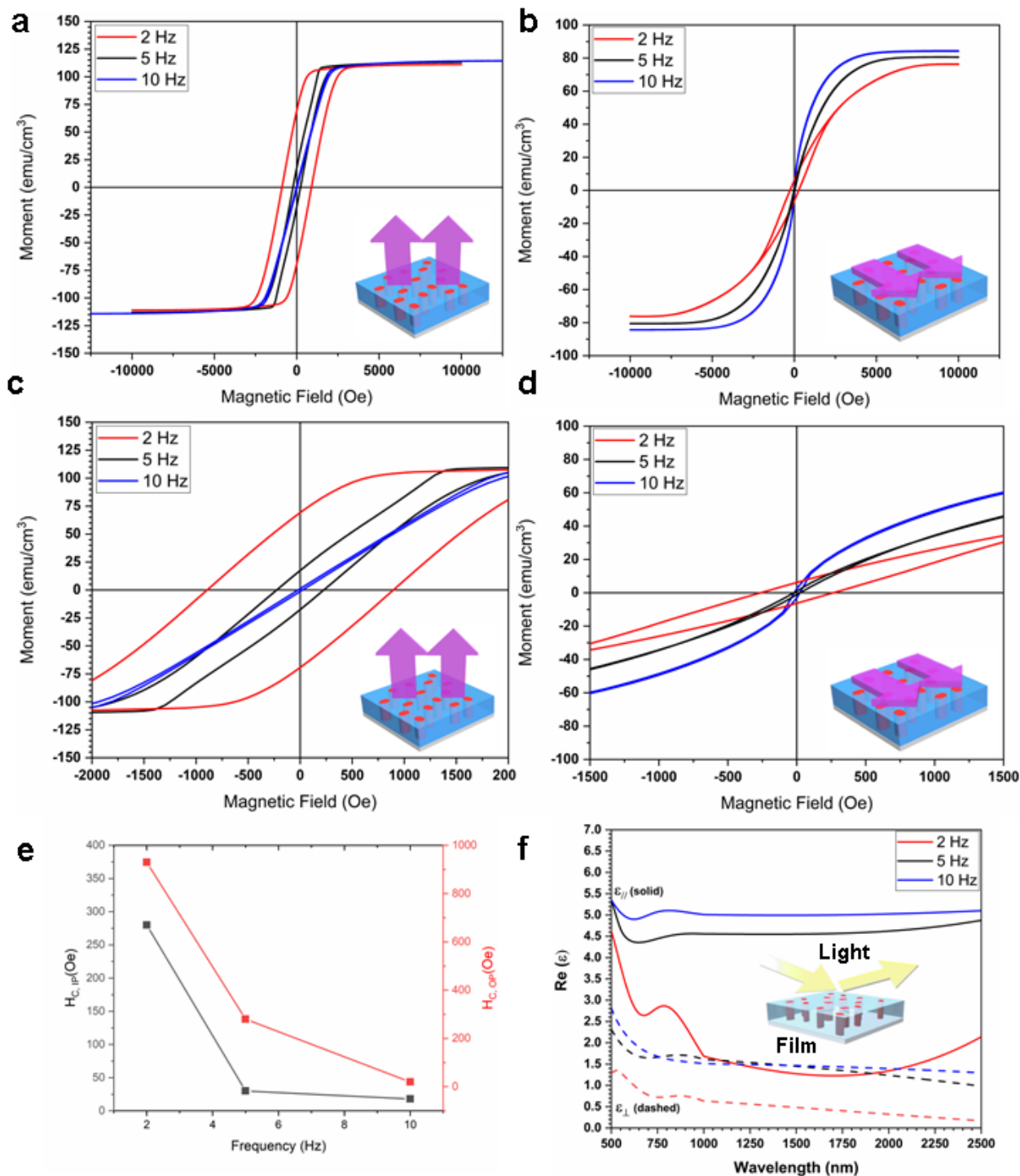


Figure 6.4 a,b) Hysteresis loops of the Fe-BTO films grown at different frequencies with c and d) graphs magnifying the magnetic moments around the coercivities. e) Graph depicting the relationship between the coercivities for both in-plane and out-of-plane with deposition frequency. f) Different dielectric constants of the different frequencies as modeled using data from ellipsometer.

To investigate how Fe nanostructures with the BTO matrix affect the magnetic and optical properties, magnetization measurements and ellipsometry measurements were conducted, and the data are summarized in Fig. 4. The room-temperature ferromagnetic properties for both the OP and the IP were measured and plotted in Fig. 4a and b, respectively. The data show an obvious anisotropy with the OP saturation magnetization of 110 emu/cm^3 and the IP saturation of $70\text{--}80 \text{ emu/cm}^3$. In the OP direction, a clear coercive field difference is seen, with the 2-Hz sample having the highest coercive field and the 10-Hz sample having the lowest coercive field value. In addition, the IP direction shows a similar trend as that of the OP results, and the overall coercive field results are plotted in Fig. 4e. Fe-BTO not only has strong tunable ferromagnetic properties but also possesses highly anisotropic dielectric properties owing to its inherent column shape of nanostructures causing a similar column shape of BTO. From the real part of dielectric permittivity, shown in Fig. 4f, it shows that the IP dielectric permittivity value is significantly higher (between 1.5- and 2-fold) than that of the OP direction. In addition, the growth frequency and the dielectric constants have seem to be correlated in that as the frequency decreases, the dielectric constant also decreases. These trends can be explained from morphology tuning. As frequency decreases, adatom diffusion increases and the dimension of the Fe nanopillars increases. If each Fe region is taken as a single magnetic domain, as length increases, the required energy to saturate and bias the magnetic moment of the Fe region increases with size. In addition, it has been previously reported that the superparamagnetic limit of Fe nanoparticles is around 10 nm [225]. Although the Fe pillars have a diameter of less than 10 nm , they may still be ferromagnetic owing to their pillar-type morphology. As the diameter increases above the limit, coercivity of Fe increases, which affects the IP and OP coercivity. The 2-Hz Fe-BTO sample has a larger coercive field owing to the existence of several larger lateral Fe domains that may be affecting the magnetization of neighboring pillars. As in the case of the saturation magnetic values, since the concentration of the Fe remains constant at 1:1 for the Fe to BTO ratio and all the different frequencies were grown with comparable film thicknesses, similar amounts of Fe will be found within all the films, resulting in similar saturation magnetic values. In a similar manner the diameter affects the magnetic behavior, the optical property is also affected. As the pillars elongate in diameter, there will be more metallic characteristics leading to a lower overall dielectric constant of the system in both the IP and OP directions. The anisotropy can be explained from the fact that the metals are in pillar fashion; the Fe-BTO system will behave more metallic in the OP direction, resulting in a

lower permittivity than that of the IP direction. Overall, the fact that varying deposition frequency was able to tune both the optical and ferromagnetic behaviors further highlights the potential of the unique Fe-BTO VAN systems for future optical and magnetic device applications.

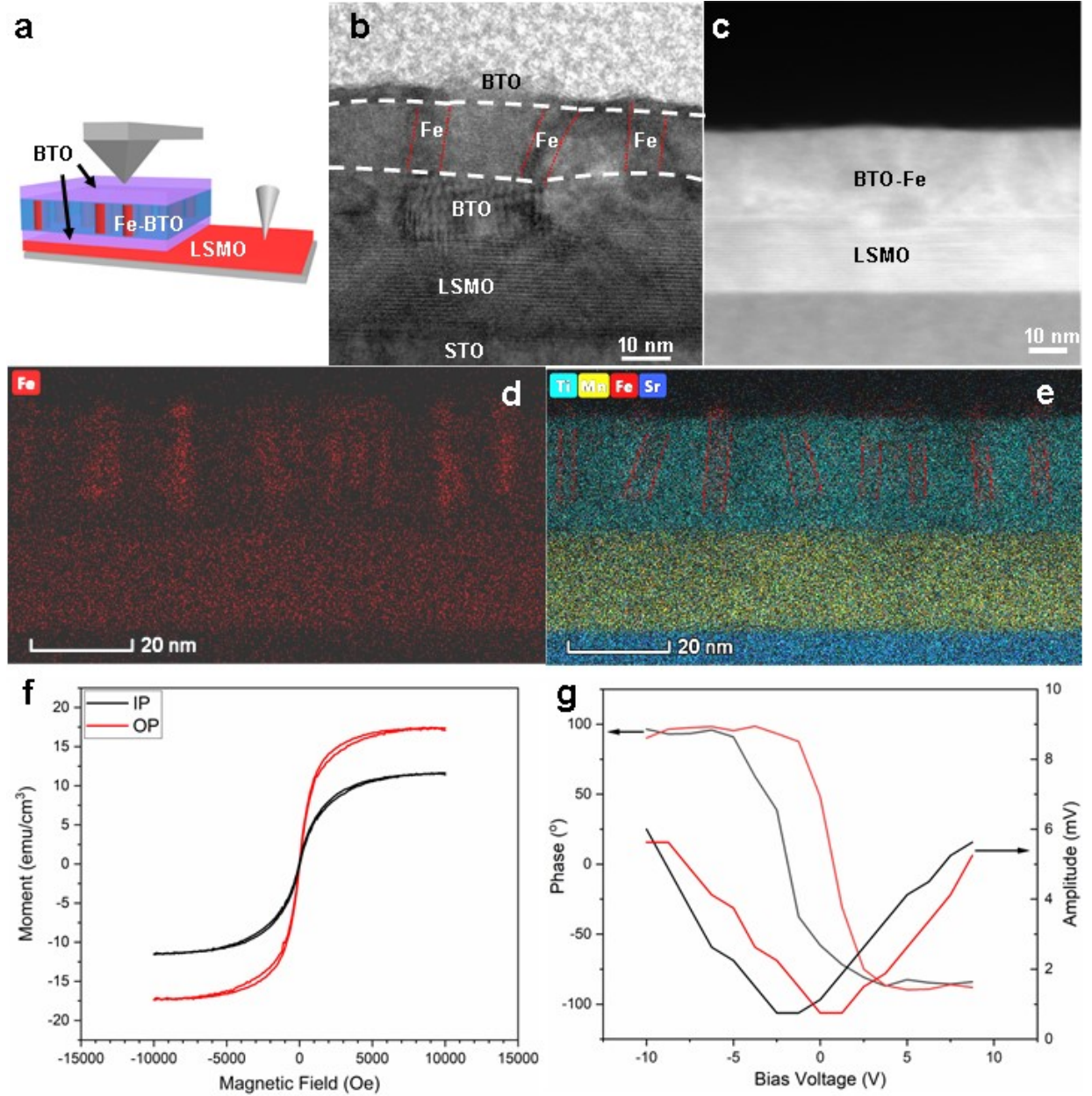


Figure 6.5 a) Schematic of the multi-layer used to isolate the Fe regions within the film from the bottom conductor. b) TEM and c) STEM images of the multi-layer. d) and e) EDX mapping of the multi-layer with the f) ferromagnetic and g) ferroelectric properties.

To demonstrate the potential multifunctionality of the Fe-BTO film, a multilayer stack was grown, with BTO encapsulating the Fe-BTO film to electrically isolate the Fe regions from the conductive bottom $\text{La}_{0.7}\text{Sr}_{0.3}\text{MnO}_3$ (LSMO) layer, as shown in Fig. 5. It is clear that the BTO region isolated the Fe portions from the semimetal LSMO, facilitating the polarization of the BTO regions in the Fe-BTO nanocomposite. This configuration allows for room-temperature ferroelectric and ferromagnetic properties to occur within the device. As shown in Fig. 5, it is possible to see the different ferromagnetic and ferroelectric properties to confirm that the multilayer device has both properties. The ferromagnetic properties also show anisotropy with the coercive field, differing from the OP and IP directions. Compared with the single-layer Fe/BTO films, wherein Fe and BTO are grown in layers on top of one another, the properties show OP anisotropy, as seen in the ferromagnetic and optical data, demonstrating anisotropic ferromagnetic and ferroelectric properties. This multistack configuration allows for two main applications compared with the single-layer film: isolating the metallic regions for individual biasing of different metal pillars, creating local electrical polarization and switching, and room-temperature magnetic switching throughout the film. In addition, the weak ferromagnetic properties and weak ferroelectricity will affect each other, causing highly anisotropic, room-temperature coupling of both electrical and magnetic properties. To further investigate the coupling, a ME coupling measurement was performed, with the results plotted in Fig. 6. In the plot, a black line shows the linear fitting analysis, with the slope indicating a ME charge coefficient, α , of around $1.02 \times 10^{-4} \mu\text{C}/(\text{cm}^2 \text{ Oe})$. Because the ferroelectric properties and polarization mainly come from BTO, a previously reported, room-temperature relative permittivity of BTO was used[226]. The calculated ME voltage coefficient is $2.30 \text{ V}/(\text{cm Oe})$. Owing to magnetization limitations, the slope does not change in the measured range. This coupling creates new avenues for potential applications in spintronics and the stochastic computing scheme.

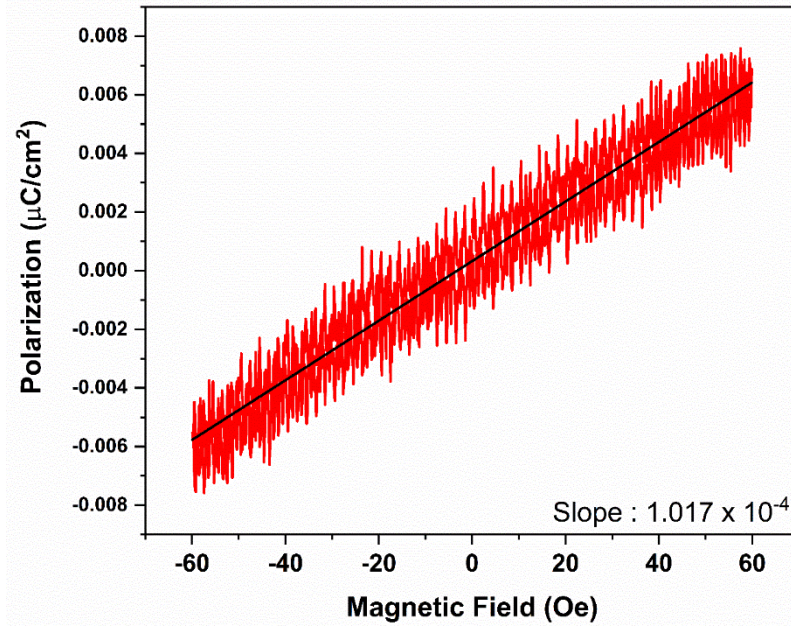


Figure 6.6 Room temperature polarization vs applied magnetic field with the black line representing the linear fit for the data.

6.5 Conclusions

This study demonstrates the growth of Fe nanopillar arrays within a BTO matrix with room-temperature multiferroic properties. By tuning the growth parameters, it is possible to modify the nanostructure, and effectively tune the strain and the magnetic properties. This study found that lower deposition frequencies result in Fe pillars with larger diameters, both lower vertical strain coupling and higher magnetic coercive fields; whereas for higher frequencies, it leads to smaller pillar diameters, higher vertical strain coupling, and lower coercive fields. Furthermore, to demonstrate the potential of room-temperature multiferroic nanocomposites, a multilayer stack with an encapsulated Fe-BTO layer was shown to demonstrate the potential by electrically isolating the Fe regions from one another, aiding the polarization of the ferroelectric BTO regions. This Fe-BTO VAN film presents a platform for highly anisotropic, room-temperature multiferroic properties, with a wide range of tunability for various electrical, magnetic, and optical devices.

7. AU ENCAPSULATED FE NANORODS WITH TUNABLE MAGNETIC OPTIC PROPERTIES

7.1 Summary

Materials with magneto-optic coupling properties are highly coveted for their potential applications ranging from spintronics and optical switches to sensors. In this work, a new, three-phase Au-Fe-La_{0.5}Sr_{0.5}FeO₃ (LSFO) hybrid material in a vertically aligned nanocomposite (VAN) form has been demonstrated. The three-phase hybrid material combines the strong ferromagnetic properties of Fe and the strong plasmonic properties of Au and dielectric nature of LSFO matrix. More interestingly the immiscible Au and Fe phases form Au-encapsulated Fe nanopillars, embedded in the LSFO matrix. Novel properties including anisotropic optical dielectric properties, plasmonic properties, magnetic anisotropy, and room temperature magneto-optic Kerr effect (MOKE) coupling are demonstrated. The novel immiscible two-metal coupling (i.e., Au and Fe) in the complex hybrid opens up exciting new potentials for future three-phase VAN systems with more versatile metal selections.

7.2 Introduction

Magneto-optic materials can effectively utilize light propagation to tune the magnetic spins in materials; the reverse can occur in that an applied magnetic field can affect the propagation of light through the materials. These materials have recently attracted attention due to their proposed roles in a variety of different applications such as spintronics[12,227,228], waveguides[229,230], and optical sensors[231,232]. As the demands for high performance, low energy consumption, and compact devices rise, there is a crucial and pressing need to develop novel materials for effective magneto-optic coupling. To this end, various magneto-optic coupling materials have been fabricated, such as single-phased thin films (e.g., Fe and Ni) [233–235], multilayer films (e.g., Fe/Cr/Fe and Au/Co/Au) [236,237], and nanostructured films (e.g., split-ring nanoantennas) [167,238]. Among these candidates, nanostructures with magneto-optic coupling have received considerable interest due to their unique geometry that are used in applications such as label-free detecting in biosensors[110,239] and high-speed applications in communication devices[230,240]. These nanostructures typically consist of either one or multiple metals fabricated into different

arrays consisting of nanodisks[241–243], nanoparticles[244,245], or nanorods[12,246]. By fabricating these metals into different nanostructures, their plasmon response is enhanced and new functionality emerges[247]. Typically lithography and multistep growth are used to fabricate these different structural arrays[248–250].

Vertically aligned nanocomposites (VAN) present an alternative approach for processing complex nanostructures[251]. VANs can be deposited using a single-step, self-assembly process, and consist of two different phases arranged into a checkboard pattern or pillar-in-matrix form[252,253]. Traditionally, VAN consists of two oxide phases coupled together, with one oxide having strong physical properties, and the other oxide having strong vertical strain that couples with the primary phase[135,251]. Due to their unique vertical structure, VANs have a couple of main advantages compared to conventional oxide thin films, such as highly anisotropic geometry and unique physical properties without any patterning or strict growth control[202,203], and multifunctionalities, e.g., multiferroism[134,163,254,255]. In addition to the significant amount of work in oxide-oxide VANs, a new class of oxide-metal VANs, such as Co-BaZrO₃, Au-BaTiO₃, Ni-BZY, have recently emerged[138,140,143,204,256–260]. Compared to the traditional oxide-oxide systems, oxide-metal VANs include a dissimilar metallic phase that when combined with leads to stronger, anisotropic properties, especially in the cases of ferromagnetic and plasmonic properties. Different from the previously reported metal pillars fabricated utilizing other techniques[261,262], these metallic pillars are sub-100 nm in diameter and can be processed in a single-step growth process that can be integrated in devices for a large range of applications. Currently, most of the metallic pillars in VANs are single phase metal with one functionality, e.g., plasmonic[144,205,260] or ferromagnetic[123,138,143,263], and very limited demonstration of complex metallic nanopillars[258].

A well coupled magnetic-plasmonic material framework is needed to fabricate stronger magneto-optical coupling. In this work, a unique composite metallic nanopillar structure coupling a plasmonic metal (e.g., Au) and a ferromagnetic metal (e.g., Fe) is proposed in a La_{0.5}Sr_{0.5}FeO₃ (LSFO) matrix, forming the complex three-phase metal-oxide VAN, i.e., Au-Fe-La_{0.5}Sr_{0.5}FeO₃ (Fe-Au-LSFO), as illustrated in Fig. 1. The reason that Au and Fe are selected as the metallic pillars is due to their plasmonic and ferromagnetic properties, respectively, and their immiscible nature following the Hume-Rothery rules accordingly[264]. LSFO was chosen as the oxide matrix since Fe-LSFO VANs have been successfully grown via decomposition[136] or with additional

Fe inclusions[204], effectively producing strong ferromagnetic properties. Because of the immiscible nature of Au and Fe, they will likely form two-phase pillars instead of alloyed pillars. By tuning the deposition parameters, such as deposition frequency, the morphology of the 3-phase VAN can be effectively tuned. The morphology tuning alters the magnetic, magneto-optical coupling and optical anisotropy which is used to evaluate the property coupling and added functionalities in using the complex 3-phase VAN designs.

7.3 Experimental

LSFO target was prepared via conventional sintering method with a 1:1 molar ratio of lanthanum and strontium into a pellet target. The films were then grown via pulsed laser deposition (PLD) system (KrF excimer laser) (Lambad Physik, $\lambda = 248$ nm) with a pure Au strip attached to the surface of the target, onto a single crystalline SrTiO_3 (STO) (001) substrate. Varying deposition frequencies of 2 Hz, 5 Hz, and 10 Hz were used to vary the nanostructure of the overall system.

The nanostructure of the films was analyzed using various analytical tools. X-ray diffraction (XRD), transmission electron microscopy (TEM) and scanning transmission electron microscopy (STEM) and energy dispersive x-ray spectra (EDS) elemental mapping were performed on all samples (FEI Talos-200X).

The magnetic behavior of the three-phase film was measured utilizing a magnetic property measuring system (MPMS 3, Quantum Design) for both parallel (in-plane) and perpendicular (out-of-plane) directions relative to the film surface.

The dielectric behavior of all the samples grown at different frequencies were measured by using a spectroscopic ellipsometer (JA Woollam RC2) by fitting an anisotropic model using general oscillators to fit the ellipsometer parameters ψ and Δ . The in-plane and out-of-plane permittivity was modeled using two Lorentz oscillators and a Drude-Lorentz model to enforce the Kramers-Kronig consistency, respectively.

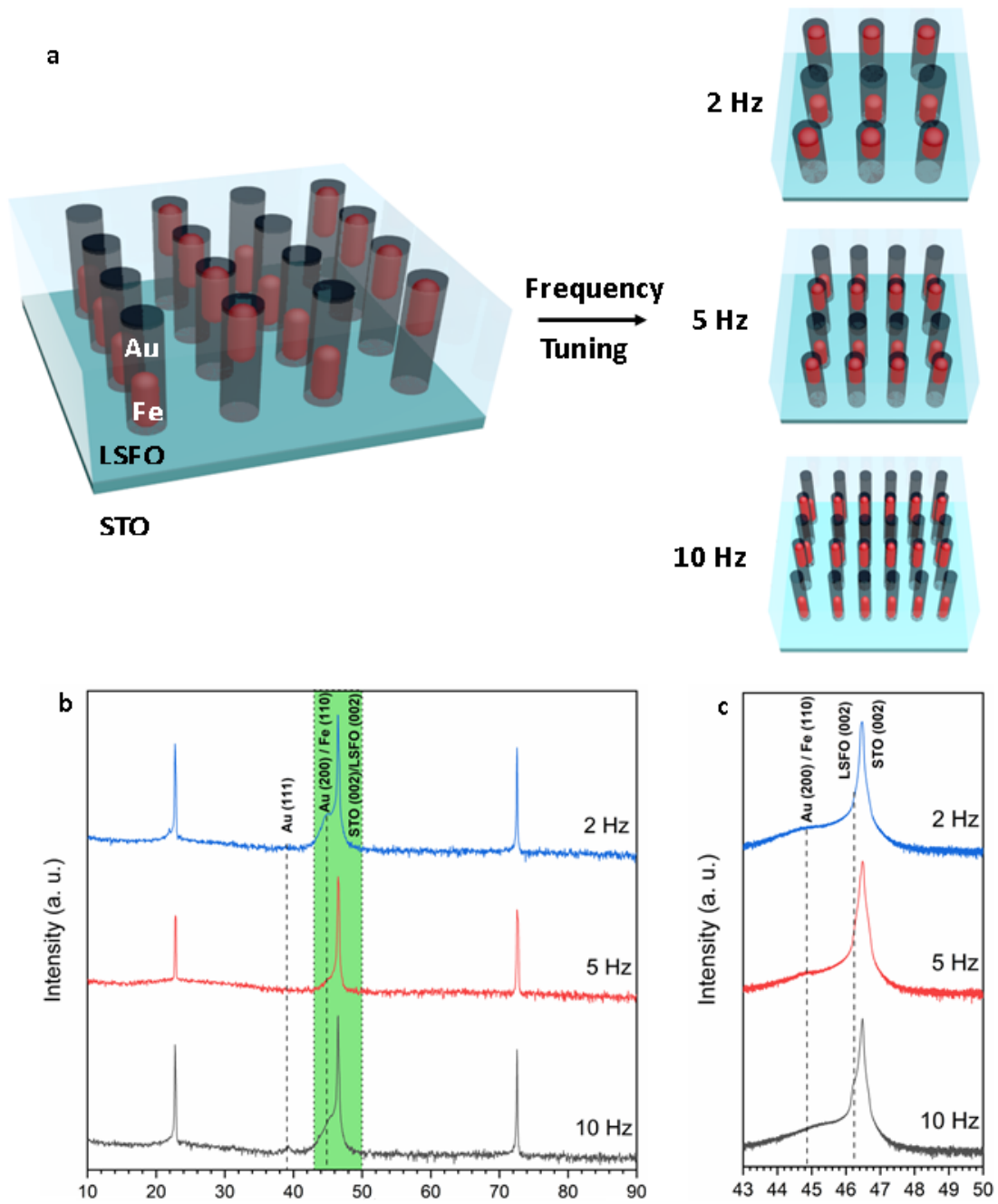


Figure 7.1a) Schematic demonstrating the growth of the Au-Fe-LSFO system. b) Typical θ - 2θ XRD scan of the different films deposited at different frequencies. c) A finer θ - 2θ XRD scan of the film between the 2θ values of 43 and 50°

7.4 Discussion

The phase composition and orientation of the Au-Fe-LSFO films deposited at different laser frequencies (2 Hz, 5 Hz, and 10 Hz) was first analyzed via typical θ - 2θ XRD scans of the films. The XRD data in Fig. 1b, shows the expected LSFO (002) peak with Au (111) peaks at a 2θ value of 39.11° and Au (200) and Fe (110) peaks located around at 2θ values of 44.97° , 45.16° , and 45.54° for the samples deposited at 2, 5, and 10 Hz, respectively. The existence of the Fe peaks indicates that the LSFO successfully decomposed through the reaction $2\text{La}_{0.5}\text{Sr}_{0.5}\text{FeO}_3 \rightarrow \text{LaSrFeO}_4 + \text{Fe} + \text{O}_2$ as previously reported[136]. Also, the Au peaks indicates that the Au was successfully deposited as a separate phase. As the deposition frequency increases from 2 to 5 to 10 Hz, the compressive strain based on the Fe (110) peak position increases to -0.66%, -1.09%, and -1.94%, respectively when compared to the bulk value at 44.673° (PDF # 06-0696). This strain variation can be attributed to the varying nucleation and growth time. As the frequency decreases, the Fe and Au atoms have a longer time to diffuse, creating metallic nanostructures with more relaxed strain states. Increasing frequencies result in the Fe and Au atoms have less time to diffuse creating more strained nanostructures.

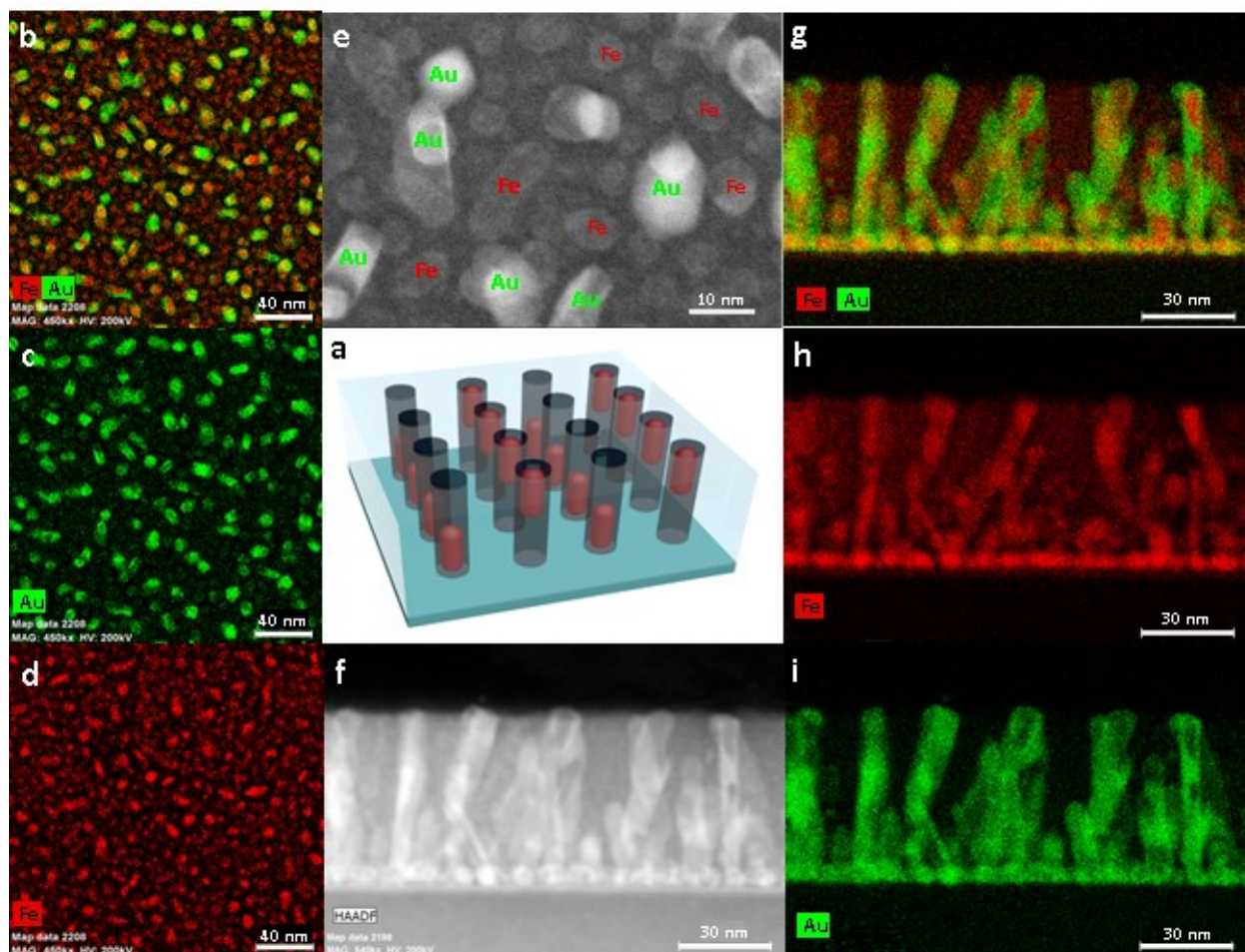


Figure 7.2a) Schematic demonstrating the Au-Fe-LSFO film grown on STO. b-d) Plan view EDX mappings of the 5 Hz film with b) Fe and Au, c) Au, and d) Fe mappings shown. e, f) HRSTEM image of the 5 Hz Au-Fe-LSFO film with e) being plan view and f) being cross-sectional. g-i) Plan view EDX mappings of the 5 Hz film with g) Fe and Au, h) Fe, and i) Au mappings shown

In addition to the strain state variation, it is also important to verify whether the Au and Fe have formed the proposed two phases or an alloyed structure. Usually, Fe and Au are immiscible under equilibrium conditions following the Hume-Rothery rules. Since PLD process introduces high kinetic energy and nonequilibrium conditions that may aid the formation of an alloyed structures, a careful TEM analysis was performed to reveal the phase distribution of the 3-phase VANs. TEM/STEM was instrumental in determining both the morphology of the nanostructure and phase separation of Au and Fe via plan-view TEM images of the 5 Hz Au-Fe-LSFO shown in Fig. 2b-e. The growth of the two metal phases led to two distinct groups of structures. One type of nanostructures has a larger diameter of around 15 nm with a lower density and lighter contrast,

while the other type has a smaller diameter of around 7 nm with a higher density and darker contrast. Additionally, the larger nanostructures are more faceted with a more polygonal shape, while the smaller nanostructures have a smooth, round shape. An EDS mapping was performed to specify the composition of the two nanostructures. The EDS reveals that the Au (green) are the larger nanostructures while the Fe (red) are the smaller nanostructures. From these images, it is possible to see discrete groups of both the Au and Fe, suggesting that the two metallic phases have formed as two phases in a unique Au encapsulated Fe structure.

To better understand the different nanostructures, additional cross sectional TEM images were taken of the 5 Hz Au-Fe-LSFO film. From the cross-sectional images in Fig 2f-i, it is possible to see two distinct Au-Fe morphologies in the system with the EDX mappings being displayed: 1) isotropic, metallic nanoparticles aggregated near the substrate and 2) anisotropic, column growth throughout the entirety of the film with selected columns having a slight tilt along the length of the column. The isotropic growth is most likely a result of the initial nucleation stages of the growth. In the initial stages, the Fe and Au have much higher surface energies than the LSFO, resulting in the metallic island growth. As the growth continues past the initial stage, the Fe nucleates along with the Au deposition, aggregating together due to their similar surface energy compared to the oxide matrix. This causes them to find other metal adatoms, forming a unique Au encapsulated Fe nanopillars. The tilting of the nanopillars could be related to the exposing of the lower surface energy of Au(111) planes while maintaining the crystalline orientation of the nanopillars.

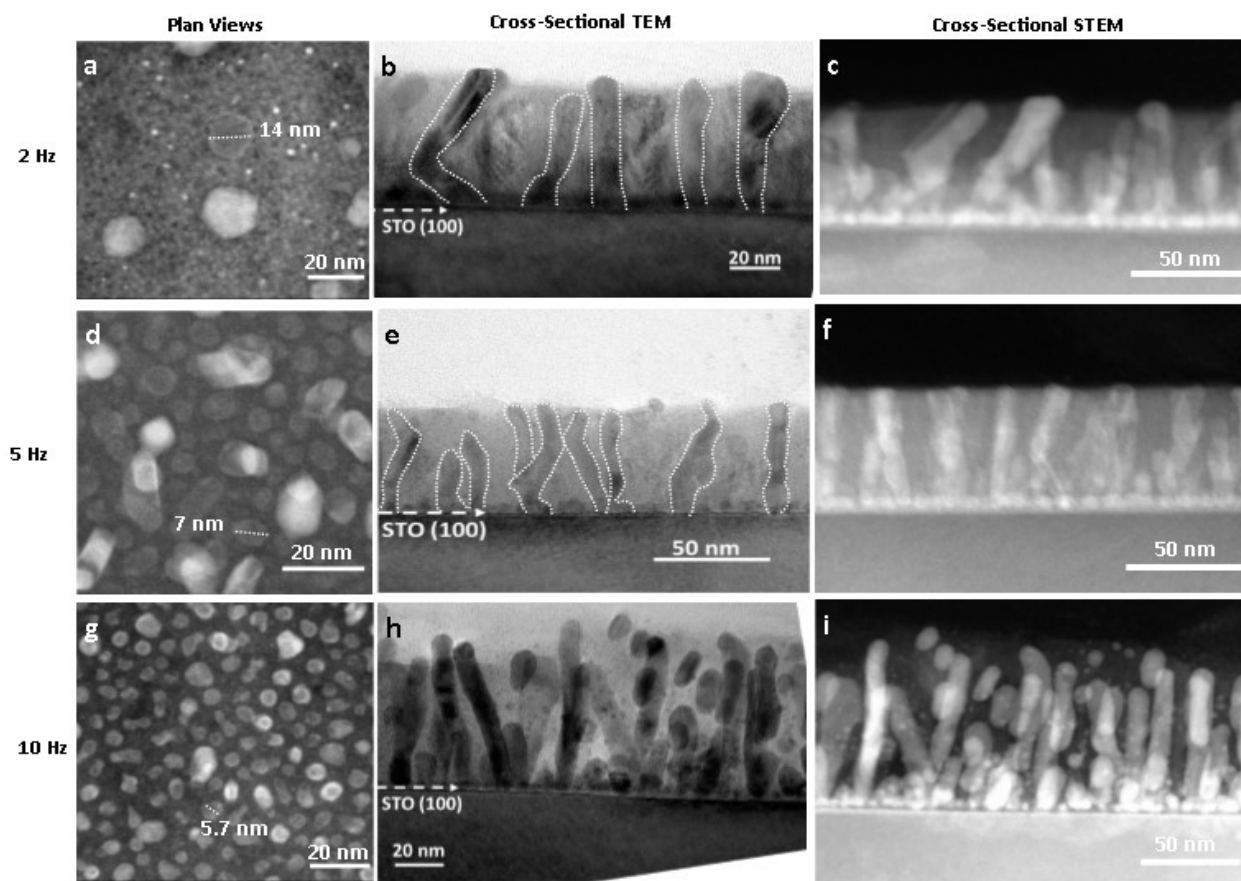


Figure 7.3a, d, g) Plan-view TEM images of the different frequencies to demonstrate how the Fe pillars vary. Cross sectional b, e, h) TEM images and c, f, i) STEM images to better observe how the pillar structure vary with frequency.

To investigate further how the Au and the Fe nucleate and to demonstrate the tunability of the nanostructures, the deposition frequency was varied from 2, 5, and 10 Hz. TEM analysis was performed on the different samples using both the cross-section and plan-view. From the plan-view images in Fig. 3, it is possible to see a trend in the sizes of the Fe nanostructures. As the frequency increases from 2 to 10 Hz, the Fe regions decrease in diameter from 14 nm to 7 nm to 5.7 nm, while the Au regions have a similar diameter of around 15 nm for the 2 and the 5 Hz sample, while in the 10 Hz sample, there are Au regions with a diameter of around 15 nm and other regions with a diameter of around 8 nm. The difference in the nucleation of Fe and Au comes from the fact that the Au tends to encapsulate some of the Fe pillars with some Fe pillars growing as single-phase ones. The single-phase Fe pillars are influenced by frequency which causes the narrowing of the diameter. The Au adatoms encapsulate the Fe pillars forming similar

nanostructure sizes regardless of frequency to some extent (e.g., 2 and 5 Hz), but for the 10 Hz, the diameter reduces. Additionally, there is an obvious shape variation as a function of frequency. At the lower frequency (e.g., 2 Hz), the Au regions are more faceted with sharp edges and corners. As the frequency increases to 5 Hz, the shape elongates along one direction with the edges reduced, but there are still several visible edges in Au. At 10 Hz, the Au regions lose all their edges, forming a round shape similar to the Fe nanostructures. This suggests that lower frequency and longer diffusion time lead to more faceted Au nanostructures while high frequency leads to round nanostructures.

Cross-sectional TEM images were taken to further reveal the morphology tuning. At 2 Hz, both the Au and the Fe form pillars with a discrete shape and a large size, but with selected pillars having either a 30° tilt or a vertical orientation. While for the 5 Hz growth, it is clear that the pillars are narrowed and grew in a more ordered and upright fashion. Lastly, for the 10 Hz sample, there seems to be two distinct growth morphologies, one being straight nanopillars, and the other being elongated nanoparticles (nano-pill-like) within the matrix. Additionally, just as the morphology and the diameter of the nanostructures varies with frequency, the density of the metallic nanostructures also varies, i.e., the density of the pillars increases as the deposition frequency increases. The specific nanostructure variations seen between the different frequencies are likely caused by the nucleation and diffusion process. Au tends to grow around Fe; as the Fe adatoms have less time to nucleate due to higher frequencies, the Fe adatoms will create smaller nanostructures with the Au nucleating around these Fe structures. Furthermore, the decreased nucleation time will cause a portion of the Fe adatoms to not have sufficient time to coalesce with the existing Fe nanostructures. The limited time results in separated Fe nanostructure development, leading to the formation of the nano-pill-like structures seen in the 10 Hz samples. For the 2 Hz and the 5 Hz samples, the decreased frequencies lead to increased nucleation time, resulting in larger pillars in the 5 Hz and the largest seen in the 2 Hz sample. Au also facilitated the growth of the pillars as evidenced from a comparison between pure Fe-LSFO and Au-Fe-LSFO films grown at similar growth conditions, shown in Fig. 8. From Fig. 8, the Fe regions grown in the two-phase Fe-LSFO VANs tends to grow in the nano-pill structures, yet in the 3-phase Au-Fe-LSFO VAN, nanopillars occur. This can be explained by the Au adatoms growing around the Fe regions. As the Au regions enclose the Fe regions, it makes it easier for other Au and Fe adatoms to grow on the more energetically favorable metal surfaces, resulting in the pillar growth.

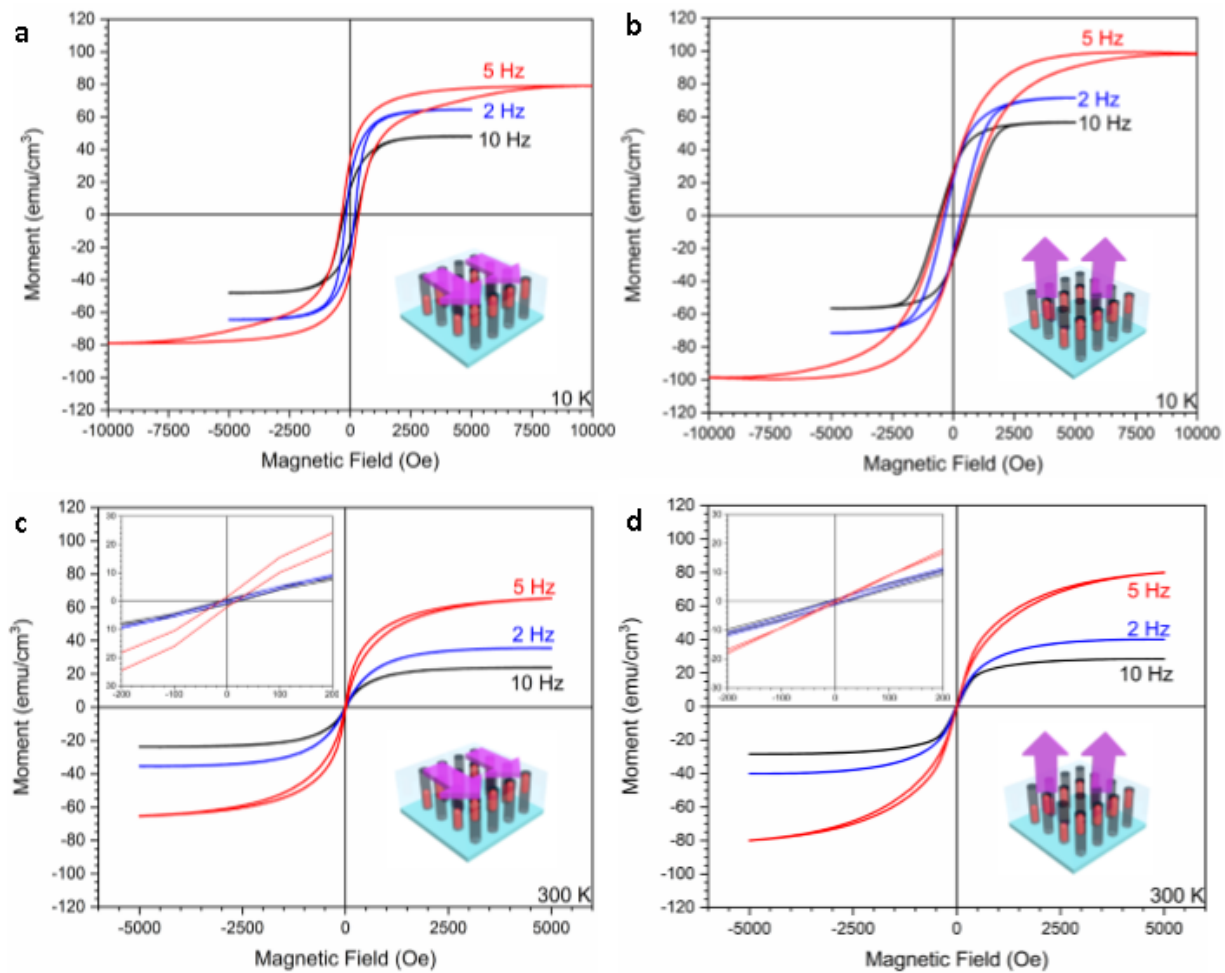


Figure 7.4a, b) Low and c, d) room temperature hysteresis loops of the Fe-BTO films grown at different frequencies with magnified inserts for the room temperature loops.

Next, to determine how the ferromagnetic behavior varies with the different nanostructures, measurements were taken from the different samples as shown in Fig. 4. At 10 K, the 2 Hz, 5 Hz, and 10 Hz have an in-plane saturation of 64 emu/cm³, 80 emu/cm³, and 48 emu/cm³ and out-of-plane saturation of 72 emu/cm³, 98 emu/cm³, and 57 emu/cm³, respectively, with an in-plane coercivity of 180 Oe, 350 Oe, and 270 Oe, and out-of-plane coercivity of 330 Oe, 460 Oe, and 576 Oe, respectively. At room temperature, the 2 Hz, 5 Hz, and 10 Hz have an in-plane saturation of 35 emu/cm³, 65 emu/cm³, and 24 emu/cm³ and out-of-plane saturation of 40 emu/cm³, 80 emu/cm³, and 28 emu/cm³, respectively, with an in-plane coercivity of 10 Oe, 15 Oe, and 18 Oe, and out-of-plane coercivity of 12 Oe, 5 Oe, and 15 Oe, respectively. Interestingly, even though the nanostructure of the pillars is highly anisotropic, the magnetic behavior displays a minor difference between the out-of-plane and in-plane, with the out-of-plane magnetization having slightly larger coercivity and saturation. This disparity arises due to the Fe regions having a more spherical, pill-like structure with the rest of the pillars consisting of Au metal. Since Au is non-magnetic, the magnetization will primary be caused by the Fe nanostructures. Furthermore, the hysteresis loops reveal that the 5 Hz sample has both the highest coercivity and the magnetic saturation in the low temperature region followed by the 2 Hz and the 10 Hz films. While for the room temperature measurements, the 5 Hz sample has the largest saturation, and all the samples have similar coercivity values. The reason that the 5 Hz film has the strongest ferromagnetic properties is because it has the most upright and uniform pillars. These pillars will require a larger applied magnetic field to align all the pillars in the same direction and will create a stronger net magnetic field. While for the 2 Hz film, as mentioned before, there is a slanted growth that takes place from the Au growths that shorten the Fe regions, causing the magnetic properties to decrease in both the out-of-plane and in-plane regions. The 10 Hz film exhibits the smallest ferromagnetic properties due to the Fe regions being the smallest and having discrete structures. These smaller regions will cause the magnetic direction to be easily turned, causing the 10 Hz film to have the weakest ferromagnetic properties.

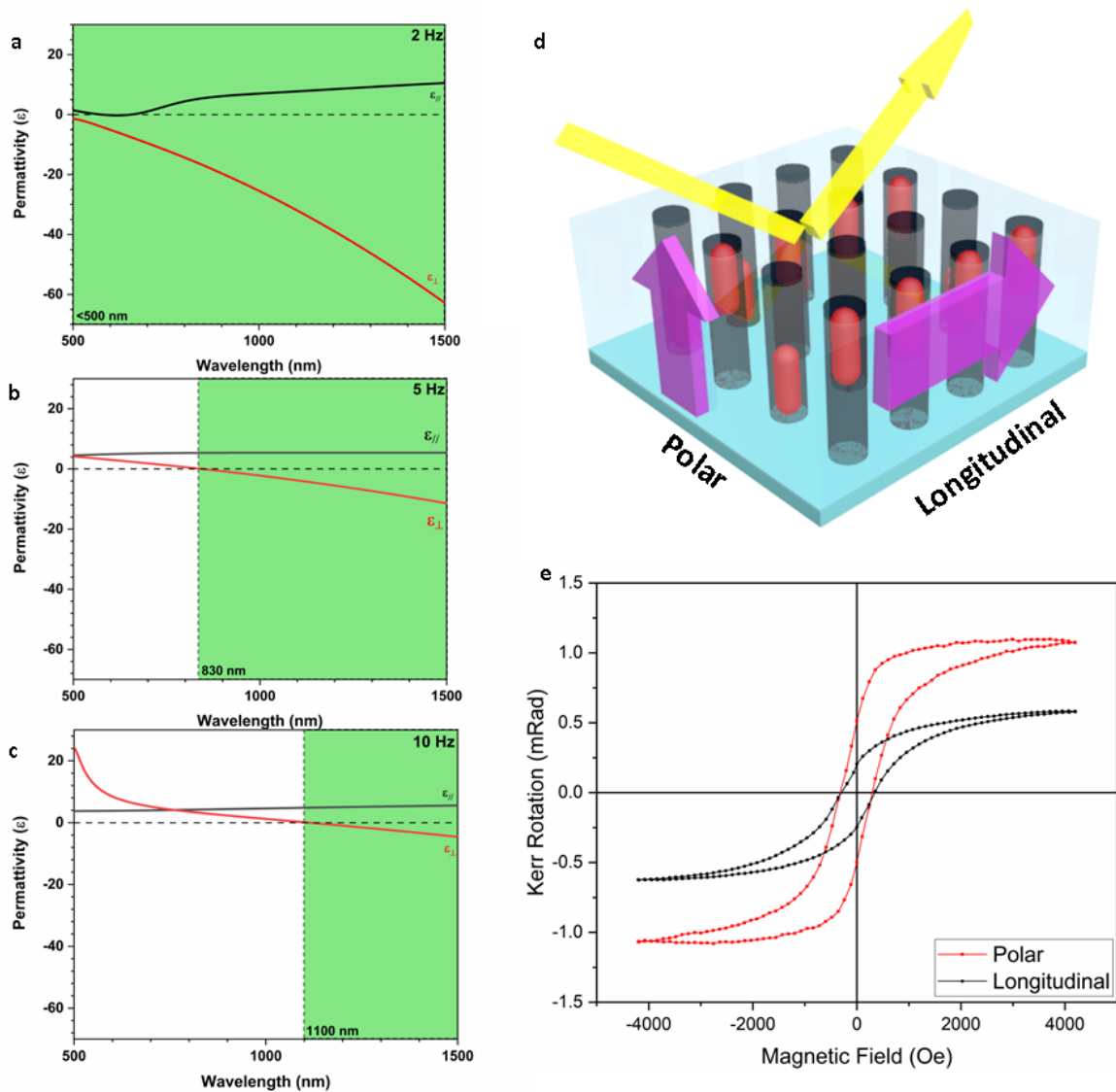


Figure 7.5a, b, c) Dielectric constants of the 2, 5, and 10 Hz sample modeled using data from the ellipsometer with the blue highlighting the hyperbolic region. d) Schematic demonstrating the polar and longitudinal directions of the MOKE measurements where the yellow is the light and the purple is the applied magnetic field direction. e) The MOKE readings for the polar and longitudinal directions for the 5 Hz measurement.

To evaluate the overall optical properties, the reflectivity data and optical transmittance data were collected and analyzed. The data in Fig 5a-c shows a clear anisotropy based on the out-of-plane and in-plane dielectric permittivity with the out-of-plane dielectric permittivity for all the samples being negative at certain wavelengths, indicating a hyperbolic response. Interestingly, the hyperbolic transition point shifts from slightly below 500 nm at 2 Hz, to 830 nm at 5 Hz, and 1100

nm at 10 Hz, with the out-of-plane dielectric permittivity decreasing with the increasing deposition frequency. This can be explained by the variation of nanostructures for each film. For the 2 Hz sample, the metallic pillars are the most continuous and the largest, and as the frequency increases, the continuity and the size of the pillars decreases, causing the trends seen in the out-of-plane dielectric permittivity. For the in-plane dielectric constant, the positive values are due to the metal regions being embedded within a ceramic matrix, causing a positive permittivity as seen in conventional ceramics. Interestingly, in Fig. 8a, in the in-plane 2 Hz sample, it is possible to see a plasmonic absorption response around the 610 nm wavelength, where there is a local minimum in the transmission curve. Since the 2 Hz has more ordered pillars, Au has grown in a more ordered structure, resulting in an enhanced plasmonic response. This indicates that, by tuning the growth parameters, it would be possible to strengthen the plasmonic response, the ferromagnetic response, and the hyperbolic transition point, which will be useful for various applications and devices.

To evaluate the magneto-optic coupling of the Au and the Fe nanostructures, MOKE data was taken at room temperature for the 5 Hz sample. From the data, it is possible to see how the induced magnetic responses varies as the light imposes on the sample in the polar and longitudinal directions (Fig 5d). Compared to the data shown in Fig 4, the MOKE data in Fig 5e, shows a large degree of anisotropy that exists between the in-plane (longitudinal) and out-of-plane (transverse) directions. The fact that the anisotropy in MOKE is much larger than that of the MPMS data indicates that the Fe was not the sole contributor to the Kerr rotation. Because of the differences, it can conclude that the Au played an additional role in directing the light through the film. As opposed to the spherical shape of the Fe regions, the Au encapsulated Fe nanostructures had a pillar geometry resulting in the anisotropy seen in the MOKE data. This indicates that the Au in conjunction with the Fe played a role in the magneto-optic behavior indicating that magneto-optical coupling between Au and Fe did occur. This magneto-optical coupling arises from the unique Au encapsulated Fe nanostructure in this film. For this result to be achieved, it was crucial for minimizing intermixing to avoid detrimental effect on both the optical and magnetic properties. To this end, Fe and Au are ideal candidates due to their immiscibility and strong physical properties. This immiscibility minimizes the Fe and Au intermixing during the nucleation process and instead forms the Au shell around the Fe to achieve the effective magneto-optical coupling. Additionally, by adding Au to the existing Fe-LSFO system, the Au encapsulated Fe nanostructures tend to grow into pillar form. These pillars result in highly anisotropic optical properties with hyperbolic optical

properties and a high degree of magneto-optical coupling. Further studies could consider other systems that Au can be added to: Fe-BaTiO₃[263], Co-BaZrO₃[123], and Ni-BaZr_{0.8}Y_{0.2}O₃[138]. Additionally, the added metal can be varied to other plasmonic metals such as Ag and Cu. This complex three-phase oxide-metal VAN utilizes immiscible metals to create a unique design for engineering complex functionalities and coupled functionalities for various optical and electronic device applications, especially pertaining to the field of spintronics, where recent work has shown the potential of magneto-optic enhancements to spintronic devices[74].

7.5 Conclusion

This study demonstrates a successful growth of a complex three-phase nanocomposite Au-Fe-LSFO thin film and potential in achieving tunable physical properties. This novel three-phase nanocomposite material combines the strong ferromagnetic properties of Fe with the strong plasmonic response of Au, creating a unique system exhibiting strong magneto-optical properties. Additionally, via tuning the deposition frequency, it is possible to tune the nanostructures of the film, and subsequently the magnetic and optical properties for use in different applications. This study demonstrates a method to include a third phase, another metal, in the oxide-metal VAN design to provide additional functionality beyond the conventional two-phase VAN systems offer. The approach opens a new and exciting avenue for effective magneto-optical coupling towards future optical switches, sensors, and spintronic devices.

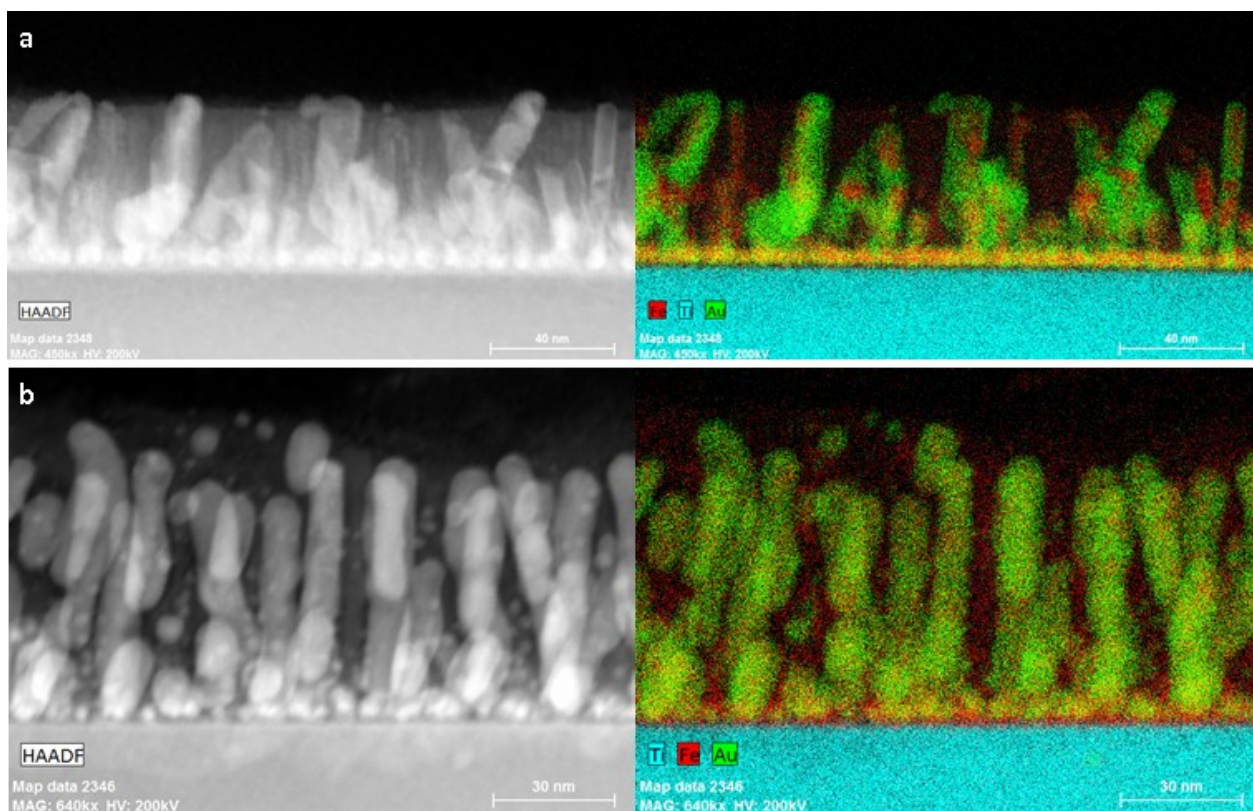


Figure 7.6 STEM and EDX images of Au-Fe-LSFO samples grown at a) 2 Hz and b) 10 Hz.

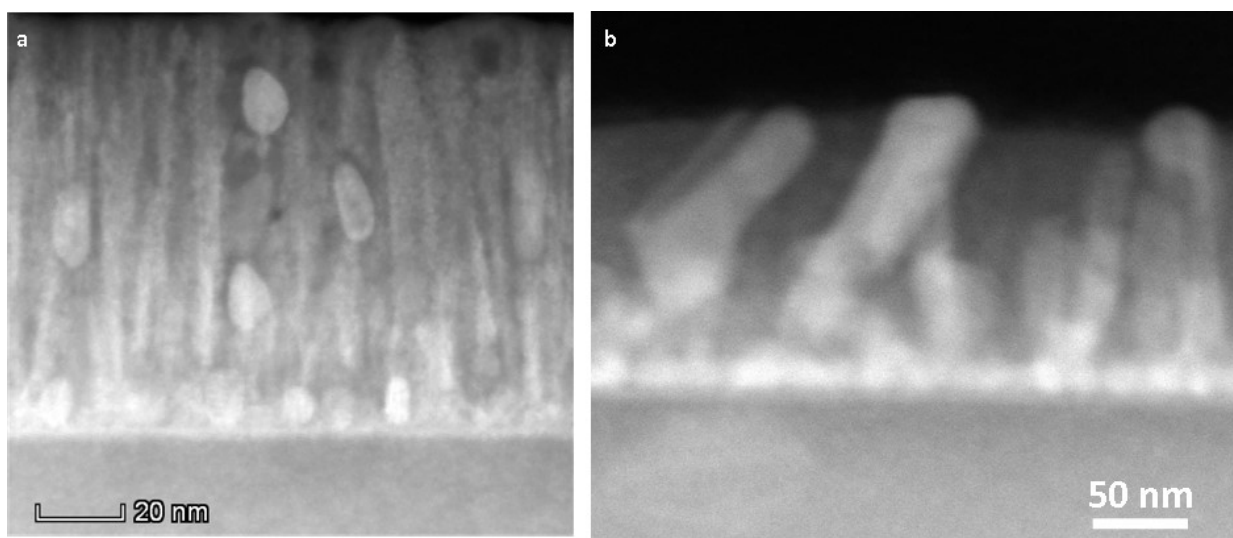


Figure 7.7 STEM images of a) Fe-LSFO and b) Au-Fe-LSFO samples grown at 2 Hz at STO.

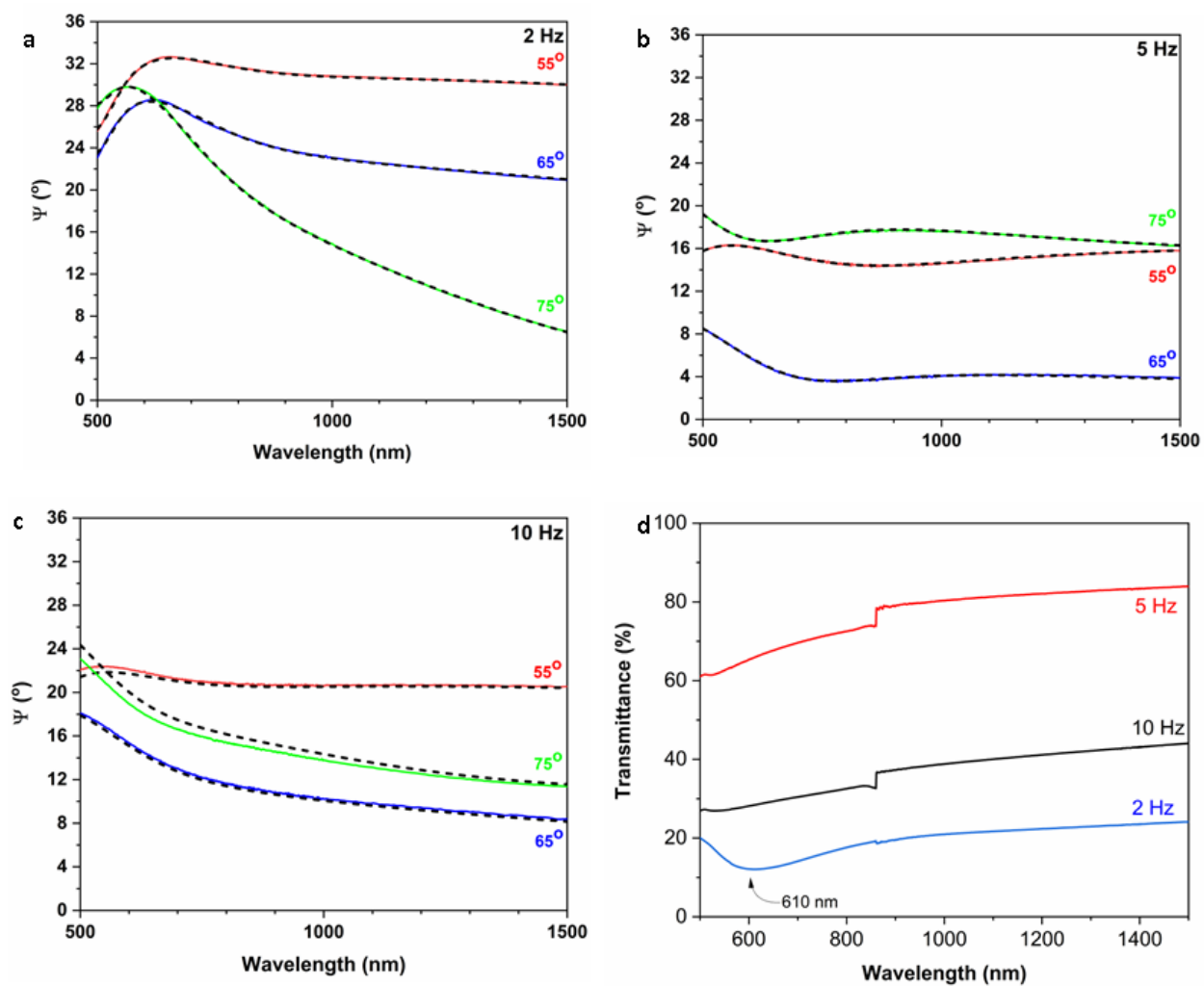


Figure 7.8 a, b, c) The measured reflectance data of the three different frequencies. d) The transmission data for the samples used to fit the model.

8. PRESENT AND FUTURE WORK

In this dissertation, the tuning of metal-oxide based VANs has been demonstrated. These VAN shows strong promise for anisotropic applications due to their strong, highly anisotropic, room temperature, physical properties. By tuning different growth conditions, such as laser energy, frequency, or thickness, the tuning of the coercivity and the anisotropy of the VAN is possible. Not only that, preliminary results for integration into a device that demonstrated magnetoresistance switching have been shown.

First, a technique was demonstrated that was able to tune the Fe nanostructures within Fe-LSFO film. In this film, by adjusting the laser energy, the nanostructure of the film was able to be tuned, and subsequently, their ferromagnetic properties. It was found that the strongest ferromagnetic properties existed at a laser energy of around 300 mJ. Second, to demonstrate the potential tune the anisotropy of the VAN, Co-BZO films of different thicknesses was grown. From the different thicknesses of the Co-BZO films, it was able to demonstrate a tuning of the coercivity of in-plane and out-of-plane properties. Additionally, the Co-BZO was integrated into a multilayer stack that allowed for a magnetoresistance change. This was a preliminary demonstration of a VAN device and opens new avenues for future work. New work has also been done on designing and growing a new system with the 3d transition metal, Fe, with a ferroelectric ceramic, BTO. This nanocomposite Fe-BTO metallic VAN has been successfully demonstrated. By changing the frequency of the laser, the diameter and structure of the Fe pillars within the Fe-BTO system has been tuned, which also tunes the room temperature ferromagnetic properties and dielectric constant of the Fe-BTO VAN. Furthermore, demonstrations were performed that showed successful coupling between the ferroelectric and ferromagnetic phases at room temperature that further highlights the multiferroic applications.

Finally, the design and successful growth of two metals within an oxide matrix has been demonstrated successfully with Au being introduced into the Fe-LSFO system. Furthermore, it has been demonstrated that by tuning the deposition conditions, mainly the deposition frequency, the metal nanostructures are able to be altered. This reveals a potential mechanism for tuning the physical properties, mainly the plasmonic response of the Au-Fe-LSFO system. Additionally, this work shows that the magnetic and plasmonic responses of the Fe and Au, respectively, are

coupled and this work may present a future framework for novel growth of three-phased VAN films.

While different VAN systems have been demonstrated, future work needs to be done on both controlling the growth of the VAN system and studying the underlying nucleation mechanisms. In order to successfully integrate the VAN into devices, it is essential to be able to demonstrate controlled growth and placement of the metal nanostructures. By tuning this bottom-up approach, it will become feasible to integrate this into current devices and integrated circuits. To achieve this goal, better understanding of the nucleation and growth process of the metal-oxide VAN must be achieved. By fully understanding the nucleation, it becomes possible to both modify the nanostructures and subsequently, tune their properties, and will lead to insights on how to control the long-range ordering of the metal-oxide VAN system, leading to the realization of the immense potential VAN can have on modern day devices and applications.

REFERENCES

- [1] S.S.P. Parkin, K.P. Roche, M.G. Samant, P.M. Rice, R.B. Beyers, R.E. Scheuerlein, E.J. O’Sullivan, S.L. Brown, J. Bucchigano, D.W. Abraham, Y. Lu, M. Rooks, P.L. Trouilloud, R. a Wanner, W.J. Gallagher, Exchange-biased magnetic tunnel junctions and application to nonvolatile magnetic random access memory (invited), *J. Appl. Phys.* 85 (1999) 5828–5833. <https://doi.org/10.1063/1.369932>.
- [2] M. Mannini, F. Pineider, P. Sainctavit, C. Danieli, E. Otero, C. Sciancalepore, A.M. Talarico, M.A. Arrio, A. Cornia, D. Gatteschi, R. Sessoli, Magnetic memory of a single-molecule quantum magnet wired to a gold surface, *Nat. Mater.* 8 (2009) 194–197. <https://doi.org/10.1038/nmat2374>.
- [3] D. Stoppels, Developments in soft magnetic power ferrites, *J. Magn. Magn. Mater.* 160 (1996) 323–328. [https://doi.org/10.1016/0304-8853\(96\)00216-8](https://doi.org/10.1016/0304-8853(96)00216-8).
- [4] D.P. Arnold, Review of microscale magnetic power generation, *IEEE Trans. Magn.* 43 (2007) 3940–3951. <https://doi.org/10.1109/TMAG.2007.906150>.
- [5] S. Parkin, X. Jiang, C. Kaiser, A. Panchula, K. Roche, M. Samant, Magnetically engineered spintronic sensors and memory, *Proc. IEEE.* 91 (2003) 661–679. <https://doi.org/10.1109/JPROC.2003.811807>.
- [6] L. López-Mir, C. Frontera, H. Aramberri, K. Bouzehouane, J. Cisneros-Fernández, B. Bozzo, L. Balcells, B. Martínez, Anisotropic sensor and memory device with a ferromagnetic tunnel barrier as the only magnetic element, *Sci. Rep.* 8 (2018) 1–10. <https://doi.org/10.1038/s41598-017-19129-5>.
- [7] W. Lowrie, Geomagnetism and paleomagnetism, in: *Fundam. Geophys.*, 2nd ed., Cambridge University Press, Cambridge, 2007: pp. 281–362. <https://doi.org/10.1017/CBO9780511807107.006>.
- [8] L.W. Martin, A.M. Rappe, Thin-film ferroelectric materials and their applications, *Nat. Rev. Mater.* 2 (2017) 16087. <https://doi.org/10.1038/natrevmats.2016.87>.
- [9] C.W. Nan, M.I. Bichurin, S. Dong, D. Viehland, G. Srinivasan, Multiferroic magnetoelectric composites: Historical perspective, status, and future directions, *J. Appl. Phys.* 103 (2008). <https://doi.org/10.1063/1.2836410>.
- [10] M.C. Ramírez-Camacho, C.F. Sánchez-Valdés, J.J. Gervacio-Arciniega, R. Font, C. Ostos, D. Bueno-Baques, M. Curiel, J.L. Sánchez-Llamazares, J.M. Siqueiros, O. Raymond-Herrera, Room temperature ferromagnetism and ferroelectricity in strained multiferroic BiFeO₃ thin films on La_{0.7}Sr_{0.3}MnO₃/SiO₂/Si substrates, *Acta Mater.* 128 (2017) 451–464. <https://doi.org/10.1016/j.actamat.2017.02.030>.

- [11] E.Y. Tsymbal, a. Gruverman, V. Garcia, M. Bibes, a. Barthélémy, Ferroelectric and multiferroic tunnel junctions, *MRS Bull.* 37 (2012) 138–143. <https://doi.org/10.1557/mrs.2011.358>.
- [12] M. Malaidurai, B. Santosh Kumar, R. Thangavel, Spin polarized carrier injection driven magneto-optical Kerr effect in Cr-doped ZnO nanorods, *Phys. Lett. Sect. A Gen. At. Solid State Phys.* 383 (2019) 2988–2992. <https://doi.org/10.1016/j.physleta.2019.06.031>.
- [13] M.S. Kushwaha, Magneto-optics of single Rashba spintronic quantum dots subjected to a perpendicular magnetic field: Fundamentals, *J. Appl. Phys.* 104 (2008) 83714. <https://doi.org/10.1063/1.3003086>.
- [14] P. Huo, S. Zhang, Y. Liang, Y. Lu, T. Xu, Hyperbolic Metamaterials and Metasurfaces: Fundamentals and Applications, *Adv. Opt. Mater.* 7 (2019) 1–25. <https://doi.org/10.1002/adom.201801616>.
- [15] J. Huang, M. Fan, H. Wang, L. Chen, C.-F. Tsai, L. Li, H. Wang, Enhanced superconducting properties of YBa₂Cu₃O₇-delta thin film with magnetic nanolayer additions, *Ceram. Int.* 42 (2016) 12202–12209. <https://doi.org/10.1016/j.ceramint.2016.04.161>.
- [16] A. Hajalilou, S. Amri Mazlan, H. Lavvafi, K. Shameli, Field Responsive Fluids as Smart Materials, 2016. <https://doi.org/10.1007/978-981-10-2495-5>.
- [17] J. Ilic, Wood: Electrical Properties, in: K.H.J. Buschow, R.W. Cahn, M.C. Flemings, B. Ilschner, E.J. Kramer, S. Mahajan, P.B.T.-E. of M.S. and T. Veyssi re (Eds.), *Encycl. Mater. Sci. Technol.*, Elsevier, Oxford, 2001: pp. 9629–9633. <https://doi.org/10.1016/B0-08-043152-6/01744-7>.
- [18] B. O’Driscoll, E. Ferre, C. Magee, C. Stevenson, The Significance of Magnetic Fabric in Layered Mafic-Ultramafic Intrusions, in: *Layer. Intrusions*, 2015: pp. 295–329. https://doi.org/10.1007/978-94-017-9652-1_7.
- [19] R. Jackson, John Tyndall and the Early History of Diamagnetism, *Ann. Sci.* 72 (2015) 435–489. <https://doi.org/10.1080/00033790.2014.929743>.
- [20] R. Bo a, Types of Magnetic Materials, in: R.B.T.-C.M. in I.C. Bo a (Ed.), *Theor. Found. Mol. Magn.*, Elsevier, 1999: pp. 345–370. [https://doi.org/10.1016/S1873-0418\(99\)80008-6](https://doi.org/10.1016/S1873-0418(99)80008-6).
- [21] F.A. Buot, J.W. McClure, Theory of diamagnetism of bismuth, *Phys. Rev. B.* 6 (1972) 4525–4533. <https://doi.org/10.1103/PhysRevB.6.4525>.
- [22] V.I. VAIDYANATHAN, Influence of Chemical Golloidisation on the Anomalous Diamagnetism of Bismuth and Antimony, *Nature.* 125 (1930) 672–672. <https://doi.org/10.1038/125672c0>.
- [23] J. Mizia, G. G rski, Paramagnetism and Weiss Ferromagnetism, in: J. Mizia, G.B.T.-M. of I.O. in C. G rski (Eds.), *Model. Itiner. Ordering Cryst.*, Elsevier, Oxford, 2007: pp. 19–26. <https://doi.org/10.1016/B978-008044647-9/50003-2>.

- [24] S. Saini, R.B. Frankel, D.D. Stark, J.T. Ferrucci, Magnetism: A primer and review, *Am. J. Roentgenol.* 150 (1988) 735–743. <https://doi.org/10.2214/ajr.150.4.735>.
- [25] T. Neuberger, B. Schöpf, H. Hofmann, M. Hofmann, B. Von Rechenberg, Superparamagnetic nanoparticles for biomedical applications: Possibilities and limitations of a new drug delivery system, *J. Magn. Magn. Mater.* 293 (2005) 483–496. <https://doi.org/10.1016/j.jmmm.2005.01.064>.
- [26] I. Malaescu, C.N. Marin, Deviation from the superparamagnetic behaviour of fine-particle systems, *J. Magn. Magn. Mater.* 218 (2000) 91–96. [https://doi.org/10.1016/S0304-8853\(00\)00334-6](https://doi.org/10.1016/S0304-8853(00)00334-6).
- [27] B. Barbara, Louis Néel: His multifaceted seminal work in magnetism, *Comptes Rendus Phys.* 1 (2019) 1–19. <https://doi.org/10.1016/j.crhy.2019.07.003>.
- [28] P.K. Manna, S.M. Yusuf, M. Basu, T. Pal, The magnetic proximity effect in a ferrimagnetic Fe₃O₄ core/ferrimagnetic γ -Mn₂O₃ shell nanoparticle system, *J. Phys. Condens. Matter.* 23 (2011) 506004. <https://doi.org/10.1088/0953-8984/23/50/506004>.
- [29] A. Donges, S. Khmelevskyi, A. Deak, R.M. Abrudan, D. Schmitz, I. Radu, F. Radu, L. Szunyogh, U. Nowak, Magnetization compensation and spin reorientation transition in ferrimagnetic DyCo₅: Multiscale modeling and element-specific measurements, *Phys. Rev. B.* 96 (2017) 1–7. <https://doi.org/10.1103/PhysRevB.96.024412>.
- [30] C.D. Stanciu, A. V. Kimel, F. Hansteen, A. Tsukamoto, A. Itoh, A. Kirilyuk, T. Rasing, Ultrafast spin dynamics across compensation points in ferrimagnetic GdFeCo: The role of angular momentum compensation, *Phys. Rev. B - Condens. Matter Mater. Phys.* 73 (2006) 1–4. <https://doi.org/10.1103/PhysRevB.73.220402>.
- [31] J.C. Slater, The ferromagnetism of nickel, *Phys. Rev.* 49 (1936) 537–545. <https://doi.org/10.1103/PhysRev.49.537>.
- [32] R.F. Mould, Pierre curie, 1859-1906, *Curr. Oncol.* 14 (2007) 74–82. <https://doi.org/10.3747/co.2007.110>.
- [33] K. Inomata, Y. Saito, K. Nakajima, M. Sagoi, Double tunnel junctions for magnetic random access memory devices, *J. Appl. Phys.* 87 (2000) 6064–6066. <https://doi.org/10.1063/1.372613>.
- [34] D. Lin, P. Zhou, W.N. Fu, Z. Badics, Z.J. Cendes, A dynamic core loss model for soft ferromagnetic and power ferrite materials in transient finite element analysis, *IEEE Trans. Magn.* 40 (2004) 1318–1321. <https://doi.org/10.1109/TMAG.2004.825025>.
- [35] J. Åkerman, P. Brown, M. DeHerrera, M. Durlam, E. Fuchs, D. Gajewski, M. Griswold, J. Janesky, J.J. Nahas, S. Tehrani, Demonstrated reliability of 4-Mb MRAM, *IEEE Trans. Device Mater. Reliab.* 4 (2004) 428–434. <https://doi.org/10.1109/TDMR.2004.837608>.

- [36] W.H. Meiklejohn, C.P. Bean, New Magnetic Anisotropy, *Phys. Rev.* 102 (1956) 1413–1414. <https://doi.org/10.1103/PhysRev.102.1413>.
- [37] M. Kiwi, Exchange bias theory, *J. Magn. Magn. Mater.* 234 (2001) 584–595. [https://doi.org/10.1016/S0304-8853\(01\)00421-8](https://doi.org/10.1016/S0304-8853(01)00421-8).
- [38] R.L. Stamps, Mechanisms for exchange bias, *J. Phys. D. Appl. Phys.* 33 (2000). <https://doi.org/10.1088/0022-3727/33/23/201>.
- [39] P. Bruno, Tight-binding approach to the orbital magnetic moment and magnetocrystalline anisotropy of transition-metal monolayers, *Phys. Rev. B.* 39 (1989) 865–868. <https://doi.org/10.1103/PhysRevB.39.865>.
- [40] J. Friedel, P. Lenglart, G. Leman, Etude du couplage spin-orbite dans les metaux de transition. Application au platine, *J. Phys. Chem. Solids.* 25 (1964) 781–800. [https://doi.org/10.1016/0022-3697\(64\)90090-3](https://doi.org/10.1016/0022-3697(64)90090-3).
- [41] G.C. Fletcher, Density of states curve for the 3d electrons in nickel, *Proc. Phys. Soc. Sect. A.* 65 (1952) 192–202. <https://doi.org/10.1088/0370-1298/65/3/306>.
- [42] B.D. Cullity (Bernard Dennis), *Introduction to magnetic materials*, 2nd ed., Hoboken, New Jersey : IEEE/Wiley, 2015.
- [43] X. Fan, H. Zhou, J. Rao, X. Zhao, J. Zhao, F. Zhang, D. Xue, Magnetic field-dependent shape anisotropy in small patterned films studied using rotating magnetoresistance, *Sci. Rep.* 5 (2015) 1–9. <https://doi.org/10.1038/srep16139>.
- [44] J. Dubowik, Shape anisotropy of magnetic heterostructures, *Phys. Rev. B - Condens. Matter Mater. Phys.* 54 (1996) 1088–1091. <https://doi.org/10.1103/PhysRevB.54.1088>.
- [45] W. Thomson, XIX. On the electro-dynamic qualities of metals:—Effects of magnetization on the electric conductivity of nickel and of iron, *Proc. R. Soc. London.* 8 (1857) 546–550. <https://doi.org/10.1098/rspl.1856.0144>.
- [46] A. Vailionis, The effects of strain on crystal structure and properties during epitaxial growth of oxides, in: G. Koster, M. Huijben, G.B.T.-E.G. of C.M.O. Rijnders (Eds.), *Ep. Growth Complex Met. Oxides*, Elsevier, 2015: pp. 175–207. <https://doi.org/10.1016/B978-1-78242-245-7.00007-5>.
- [47] G.H. Jonker, J.H. Van Santen, Ferromagnetic compounds of manganese with perovskite structure, *Physica.* 16 (1950) 337–349. [https://doi.org/10.1016/0031-8914\(50\)90033-4](https://doi.org/10.1016/0031-8914(50)90033-4).
- [48] Y.A. Izyumov, Y.N. Skryabin, Double exchange model and the unique properties of the manganites, *Uspekhi Fiz. Nauk.* 171 (2001) 147–148. <https://doi.org/10.1070/PU2001v044n02ABEH000840>.

- [49] A.J. Millis, P.B. Littlewood, B.I. Shraiman, Double exchange alone does not explain the resistivity of $\text{La}_{1-x}\text{Sr}_x\text{MnO}_3$, *Phys. Rev. Lett.* 74 (1995) 5144–5147. <https://doi.org/10.1103/PhysRevLett.74.5144>.
- [50] J.L. Alonso, L.A. Fernández, F. Guinea, V. Laliena, A. Martín-Mayor, Variational mean-field approach to the double-exchange model, *Phys. Rev. B - Condens. Matter Mater. Phys.* 63 (2001) 1–12. <https://doi.org/10.1103/PhysRevB.63.054411>.
- [51] D.M. Edwards, A.C.M. Green, K. Kubo, Electronic structure and resistivity of the double exchange model, *J. Phys. Condens. Matter.* 11 (1999) 2791–2808. <https://doi.org/10.1088/0953-8984/11/13/014>.
- [52] G. Binasch, P. Grünberg, F. Saurenbach, W. Zinn, Enhanced magnetoresistance in layered magnetic structures with antiferromagnetic interlayer exchange, *Phys. Rev. B.* 39 (1989) 4828–4830. <https://doi.org/10.1103/PhysRevB.39.4828>.
- [53] M.N. Baibich, J.M. Broto, A. Fert, F.N. Van Dau, F. Petroff, P. Eitenne, G. Creuzet, A. Friederich, J. Chazelas, Giant magnetoresistance of (001)Fe/(001)Cr magnetic superlattices, *Phys. Rev. Lett.* 61 (1988) 2472–2475. <https://doi.org/10.1103/PhysRevLett.61.2472>.
- [54] M. Julliere, Tunneling between ferromagnetic films, *Phys. Lett. A.* 54 (1975) 225–226. [https://doi.org/10.1016/0375-9601\(75\)90174-7](https://doi.org/10.1016/0375-9601(75)90174-7).
- [55] T. Miyazaki, S. Kumagai, T. Yaoi, Spin tunneling in Ni–Fe/Al₂O₃/Co junction devices (invited), *J. Appl. Phys.* 81 (1997) 3753–3757. <https://doi.org/10.1063/1.364957>.
- [56] S. Yadavalli, M.H. Yang, C.P. Flynn, Low-temperature growth of MgO by molecular-beam epitaxy, *Phys. Rev. B.* 41 (1990) 7961–7963. <https://doi.org/10.1103/PhysRevB.41.7961>.
- [57] H. Schmid, Some symmetry aspects of ferroics and single phase multiferroics *, *J. Phys. Condens. Matter.* 20 (2008) 434201. <https://doi.org/10.1088/0953-8984/20/43/434201>.
- [58] R. Blinc, The soft mode concept and the history of ferroelectricity, *Ferroelectrics.* 74 (1987) 301–303. <https://doi.org/10.1080/00150198708201310>.
- [59] M. Hoffmann, F.P.G. Fengler, M. Herzig, T. Mittmann, B. Max, U. Schroeder, R. Negrea, P. Lucian, S. Slesazek, T. Mikolajick, Unveiling the double-well energy landscape in a ferroelectric layer, *Nature.* 565 (2019) 464–467. <https://doi.org/10.1038/s41586-018-0854-z>.
- [60] V. Garcia, M. Bibes, Ferroelectric tunnel junctions for information storage and processing, *Nat. Commun.* 5 (2014). <https://doi.org/10.1038/ncomms5289>.
- [61] H. Kohlstedt, N.A. Pertsev, J. Rodríguez Contreras, R. Waser, Theoretical current-voltage characteristics of ferroelectric tunnel junctions, *Phys. Rev. B - Condens. Matter Mater. Phys.* 72 (2005) 1–10. <https://doi.org/10.1103/PhysRevB.72.125341>.

- [62] J. Mathon, A. Umerski, Theory of tunneling magnetoresistance of an epitaxial Fe/MgO/Fe(001) junction, *Phys. Rev. B - Condens. Matter Mater. Phys.* 63 (2001) 1–4. <https://doi.org/10.1103/PhysRevB.63.220403>.
- [63] W.H. Butler, X.-G. Zhang, T.C. Schulthess, J.M. MacLaren, Spin-dependent tunneling conductance of $\text{Fe}/\text{MgO}/\text{Fe}$ sandwiches, *Phys. Rev. B.* 63 (2001) 054416. <https://doi.org/10.1103/PhysRevB.63.054416>.
- [64] M. Bowen, V. Cros, F. Petroff, A. Fert, C. Martínez Boubeta, J.L. Costa-Krämer, J. V. Anguita, A. Cebollada, F. Briones, J.M. De Teresa, L. Morellón, M.R. Ibarra, F. Güell, F. Peiró, A. Cornet, Large magnetoresistance in Fe/MgO/FeCo(001) epitaxial tunnel junctions on GaAs(001), *Appl. Phys. Lett.* 79 (2001) 1655–1657. <https://doi.org/10.1063/1.1404125>.
- [65] S. Yuasa, T. Nagahama, A. Fukushima, Y. Suzuki, K. Ando, Giant room-temperature magnetoresistance in single-crystal Fe/MgO/Fe magnetic tunnel junctions, *Nat. Mater.* 3 (2004) 868–871. <https://doi.org/10.1038/nmat1257>.
- [66] S. Ikeda, K. Miura, H. Yamamoto, K. Mizunuma, H.D. Gan, M. Endo, S. Kanai, J. Hayakawa, F. Matsukura, H. Ohno, A perpendicular-anisotropy CoFeB–MgO magnetic tunnel junction, *Nat. Mater.* 9 (2010) 721–724. <https://doi.org/10.1038/nmat2804>.
- [67] C. Grezes, F. Ebrahimi, J.G. Alzate, X. Cai, J.A. Katine, J. Langer, B. Ocker, P. Khalili Amiri, K.L. Wang, Ultra-low switching energy and scaling in electric-field-controlled nanoscale magnetic tunnel junctions with high resistance-area product, *Appl. Phys. Lett.* 108 (2016) 012403. <https://doi.org/10.1063/1.4939446>.
- [68] Y. Huai, H. Gan, Z. Wang, P. Xu, X. Hao, B.K. Yen, R. Malmhall, N. Pakala, C. Wang, J. Zhang, Y. Zhou, D. Jung, K. Satoh, R. Wang, L. Xue, M. Pakala, High performance perpendicular magnetic tunnel junction with Co/Ir interfacial anisotropy for embedded and standalone STT-MRAM applications, *Appl. Phys. Lett.* 112 (2018) 092402. <https://doi.org/10.1063/1.5018874>.
- [69] K.C. Chun, H. Zhao, J.D. Harms, T.H. Kim, J.P. Wang, C.H. Kim, A scaling roadmap and performance evaluation of in-plane and perpendicular MTJ based STT-MRAMs for high-density cache memory, *IEEE J. Solid-State Circuits.* 48 (2013) 598–610. <https://doi.org/10.1109/JSSC.2012.2224256>.
- [70] H. Ohmori, T. Hatori, S. Nakagawa, Perpendicular magnetic tunnel junction with tunneling magnetoresistance ratio of 64% using MgO (100) barrier layer prepared at room temperature, *J. Appl. Phys.* 103 (2008) 98–101. <https://doi.org/10.1063/1.2840016>.
- [71] M. Gajek, M. Bibes, S. Fusil, K. Bouzehouane, J. Fontcuberta, A. Barthélémy, A. Fert, Tunnel junctions with multiferroic barriers., *Nat. Mater.* 6 (2007) 296–302. <https://doi.org/10.1038/nmat1860>.

- [72] Y. Liu, X. Zhang, Metamaterials: A new frontier of science and technology, *Chem. Soc. Rev.* 40 (2011) 2494–2507. <https://doi.org/10.1039/c0cs00184h>.
- [73] J. Wang, Y.K. Takahashi, K. ichi Uchida, Magneto-optical painting of heat current, *Nat. Commun.* 11 (2020) 1–7. <https://doi.org/10.1038/s41467-019-13799-7>.
- [74] A. Dutta, A. V. Kildishev, V.M. Shalaev, A. Boltasseva, E.E. Marinero, Surface-plasmon opto-magnetic field enhancement for all-optical magnetization switching, *Opt. Mater. Express.* 7 (2017) 4316. <https://doi.org/10.1364/ome.7.004316>.
- [75] R.A. Shelby, D.R. Smith, S. Schultz, Experimental verification of a negative index of refraction, *Science* (80-.). 292 (2001) 77–79. <https://doi.org/10.1126/science.1058847>.
- [76] V.G. Veselago, THE ELECTRODYNAMICS OF SUBSTANCES WITH SIMULTANEOUSLY NEGATIVE VALUES OF ϵ AND μ , *Sov. Phys. Uspekhi.* 10 (1968) 509–514. <https://doi.org/10.1070/pu1968v010n04abeh003699>.
- [77] J.B. Pendry, Negative refraction makes a perfect lens, *Phys. Rev. Lett.* 85 (2000) 3966–3969. <https://doi.org/10.1103/PhysRevLett.85.3966>.
- [78] P. Alitalo, S. Tretyakov, Electromagnetic cloaking with metamaterials, *Mater. Today.* 12 (2009) 22–29. [https://doi.org/10.1016/S1369-7021\(09\)70072-0](https://doi.org/10.1016/S1369-7021(09)70072-0).
- [79] Z.J. Wong, Y. Wang, K. O’Brien, J. Rho, X. Yin, S. Zhang, N. Fang, T.J. Yen, X. Zhang, Optical and acoustic metamaterials: Superlens, negative refractive index and invisibility cloak, *J. Opt. (United Kingdom).* 19 (2017). <https://doi.org/10.1088/2040-8986/aa7a1f>.
- [80] P. Yu, L. V. Besteiro, Y. Huang, J. Wu, L. Fu, H.H. Tan, C. Jagadish, G.P. Wiederrecht, A.O. Govorov, Z. Wang, Broadband Metamaterial Absorbers, *Adv. Opt. Mater.* 7 (2019) 1–32. <https://doi.org/10.1002/adom.201800995>.
- [81] G. Singh, R. Ni, A. Marwaha, A Review of Metamaterials and its Applications, *Int. J. Eng. Trends Technol.* 19 (2015) 305–310. <https://doi.org/10.14445/22315381/IJETT-V19P254>.
- [82] F. Xu, Y. Bai, L. Qiao, H. Zhao, J. Zhou, Realization of negative permittivity of Co₂Z hexagonal ferrite and left-handed property of ferrite composite material, *J. Phys. D. Appl. Phys.* 42 (2009). <https://doi.org/10.1088/0022-3727/42/2/025403>.
- [83] A. Poddubny, I. Iorsh, P. Belov, Y. Kivshar, Hyperbolic metamaterials, *Nat. Photonics.* 7 (2013) 958–967. <https://doi.org/10.1038/nphoton.2013.243>.
- [84] V.M. Agranovich, V.E. Kravtsov, Notes on crystal optics of superlattices, *Solid State Commun.* 55 (1985) 85–90. [https://doi.org/10.1016/0038-1098\(85\)91111-1](https://doi.org/10.1016/0038-1098(85)91111-1).
- [85] A.A. Orlov, P.M. Voroshilov, P.A. Belov, Y.S. Kivshar, Engineered optical nonlocality in nanostructured metamaterials, *Phys. Rev. B - Condens. Matter Mater. Phys.* 84 (2011) 1–4. <https://doi.org/10.1103/PhysRevB.84.045424>.

- [86] Z. Liu, H. Lee, Y. Xiong, C. Sun, X. Zhang, Far-field optical hyperlens magnifying sub-diffraction-limited objects, *Science* (80-.). 315 (2007) 1686. <https://doi.org/10.1126/science.1137368>.
- [87] H.N.S. Krishnamoorthy, Z. Jacob, E. Narimanov, I. Kretzschmar, V.M. Menon, Topological transitions in metamaterials, *Opt. InfoBase Conf. Pap.* (2012) 205–210. <https://doi.org/10.1364/qels.2012.qm2e.6>.
- [88] J. Kim, V.P. Drachev, Z. Jacob, G. V Naik, A. Boltasseva, E.E. Narimanov, V.M. Shalaev, Improving the radiative decay rate for dye molecules with hyperbolic metamaterials, *Opt. Express*. 20 (2012) 8100–8116. <https://doi.org/10.1364/OE.20.008100>.
- [89] T. Tumkur, G. Zhu, P. Black, Y.A. Barnakov, C.E. Bonner, M.A. Noginov, Control of spontaneous emission in a volume of functionalized hyperbolic metamaterial, *Appl. Phys. Lett.* 99 (2011) 2009–2012. <https://doi.org/10.1063/1.3631723>.
- [90] X. Yang, J. Yao, J. Rho, X. Yin, X. Zhang, Experimental realization of three-dimensional indefinite cavities at the nanoscale with anomalous scaling laws, *Nat. Photonics*. 6 (2012) 450–454. <https://doi.org/10.1038/nphoton.2012.124>.
- [91] C.R. Simovski, P.A. Belov, A. V. Atrashchenko, Y.S. Kivshar, Wire metamaterials: Physics and applications, *Adv. Mater.* 24 (2012) 4229–4248. <https://doi.org/10.1002/adma.201200931>.
- [92] M.G. Silveirinha, Nonlocal homogenization model for a periodic array of -negative rods, *Phys. Rev. E - Stat. Nonlinear, Soft Matter Phys.* 73 (2006) 1–10. <https://doi.org/10.1103/PhysRevE.73.046612>.
- [93] A. V Kabashin, P. Evans, S. Pastkovsky, W. Hendren, G.A. Wurtz, R. Atkinson, R. Pollard, V.A. Podolskiy, A. V Zayats, Plasmonic nanorod metamaterials for biosensing, *Nat. Mater.* 8 (2009) 867–871. <https://doi.org/10.1038/nmat2546>.
- [94] S. Atakaramians, A. Argyros, S.C. Fleming, B.T. Kuhlmeiy, Hollow-core waveguides with uniaxial metamaterial cladding: modal equations and guidance conditions, *J. Opt. Soc. Am. B*. 29 (2012) 2462–2477. <https://doi.org/10.1364/JOSAB.29.002462>.
- [95] H. Yu, Y. Peng, Y. Yang, Z.Y. Li, Plasmon-enhanced light–matter interactions and applications, *Npj Comput. Mater.* 5 (2019) 1–14. <https://doi.org/10.1038/s41524-019-0184-1>.
- [96] S. Zeng, D. Baillargeat, H.P. Ho, K.T. Yong, Nanomaterials enhanced surface plasmon resonance for biological and chemical sensing applications, *Chem. Soc. Rev.* 43 (2014) 3426–3452. <https://doi.org/10.1039/c3cs60479a>.
- [97] Y. Tang, X. Zeng, J. Liang, Surface Plasmon Resonance: An Introduction to a Surface Spectroscopy Technique, *J. Chem. Educ.* 87 (2010) 742–746. <https://doi.org/10.1021/ed100186y>.

- [98] J.F. Masson, Surface Plasmon Resonance Clinical Biosensors for Medical Diagnostics, *ACS Sensors*. 2 (2017) 16–30. <https://doi.org/10.1021/acssensors.6b00763>.
- [99] A.K. Sharma, R. Jha, B.D. Gupta, Fiber-optic sensors based on surface plasmon resonance: A comprehensive review, *IEEE Sens. J.* 7 (2007) 1118–1129. <https://doi.org/10.1109/JSEN.2007.897946>.
- [100] K.M. Kosuda, J.M. Bingham, K.L. Wustholz, R.P. Van Duyne, R.J. Groarke, Nanostructures and Surface-Enhanced Raman Spectroscopy, in: D.L. Andrews, R.H. Lipson, T.B.T.-C.N. and N. (Second E. Nann (Eds.), *Compr. Nanosci. Nanotechnol.*, Elsevier, Oxford, 2016: pp. 117–152. <https://doi.org/10.1016/B978-0-12-803581-8.00611-1>.
- [101] V.G. Kravets, A. V. Kabashin, W.L. Barnes, A.N. Grigorenko, Plasmonic Surface Lattice Resonances: A Review of Properties and Applications, *Chem. Rev.* 118 (2018) 5912–5951. <https://doi.org/10.1021/acs.chemrev.8b00243>.
- [102] T. Lee, G.H. Kim, S.M. Kim, K. Hong, Y. Kim, C. Park, H. Sohn, J. Min, Label-free localized surface plasmon resonance biosensor composed of multi-functional DNA 3 way junction on hollow Au spike-like nanoparticles (HAuSN) for avian influenza virus detection, *Colloids Surfaces B Biointerfaces*. 182 (2019) 110341. <https://doi.org/10.1016/j.colsurfb.2019.06.070>.
- [103] M. Farady, I. Experimental researches in electricity.—Nineteenth series, *Philos. Trans. R. Soc. London*. 136 (1846) 1–20. <https://doi.org/10.1098/rstl.1846.0001>.
- [104] J.T. Chang, J.F. Dillon, U.F. Gianola, Magneto-Optical Variable Memory Based Upon the Properties of a Transparent Ferrimagnetic Garnet at Its Compensation Temperature, *J. Appl. Phys.* 36 (1965) 1110–1111. <https://doi.org/10.1063/1.1714122>.
- [105] Y.S. Didosyan, H. Hauser, H. Wolfmayr, J. Nicolics, P. Fulmek, Magneto-optical rotational speed sensor, *Sensors Actuators, A Phys.* 106 (2003) 168–171. [https://doi.org/10.1016/S0924-4247\(03\)00158-4](https://doi.org/10.1016/S0924-4247(03)00158-4).
- [106] N.O. Urs, B. Mozooni, P. Mazalski, M. Kustov, P. Hayes, S. Deldar, E. Quandt, J. McCord, Advanced magneto-optical microscopy: Imaging from picoseconds to centimeters - imaging spin waves and temperature distributions (invited), *AIP Adv.* 6 (2016) 55605. <https://doi.org/10.1063/1.4943760>.
- [107] J. Kerr, XL. A new relation between electricity and light: Dielectrified media birefringent, *London, Edinburgh, Dublin Philos. Mag. J. Sci.* 50 (1875) 337–348. <https://doi.org/10.1080/14786447508641302>.
- [108] J. Kerr, LIV. A new relation between electricity and light: Dielectrified media birefringent (Second paper), *London, Edinburgh, Dublin Philos. Mag. J. Sci.* 50 (1875) 446–458. <https://doi.org/10.1080/14786447508641319>.

- [109] T. Haider, A Review of Magneto-Optic Effects and Its Application, *Int. J. Electromagn. Appl.* 7 (2017) 17–24. <https://doi.org/10.5923/j.ijea.20170701.03>.
- [110] I.S. Maksymov, Magneto-plasmonic nanoantennas: Basics and applications, *Rev. Phys.* 1 (2016) 36–51. <https://doi.org/10.1016/j.revip.2016.03.002>.
- [111] Z. Ayareh, S. Mahmoodi, M. Moradi, Magneto-plasmonic biosensing platform for detection of glucose concentration, *Optik (Stuttg)*. 178 (2019) 765–773. <https://doi.org/10.1016/j.ijleo.2018.10.066>.
- [112] G. Armelles, L. Bergamini, N. Zabala, F. García, M.L. Dotor, L. Torné, R. Alvaro, A. Griol, A. Martínez, J. Aizpurua, A. Cebollada, Metamaterial Platforms for Spintronic Modulation of Mid-Infrared Response under Very Weak Magnetic Field, *ACS Photonics*. 5 (2018) 3956–3961. <https://doi.org/10.1021/acsphotonics.8b00866>.
- [113] A. Biswas, I.S. Bayer, A.S. Biris, T. Wang, E. Dervishi, F. Faupel, Advances in top-down and bottom-up surface nanofabrication: Techniques, applications & future prospects, *Adv. Colloid Interface Sci.* 170 (2012) 2–27. <https://doi.org/10.1016/j.cis.2011.11.001>.
- [114] A. Pimpin, W. Srituravanich, Reviews on micro- and nanolithography techniques and their applications, *Eng. J.* 16 (2012) 37–55. <https://doi.org/10.4186/ej.2012.16.1.37>.
- [115] S. Kumar, S. Tanwar, S.K. Sharma, Nanoantenna – A Review on Present and Future Perspective, *ISSN (Online)*. 4 (2016) 2348–4098. <https://doi.org/10.2348/ijset0116240>.
- [116] L. Guo, P.R. Krauss, S.Y. Chou, Nanoscale silicon field effect transistors fabricated using imprint lithography, *Appl. Phys. Lett.* 71 (1997) 1881–1883. <https://doi.org/10.1063/1.119426>.
- [117] G.L.-T. Chiu, J.M. Shaw, Optical lithography: Introduction, *IBM J. Res. Dev.* 41 (1997) 3–6. <https://doi.org/10.1147/rd.411.0003>.
- [118] B.D. Gates, Q. Xu, M. Stewart, D. Ryan, C.G. Willson, G.M. Whitesides, New approaches to nanofabrication: Molding, printing, and other techniques, *Chem. Rev.* 105 (2005) 1171–1196. <https://doi.org/10.1021/cr030076o>.
- [119] S. Hashioka, M. Saito, E. Tamiya, H. Matsumura, Metal nanogap devices fabricated by conventional photolithography and their application to deoxyribose nucleic acid analysis, *J. Vac. Sci. Technol. B Microelectron. Nanom. Struct. Process. Meas. Phenom.* 21 (2003) 2937–2940. <https://doi.org/10.1116/1.1625961>.
- [120] M.C. Smayling, V. Axelrad, 32Nm and Below Logic Patterning Using Optimized Illumination and Double Patterning, *Opt. Microlithogr. XXII*. 7274 (2009) 72740K. <https://doi.org/10.1117/12.814258>.
- [121] Z.L. Wang, Zinc oxide nanostructures: Growth, properties and applications, *J. Phys. Condens. Matter*. 16 (2004). <https://doi.org/10.1088/0953-8984/16/25/R01>.

- [122] L. Schmidt-Mende, J.L. MacManus-Driscoll, ZnO - nanostructures, defects, and devices, *Mater. Today*. 10 (2007) 40–48. [https://doi.org/10.1016/S1369-7021\(07\)70078-0](https://doi.org/10.1016/S1369-7021(07)70078-0).
- [123] J. Huang, L. Li, P. Lu, Z. Qi, X. Sun, X. Zhang, H. Wang, Self-assembled Co-BaZrO₃ nanocomposite thin films with ultra-fine vertically aligned Co nanopillars, *Nanoscale*. 9 (2017) 7970–7976. <https://doi.org/10.1039/c7nr01122a>.
- [124] R. Jiang, X. Meng, Synthesis of aluminum nitride nanostructures via chemical vapor deposition method with nickel as catalyst, *Rev. Mex. Fis.* 64 (2018) 67–71. <https://doi.org/10.31349/revmexfis.64.67>.
- [125] O.I. Lebedev, J. Verbeeck, G. Van Tendeloo, O. Shapoval, A. Belenchuk, V. Moshnyaga, B. Damashcke, K. Samwer, Structural phase transitions and stress accommodation in (formula presented) composite films, *Phys. Rev. B - Condens. Matter Mater. Phys.* 66 (2002) 1–10. <https://doi.org/10.1103/PhysRevB.66.104421>.
- [126] M. Fan, H. Wang, S. Misra, B. Zhang, Z. Qi, X. Sun, J. Huang, H. Wang, Microstructure, Magnetic, and Magnetoresistance Properties of La_{0.7}Sr_{0.3}MnO₃:CuO Nanocomposite Thin Films, *ACS Appl. Mater. Interfaces*. 10 (2018) 5779–5784. <https://doi.org/10.1021/acsami.7b17398>.
- [127] J. Huang, A. Gellatly, A. Kauffmann, X. Sun, H. Wang, Exchange Bias Effect along Vertical Interfaces in La_{0.7}Sr_{0.3}MnO₃:NiO Vertically Aligned Nanocomposite Thin Films Integrated on Silicon Substrates, *Cryst. Growth Des.* 18 (2018) 4388–4394. <https://doi.org/10.1021/acs.cgd.8b00366>.
- [128] M. Fan, H. Wang, S. Misra, B. Zhang, Z. Qi, X. Sun, J. Huang, H. Wang, Microstructure, Magnetic, and Magnetoresistance Properties of La_{0.7}Sr_{0.3}MnO₃:CuO Nanocomposite Thin Films, *ACS Appl. Mater. Interfaces*. 10 (2018) 5779–5784. <https://doi.org/10.1021/acsami.7b17398>.
- [129] X. Sun, J. Huang, J. Jian, M. Fan, H. Wang, Q. Li, J.L. Mac Manus-Driscoll, P. Lu, X. Zhang, H. Wang, Three-dimensional strain engineering in epitaxial vertically aligned nanocomposite thin films with tunable magnetotransport properties, *Mater. Horizons*. 5 (2018) 536–544. <https://doi.org/10.1039/c8mh00216a>.
- [130] A. Chen, Z. Bi, C.F. Tsai, J. Lee, Q. Su, X. Zhang, Q. Jia, J.L. MacManus-Driscoll, H. Wang, Tunable low-field magnetoresistance in (La_{0.7}Sr_{0.3}MnO₃)_{0.5}:(ZnO)_{0.5} self-assembled vertically aligned nanocomposite thin films, *Adv. Funct. Mater.* 21 (2011) 2423–2429. <https://doi.org/10.1002/adfm.201002746>.
- [131] F. Khatkhatay, A. Chen, J.H. Lee, W. Zhang, H. Abdel-Raziq, H. Wang, Ferroelectric properties of vertically aligned nanostructured BaTiO₃-CeO₂ thin films and their integration on silicon, *ACS Appl. Mater. Interfaces*. 5 (2013) 12541–12547. <https://doi.org/10.1021/am403834k>.

- [132] W. Zhang, J. Jian, A. Chen, L. Jiao, F. Khatkhatay, L. Li, F. Chu, Q. Jia, J.L. MacManus-Driscoll, H. Wang, Strain relaxation and enhanced perpendicular magnetic anisotropy in $\text{BiFeO}_3:\text{CoFe}_2\text{O}_4$ vertically aligned nanocomposite thin films, *Appl. Phys. Lett.* 104 (2014) 062402. <https://doi.org/10.1063/1.4864405>.
- [133] W. Zhang, M. Fan, L. Li, A. Chen, Q. Su, Q. Jia, J.L. MacManus-Driscoll, H. Wang, Heterointerface design and strain tuning in epitaxial $\text{BiFeO}_3:\text{CoFe}_2\text{O}_4$ nanocomposite films, *Appl. Phys. Lett.* 107 (2015) 212901. <https://doi.org/10.1063/1.4936157>.
- [134] X. Gao, L. Li, J. Jian, H. Wang, M. Fan, J. Huang, X. Wang, H. Wang, Vertically Aligned Nanocomposite $\text{BaTiO}_3:\text{YMnO}_3$ Thin Films with Room Temperature Multiferroic Properties toward Nanoscale Memory Devices, *ACS Appl. Nano Mater.* 1 (2018) 2509–2514. <https://doi.org/10.1021/acsanm.8b00614>.
- [135] J. Huang, J.L. MacManus-Driscoll, H. Wang, New epitaxy paradigm in epitaxial self-assembled oxide vertically aligned nanocomposite thin films, *J. Mater. Res.* 32 (2017) 4054–4066. <https://doi.org/10.1557/jmr.2017.281>.
- [136] L. Mohaddes-Ardabili, H. Zhe\ng, S.B. Ogale, B. Hannoyer, W. Tian, J. Wang, S.E. Lofland, S.R. Shinde, T. Zhao, Y. Jia, L. Salamanca-Riba, D.G. Schlom, M. Wuttig, R. Ramesh, Self-assembled single-crystal ferromagnetic iron nanowires formed by decomposition., *Nat. Mater.* 3 (2004) 533–538. <https://doi.org/10.1038/nmat1162>.
- [137] J. Huang, Z. Qi, L. Li, H. Wang, S. Xue, B. Zhang, X. Zhang, H. Wang, Self-assembled vertically aligned Ni nanopillars in CeO_2 with anisotropic magnetic and transport properties for energy applications, *Nanoscale.* 10 (2018) 17182–17188. <https://doi.org/10.1039/c8nr05532g>.
- [138] Q. Su, W. Zhang, P. Lu, S. Fang, F. Khatkhatay, J. Jian, L. Li, F. Chen, X. Zhang, J.L. Macmanus-Driscoll, A. Chen, Q. Jia, H. Wang, Self-Assembled Magnetic Metallic Nanopillars in Ceramic Matrix with Anisotropic Magnetic and Electrical Transport Properties, *ACS Appl. Mater. Interfaces.* 8 (2016) 20283–20291. <https://doi.org/10.1021/acsami.6b05999>.
- [139] L. Li, L. Sun, J.S. Gomez-Diaz, N.L. Hogan, P. Lu, F. Khatkhatay, W. Zhang, J. Jian, J. Huang, Q. Su, M. Fan, C. Jacob, J. Li, X. Zhang, Q. Jia, M. Sheldon, A. Alu, X. Li, H. Wang, Self-Assembled Epitaxial Au-Oxide Vertically Aligned Nanocomposites for Nanoscale Metamaterials, *NANO Lett.* 16 (2016) 3936–3943. <https://doi.org/10.1021/acs.nanolett.6b01575>.
- [140] S. Misra, L. Li, J. Jian, J. Huang, X. Wang, D. Zemlyanov, J.W. Jang, F.H. Ribeiro, H. Wang, Tailorable Au Nanoparticles Embedded in Epitaxial TiO_2 Thin Films for Tunable Optical Properties, *ACS Appl. Mater. Interfaces.* 10 (2018) 32895–32902. <https://doi.org/10.1021/acsami.8b12210>.
- [141] J. Huang, J.L. MacManus-Driscoll, H. Wang, New epitaxy paradigm in epitaxial self-assembled oxide vertically aligned nanocomposite thin films, *J. Mater. Res.* 32 (2017) 4054–4066. <https://doi.org/10.1557/jmr.2017.281>.

- [142] A. Chen, M. Weigand, Z. Bi, W. Zhang, X. Lu, P. Dowden, J.L. Macmanus-driscoll, H. Wang, Q. Jia, Evolution of microstructure, strain and physical properties in oxide nanocomposite films, *Sci. Rep.* 4 (2014) 1–7. <https://doi.org/10.1038/srep05426>.
- [143] B. Zhang, J. Huang, J. Jian, B.X. Rutherford, L. Li, S. Misra, X. Sun, H. Wang, Tuning magnetic anisotropy in Co-BaZrO₃ vertically aligned nanocomposites for memory device integration, *Nanoscale Adv.* 1 (2019) 4450–4458. <https://doi.org/10.1039/c9na00438f>.
- [144] S. Misra, L. Li, D. Zhang, J. Jian, Z. Qi, M. Fan, H.-T. Chen, X. Zhang, H. Wang, Self-Assembled Ordered Three-Phase Au-BaTiO₃-ZnO Vertically Aligned Nanocomposites Achieved by a Templating Method, *Adv. Mater.* 31 (2019) 1806529. <https://doi.org/10.1002/adma.201806529>.
- [145] S.M. Shang, W. Zeng, Conductive nanofibres and nanocoatings for smart textiles, 2013. <https://doi.org/10.1533/9780857093530.1.92>.
- [146] A.K. Chatterjee, X-Ray Diffraction, in: V.S. Ramachandran, J.J.B.T.-H. of A.T. in C.S. and T. Beaudoin (Eds.), *Handb. Anal. Tech. Concr. Sci. Technol.*, Elsevier, Norwich, NY, 2001: pp. 275–332. <https://doi.org/10.1016/B978-081551437-4.50011-4>.
- [147] S.J. Pennycook, A.R. Lupini, M. Varela, A. Borisevich, Y. Peng, M.P. Oxley, K. Van Benthem, M.F. Chisholm, Scanning Transmission Electron Microscopy for Nanostructure Characterization, in: *Scanning Microsc. Nanotechnol.*, Springer New York, New York, NY, 2006: pp. 152–191. https://doi.org/10.1007/978-0-387-39620-0_6.
- [148] V.-M. Airaksinen, Silicon Wafer and Thin Film Measurements, in: *Handb. Silicon Based MEMS Mater. Technol.*, Elsevier, 2015: pp. 381–390. <https://doi.org/10.1016/B978-0-323-29965-7.00015-4>.
- [149] M. Fan, B. Zhang, H. Wang, J. Jian, X. Sun, J. Huang, L. Li, X. Zhang, H. Wang, Self-Organized Epitaxial Vertically Aligned Nanocomposites with Long-Range Ordering Enabled by Substrate Nanotemplating, *Adv. Mater.* 29 (2017).
- [150] I. Žutić, J. Fabian, S. Das Sarma, Spintronics: Fundamentals and applications, *Rev. Mod. Phys.* 76 (2004) 323–410. <https://doi.org/10.1103/RevModPhys.76.323>.
- [151] S.A. Wolf, Spintronics: A Spin-Based Electronics Vision for the Future, *Science* (80-.). 294 (2001) 1488–1495. <https://doi.org/10.1126/science.1065389>.
- [152] S.A. Wolf, J. Lu, M.R. Stan, E. Chen, D.M. Treger, The promise of nanomagnetism and spintronics for future logic and universal memory, *Proc. IEEE.* 98 (2010) 2155–2168. <https://doi.org/10.1109/JPROC.2010.2064150>.
- [153] J. Wang, H. Meng, J.P. Wang, Programmable spintronics logic device based on a magnetic tunnel junction element, *J. Appl. Phys.* 97 (2005) 95–98. <https://doi.org/10.1063/1.1857655>.

- [154] R. Lavrijsen, J. Lee, A. Fernández-Pacheco, D.C.M.C. Petit, R. Mansell, R.P. Cowburn, Magnetic ratchet for three-dimensional spintronic memory and logic., *Nature*. 493 (2013) 647–50. <https://doi.org/10.1038/nature11733>.
- [155] W. Shen, X. Liu, D. Mazumdar, G. Xiao, In situ detection of single micron-sized magnetic beads using magnetic tunnel junction sensors, *Appl. Phys. Lett.* 86 (2005) 1–3. <https://doi.org/10.1063/1.1952582>.
- [156] N. Nishimura, T. Hirai, A. Koganei, T. Ikeda, K. Okano, Y. Sekiguchi, Y. Osada, Magnetic tunnel junction device with perpendicular magnetization films for high-density magnetic random access memory, *J. Appl. Phys.* 91 (2002) 5246–5249. <https://doi.org/10.1063/1.1459605>.
- [157] J.S. Moodera, L.R. Kinder, T.M. Wong, R. Meservey, Large magnetoresistance at room temperature in ferromagnetic thin film tunnel junctions, *Phys. Rev. Lett.* 74 (1995) 3273–3276. <https://doi.org/10.1103/PhysRevLett.74.3273>.
- [158] D. Pantel, S. Goetze, D. Hesse, M. Alexe, Reversible electrical switching of spin polarization in multiferroic tunnel junctions., *Nat. Mater.* 11 (2012) 289–93. <https://doi.org/10.1038/nmat3254>.
- [159] E.Y. Tsymbal, APPLIED PHYSICS: Tunneling Across a Ferroelectric, *Science* (80-.). 313 (2006) 181–183. <https://doi.org/10.1126/science.1126230>.
- [160] M. Gajek, J.J. Nowak, J.Z. Sun, P.L. Trouilloud, E.J. O’Sullivan, D.W. Abraham, M.C. Gaidis, G. Hu, S. Brown, Y. Zhu, R.P. Robertazzi, W.J. Gallagher, D.C. Worledge, Spin torque switching of 20 nm magnetic tunnel junctions with perpendicular anisotropy, *Appl. Phys. Lett.* 100 (2012) 7–10. <https://doi.org/10.1063/1.3694270>.
- [161] M. Nakayama, T. Kai, N. Shimomura, M. Amano, E. Kitagawa, T. Nagase, M. Yoshikawa, T. Kishi, S. Ikegawa, H. Yoda, Spin transfer switching in TbCoFeCoFeBMgOCFeBTbCoFe magnetic tunnel junctions with perpendicular magnetic anisotropy, *J. Appl. Phys.* 103 (2008) 101–104. <https://doi.org/10.1063/1.2838335>.
- [162] A. Chen, Z. Bi, H. Hazariwala, X. Zhang, Q. Su, L. Chen, Q. Jia, J.L. Macmanus-Driscoll, H. Wang, Microstructure, magnetic, and low-field magnetotransport properties of self-assembled (La_{0.7}Sr_{0.3}MnO₃)_{0.5}:(CeO₂)_{0.5} vertically aligned nanocomposite thin films., *Nanotechnology*. 22 (2011) 1–6. <https://doi.org/10.1088/0957-4484/22/31/315712>.
- [163] Q. Su, D. Yoon, A. Chen, F. Khatkhatay, A. Manthiram, H. Wang, Vertically aligned nanocomposite electrolytes with superior out-of-plane ionic conductivity for solid oxide fuel cells, *J. Power Sources*. 242 (2013) 455–463. <https://doi.org/10.1016/j.jpowsour.2013.05.137>.
- [164] W. Zhang, L. Li, P. Lu, M. Fan, Q. Su, F. Khatkhatay, A. Chen, Q. Jia, X. Zhang, J.L. MacManus-Driscoll, H. Wang, Perpendicular Exchange-Biased Magnetotransport at the Vertical Heterointerfaces in La_{0.7}Sr_{0.3}MnO₃:NiO Nanocomposites, *ACS Appl. Mater. Interfaces*. 7 (2015) 21646–21651. <https://doi.org/10.1021/acsami.5b06314>.

- [165] Q. Su, D. Yoon, Z. Sisman, F. Khatkhatay, Q. Jia, A. Manthiram, H. Wang, Vertically aligned nanocomposite $\text{La}_{0.8}\text{Sr}_{0.2}\text{MnO}_{3-x}\text{Zr}_{0.92}\text{Y}_{0.08}\text{O}_{1.96}$ thin films as electrode/electrolyte interfacial layer for solid oxide reversible fuel cells, *Int. J. Hydrogen Energy*. 38 (2013) 16320–16327. <https://doi.org/10.1016/j.ijhydene.2013.09.128>.
- [166] X.-G. Zhang, W.H. Butler, A. Bandyopadhyay, Effects of the iron-oxide layer in Fe-FeO-MgO-Fe tunneling junctions, *Phys. Rev. B*. 68 (2003) 6–9. <https://doi.org/10.1103/PhysRevB.68.092402>.
- [167] D.L. Leslie-Pelecky, R.D. Rieke, Magnetic Properties of Nanostructured Materials, *Chem. Mater.* 8 (1996) 1770–1783. <https://doi.org/10.1021/cm960077f>.
- [168] C.P. Luo, D.J. Sellmyer, Structural and magnetic properties of FePt:SiO_2 granular thin films, *Appl. Phys. Lett.* 75 (1999) 3162. <https://doi.org/10.1063/1.125264>.
- [169] A.F. Vincent, S. Member, J. Larroque, N. Locatelli, N. Ben Romdhane, O. Bichler, C. Gamrat, W. Sheng Zhao, S. Member, J. Klein, S. Galdin-Retailleau, D. Querlioz, Spin-Transfer Torque Magnetic Memory as a Stochastic Memristive Synapse for Neuromorphic Systems, *IEEE Trans. Biomed. Circuits Syst.* 9 (2015) 166–174. <https://doi.org/10.1109/TBCAS.2015.2414423>.
- [170] Z. Diao, Z. Li, S. Wang, Y. Ding, A. Panchula, E. Chen, L. Wang, Y. Huai, Spin-transfer torque switching in magnetic tunnel junctions and spin-transfer torque random access memory, *J. Phys. Condens. Matter*. 19 (2007) 165209. <https://doi.org/10.1088/0953-8984/19/16/165209>.
- [171] B. Dieny, M. Chshiev, Perpendicular magnetic anisotropy at transition metal/oxide interfaces and applications, *Rev. Mod. Phys.* 89 (2017) 025008. <https://doi.org/10.1103/RevModPhys.89.025008>.
- [172] Y. Zhang, X. Lin, J.P. Adam, G. Agnus, W. Kang, W. Cai, J.R. Coudeville, N. Isac, J. Yang, H. Yang, K. Cao, H. Cui, D. Zhang, Y. Zhang, C. Zhao, W. Zhao, D. Ravelosona, Heterogeneous Memristive Devices Enabled by Magnetic Tunnel Junction Nanopillars Surrounded by Resistive Silicon Switches, *Adv. Electron. Mater.* 4 (2018) 1–8. <https://doi.org/10.1002/aelm.201700461>.
- [173] Y. Yin, W. Huang, Y. Liu, S. Yang, S. Dong, J. Tao, Y.-M. Zhu, Q. Li, X.-G. Li, Octonary Resistance States in $\text{La}_{0.7}\text{Sr}_{0.3}\text{MnO}_3/\text{BaTiO}_3/\text{La}_{0.7}\text{Sr}_{0.3}\text{MnO}_3$ Multiferroic Tunnel Junctions, *Adv. Electron. Mater.* 1 (2015) 1500183. <https://doi.org/10.1002/aelm.201500183>.
- [174] S. Lakshmanan, S.K. Rao, M.R. Muthuvel, G. Chandrasekaran, H.A. Therese, Variable substrate temperature deposition of CoFeB film on Ta for manipulating the perpendicular coercive forces, *J. Magn. Mater.* 435 (2017) 81–86. <https://doi.org/10.1016/j.jmmm.2017.03.069>.

- [175] N. Strelkov, A. Chavent, A. Timopheev, R.C. Sousa, I.L. Prejbeanu, L.D. Buda-Prejbeanu, B. Dieny, Impact of Joule heating on the stability phase diagrams of perpendicular magnetic tunnel junctions, *Phys. Rev. B.* 98 (2018) 214410. <https://doi.org/10.1103/PhysRevB.98.214410>.
- [176] H. Liu, D. Bedau, D. Backes, J.A. Katine, J. Langer, A.D. Kent, Ultrafast switching in magnetic tunnel junction based orthogonal spin transfer devices, *Appl. Phys. Lett.* 97 (2010) 242510. <https://doi.org/10.1063/1.3527962>.
- [177] M.M. Vopson, S. Lepadatu, Solving the electrical control of magnetic coercive field paradox, *Appl. Phys. Lett.* 122901 (2014) 1–5. <https://doi.org/10.1063/1.4896521>.
- [178] I.M. Miron, K. Garello, G. Gaudin, P.J. Zermatten, M. V. Costache, S. Auffret, S. Bandiera, B. Rodmacq, A. Schuhl, P. Gambardella, Perpendicular switching of a single ferromagnetic layer induced by in-plane current injection, *Nature.* 476 (2011) 189–193. <https://doi.org/10.1038/nature10309>.
- [179] B. Tudu, A. Tiwari, Recent Developments in Perpendicular Magnetic Anisotropy Thin Films for Data Storage Applications, *Vacuum.* 146 (2017) 329–341. <https://doi.org/10.1016/j.vacuum.2017.01.031>.
- [180] J. Sayama, T. Asahi, K. Mizutani, T. Osaka, Newly developed SmCo 5 thin film with perpendicular magnetic anisotropy, *J. Phys. D. Appl. Phys.* 37 (2004) L1–L4. <https://doi.org/10.1088/0022-3727/37/1/L01>.
- [181] D.D. Djayaprawira, K. Tsunekawa, M. Nagai, H. Maehara, S. Yamagata, N. Watanabe, S. Yuasa, Y. Suzuki, K. Ando, 230% room-temperature magnetoresistance in CoFeBMgOCoFeB magnetic tunnel junctions, *Appl. Phys. Lett.* 86 (2005) 1–3. <https://doi.org/10.1063/1.1871344>.
- [182] H. Sato, E.C.I. Enobio, M. Yamanouchi, S. Ikeda, S. Fukami, S. Kanai, F. Matsukura, H. Ohno, Properties of magnetic tunnel junctions with a MgO/CoFeB/Ta/CoFeB/MgO recording structure down to junction diameter of 11nm, *Appl. Phys. Lett.* 105 (2014) 1–5. <https://doi.org/10.1063/1.4892924>.
- [183] K. Mizunuma, M. Yamanouchi, H. Sato, S. Ikeda, S. Kanai, F. Matsukura, Size Dependence of Magnetic Properties of Nanoscale CoFeB–MgO Magnetic Tunnel Junctions with Perpendicular Magnetic Easy Axis Observed by Ferromagnetic Resonance, *Appl. Phys. Express.* 6 (2013) 63002. <https://doi.org/10.7567/APEX.6.063002>.
- [184] G. Xia, Y. Tan, F. Wu, F. Fang, D. Sun, Z. Guo, Z. Huang, X. Yu, Graphene-wrapped reversible reaction for advanced hydrogen storage, *Nano Energy.* 26 (2016) 488–495. <https://doi.org/10.1016/j.nanoen.2016.06.016>.
- [185] P.F. Carcia, A.D. Meinhaldt, A. Suna, Perpendicular magnetic anisotropy in Pd/Co thin film layered structures, *Appl. Phys. Lett.* 47 (1985) 178–180. <https://doi.org/10.1063/1.96254>.

- [186] D. Kan, R. Aso, R. Sato, M. Haruta, H. Kurata, Y. Shimakawa, Tuning magnetic anisotropy by interfacially engineering the oxygen coordination environment in a transition metal oxide, *Nat. Mater.* 15 (2016) 432–437. <https://doi.org/10.1038/nmat4580>.
- [187] X. Qiao, B. Wang, Z. Tang, Y. Shen, H. Yang, J. Wang, Q. Zhan, S. Mao, X. Xu, R.-W. Li, Tuning magnetic anisotropy of amorphous CoFeB film by depositing on convex flexible substrates, *AIP Adv.* 6 (2016) 056106. <https://doi.org/10.1063/1.4943153>.
- [188] S. Lee, W.R. Zhang, F. Khatkhatay, H.Y. Wang, Q.X. Jia, J.L. MacManus-Driscoll, Ionic Conductivity Increased by Two Orders of Magnitude in Micrometer-Thick Vertical Yttria-Stabilized ZrO₂ Nanocomposite Films, *Nano Lett.* 15 (2015) 7362–7369. <https://doi.org/10.1021/acs.nanolett.5b02726>.
- [189] J.L. Macmanus-Driscoll, Self-assembled heteroepitaxial oxide nanocomposite thin film structures: Designing interface-induced functionality in electronic materials, *Adv. Funct. Mater.* 20 (2010) 2035–2045. <https://doi.org/10.1002/adfm.201000373>.
- [190] W.R. Zhang, A.P. Chen, J. Jian, Y.Y. Zhu, L. Chen, P. Lu, Q.X. Jia, J.L. MacManus-Driscoll, X.H. Zhang, H.Y. Wang, Strong perpendicular exchange bias in epitaxial La_{0.7}Sr_{0.3}MnO₃:BiFeO₃ nanocomposite films through vertical interfacial coupling, *Nanoscale*. 7 (2015) 13808–13815. <https://doi.org/10.1039/c5nr03231h>.
- [191] B. Zhang, M. Fan, L. Li, J. Jian, J. Huang, H. Wang, M. Kalaswad, H. Wang, Tunable magnetic anisotropy of self-assembled Fe nanostructures within a La_{0.5}Sr_{0.5}FeO₃ matrix, *Appl. Phys. Lett.* 112 (2018) 013104. <https://doi.org/10.1063/1.5008382>.
- [192] M. Gierlings, M.J. Prandolini, H. Fritzsche, M. Gruyters, D. Riegel, Change and asymmetry of magnetization reversal for a Co/CoO exchange-bias system, *Phys. Rev. B - Condens. Matter Mater. Phys.* 65 (2002) 1–4. <https://doi.org/10.1103/PhysRevB.65.092407>.
- [193] T.A. Roth, The surface and grain boundary energies of iron, cobalt and nickel, *Mater. Sci. Eng.* 18 (1975) 183–192. [https://doi.org/10.1016/0025-5416\(75\)90168-8](https://doi.org/10.1016/0025-5416(75)90168-8).
- [194] R.I. Eglitis, First-principles calculations of BaZrO₃ (001) and (011) surfaces, *J. Phys. Condens. Matter*. 19 (2007) 356004. <https://doi.org/10.1088/0953-8984/19/35/356004>.
- [195] B. Meyer, J. Padilla, D. Vanderbilt, Theory of PbTiO₃, BaTiO₃, and SrTiO₃ surfaces, *Faraday Discuss.* 114 (1999) 395–405. <https://doi.org/10.1039/a903029h>.
- [196] X. Sun, Q. Li, J. Huang, J. Jian, P. Lu, X. Zhang, J.L. MacManus-Driscoll, H. Wang, Strain and property tuning of the 3D framed epitaxial nanocomposite thin films via interlayer thickness variation, *J. Appl. Phys.* 125 (2019) 082530. <https://doi.org/10.1063/1.5053705>.
- [197] K. Tarawneh, N. Al-Aqtash, R. Sabirianov, Large magnetoresistance in planar Fe/MoS₂/Fe tunnel junction, *Comput. Mater. Sci.* 124 (2016) 15–22. <https://doi.org/10.1016/j.commatsci.2016.06.005>.

- [198] J.L. MacManus-Driscoll, P. Zerrer, H. Wang, H. Yang, J. Yoon, A. Fouchet, R. Yu, M.G. Blamire, Q. Jia, Strain control and spontaneous phase ordering in vertical nanocomposite heteroepitaxial thin films, *Nat. Mater.* 7 (2008) 314–320. <https://doi.org/10.1038/nmat2124>.
- [199] W. Zhang, M. Fan, L. Li, A. Chen, Q. Su, Q. Jia, J.L. MacManus-Driscoll, H. Wang, Heterointerface design and strain tuning in epitaxial $\text{BiFeO}_3/\text{CoFe}_2\text{O}_4$ nanocomposite films, *Appl. Phys. Lett.* 107 (2015) 212901. <https://doi.org/10.1063/1.4936157>.
- [200] A. Chen, Z. Bi, Q. Jia, J.L. Macmanus-Driscoll, H. Wang, Microstructure, vertical strain control and tunable functionalities in self-assembled, vertically aligned nanocomposite thin films, *Acta Mater.* 61 (2013) 2783–2792. <https://doi.org/10.1016/j.actamat.2012.09.072>.
- [201] A. Chen, Z. Harrell, P. Lu, E. Enriquez, L. Li, B. Zhang, P. Dowden, C. Chen, H. Wang, J.L. MacManus-Driscoll, Q. Jia, Strain Enhanced Functionality in a Bottom-Up Approach Enabled 3D Super-Nanocomposites, *Adv. Funct. Mater.* 1900442 (2019) 1–8. <https://doi.org/10.1002/adfm.201900442>.
- [202] M. Fan, W. Zhang, J. Jian, J. Huang, H. Wang, Strong perpendicular exchange bias in epitaxial $\text{La}_{0.7}\text{Sr}_{0.3}\text{MnO}_3/\text{LaFeO}_3$ nanocomposite thin films, *APL Mater.* 4 (2016) 076105. <https://doi.org/10.1063/1.4958965>.
- [203] W. Zhang, L. Li, P. Lu, M. Fan, Q. Su, F. Khatkhatay, A. Chen, Q. Jia, X. Zhang, J.L. MacManus-Driscoll, H. Wang, Perpendicular Exchange-Biased Magnetotransport at the Vertical Heterointerfaces in $\text{La}_{0.7}\text{Sr}_{0.3}\text{MnO}_3/\text{NiO}$ Nanocomposites, *ACS Appl. Mater. Interfaces.* 7 (2015) 21646–21651. <https://doi.org/10.1021/acsami.5b06314>.
- [204] B. Zhang, M. Fan, L. Li, J. Jian, J. Huang, H. Wang, M. Kalaswad, H. Wang, Tunable magnetic anisotropy of self-assembled Fe nanostructures within a $\text{La}_{0.5}\text{Sr}_{0.5}\text{FeO}_3$ matrix, *Appl. Phys. Lett.* 112 (2018) 0–5. <https://doi.org/10.1063/1.5008382>.
- [205] L. Li, L. Sun, J.S. Gomez-Diaz, N.L. Hogan, P. Lu, F. Khatkhatay, W. Zhang, J. Jian, J. Huang, Q. Su, M. Fan, C. Jacob, J. Li, X. Zhang, Q. Jia, M. Sheldon, A. Alù, X. Li, H. Wang, Self-assembled epitaxial Au-oxide vertically aligned nanocomposites for nanoscale metamaterials, *Nano Lett.* 16 (2016) 3936–3943. <https://doi.org/10.1021/acs.nanolett.6b01575>.
- [206] K.J. Choi, M. Biegalski, Y.L. Li, A. Sharan, J. Schubert, R. Uecker, P. Reiche, Y.B. Chen, X.Q. Pan, V. Gopalan, L.-Q. Chen, D.G. Schlom, C.B. Eom, Enhancement of ferroelectricity in strained BaTiO_3 thin films-supplementary info, *Science.* 306 (2004) 1005-suppl. <https://doi.org/10.1126/science.1103218>.
- [207] L. Huang, Z. Chen, J.D. Wilson, S. Banerjee, R.D. Robinson, I.P. Herman, R. Laibowitz, S. O'Brien, Barium titanate nanocrystals and nanocrystal thin films: Synthesis, ferroelectricity, and dielectric properties, *J. Appl. Phys.* 100 (2006) 034316. <https://doi.org/10.1063/1.2218765>.
- [208] M. Dawber, K.M. Rabe, J.F. Scott, Physics of thin-film ferroelectric oxides, *Rev. Mod. Phys.* 77 (2005) 1083–1130. <https://doi.org/10.1103/RevModPhys.77.1083>.

- [209] V.N. Reddy, K.C. Babu Naidu, T. Subbarao, Structural, optical and ferroelectric properties of BaTiO₃ ceramics, *J. Ovonic Res.* 12 (2016) 185–191.
- [210] V. Mishra, A. Sagdeo, V. Kumar, M.K. Warshi, H.M. Rai, S.K. Saxena, D.R. Roy, V. Mishra, R. Kumar, P.R. Sagdeo, Electronic and optical properties of BaTiO₃ across tetragonal to cubic phase transition: An experimental and theoretical investigation, *J. Appl. Phys.* 122 (2017) 065105. <https://doi.org/10.1063/1.4997939>.
- [211] L.A. Wills, B.W. Wessels, D.S. Richeson, T.J. Marks, Epitaxial growth of BaTiO₃ thin films by organometallic chemical vapor deposition, *Appl. Phys. Lett.* 60 (1992) 41–43. <https://doi.org/10.1063/1.107359>.
- [212] T. Woldu, B. Raneesh, P. Sreekanth, M. V. Ramana Reddy, R. Philip, N. Kalarikkal, Size dependent nonlinear optical absorption in BaTiO₃ nanoparticles, *Chem. Phys. Lett.* 625 (2015) 58–63. <https://doi.org/10.1016/j.cplett.2015.02.020>.
- [213] T. Jin, L. Li, B. Zhang, H.Y.G. Lin, H. Wang, P.T. Lin, Monolithic Mid-Infrared Integrated Photonics Using Silicon-on-Epitaxial Barium Titanate Thin Films, *ACS Appl. Mater. Interfaces.* 9 (2017) 21848–21855. <https://doi.org/10.1021/acsami.7b02681>.
- [214] C. Xiong, W.H.P. Pernice, J.H. Ngai, J.W. Reiner, D. Kumah, F.J. Walker, C.H. Ahn, H.X. Tang, Active silicon integrated nanophotonics: Ferroelectric BaTiO₃ devices, *Nano Lett.* 14 (2014) 1419–1425. <https://doi.org/10.1021/nl404513p>.
- [215] T. Jin, L. Li, B. Zhang, H.Y.G. Lin, H. Wang, P.T. Lin, Real-Time and Label-Free Chemical Sensor-on-a-chip using Monolithic Si-on-BaTiO₃ Mid-Infrared waveguides, *Sci. Rep.* 7 (2017) 5836. <https://doi.org/10.1038/s41598-017-05711-4>.
- [216] T. Jin, L. Li, B. Zhang, H.-Y.G. Lin, H. Wang, P.T. Lin, Epitaxial Barium Titanate Thin Films for Mid-infrared Photonic Circuits, in: *Adv. Photonics 2017 (IPR, NOMA, Sensors, Networks, SPPCom, PS)*, OSA, Washington, D.C., 2017: p. ITh1A.5. <https://doi.org/10.1364/iprsn.2017.ith1a.5>.
- [217] G. Venkataiah, Y. Shirahata, M. Itoh, T. Taniyama, Manipulation of magnetic coercivity of Fe film in Fe/BaTiO₃ heterostructure by electric field, *Appl. Phys. Lett.* 99 (2011) 98–101. <https://doi.org/10.1063/1.3628464>.
- [218] G. Venkataiah, Y. Shirahata, I. Suzuki, M. Itoh, T. Taniyama, Strain-induced reversible and irreversible magnetization switching in Fe/BaTiO₃ heterostructures, *J. Appl. Phys.* 111 (2012) 033921. <https://doi.org/10.1063/1.3684695>.
- [219] Y. Shirahata, T. Nozaki, G. Venkataiah, H. Taniguchi, M. Itoh, T. Taniyama, Switching of the symmetry of magnetic anisotropy in Fe/BaTiO₃ heterostructures, *Appl. Phys. Lett.* 99 (2011) 1–4. <https://doi.org/10.1063/1.3609237>.
- [220] S. Brivio, C. Rinaldi, D. Petti, R. Bertacco, F. Sanchez, Epitaxial growth of Fe/BaTiO₃ heterostructures, *Thin Solid Films.* 519 (2011) 5804–5807. <https://doi.org/10.1016/j.tsf.2010.12.193>.

- [221] K. Samuvel, K. Ramachandran, Structure, electrical and magnetic property investigations on Fe-doped hexagonal BaTiO₃, *Optik (Stuttg)*. 127 (2016) 1781–1786. <https://doi.org/10.1016/j.ijleo.2015.10.240>.
- [222] W.A. Borders, A.Z. Pervaiz, S. Fukami, K.Y. Camsari, H. Ohno, S. Datta, Integer factorization using stochastic magnetic tunnel junctions, *Nature*. 573 (2019) 390–393. <https://doi.org/10.1038/s41586-019-1557-9>.
- [223] M.L. Schneider, C.A. Donnelly, S.E. Russek, B. Baek, M.R. Pufall, P.F. Hopkins, P.D. Dresselhaus, S.P. Benz, W.H. Rippard, Ultralow power artificial synapses using nanotextured magnetic josephson junctions, *Sci. Adv.* 4 (2018). <https://doi.org/10.1126/sciadv.1701329>.
- [224] K. Yue, Y. Liu, R.K. Lake, A.C. Parker, A brain-plausible neuromorphic on-the-fly learning system implemented with magnetic domain wall analog memristors, *Sci. Adv.* 5 (2019) 1–10. <https://doi.org/10.1126/sciadv.aau8170>.
- [225] D.L. Huber, Synthesis, properties, and applications of iron nanoparticles, *Small*. 1 (2005) 482–501. <https://doi.org/10.1002/sml.200500006>.
- [226] B.H. Hoerman, G.M. Ford, L.D. Kaufmann, B.W. Wessels, Dielectric properties of epitaxial BaTiO₃ thin films, *Appl. Phys. Lett.* 73 (1998) 2248–2250. <https://doi.org/10.1063/1.121691>.
- [227] V. Kumar Gudelli, G.Y. Guo, Magnetism and magneto-optical effects in bulk and few-layer CrI₃: A theoretical GGA + U study, *New J. Phys.* 21 (2019). <https://doi.org/10.1088/1367-2630/ab1ae9>.
- [228] T. Higo, H. Man, D.B. Gopman, L. Wu, T. Koretsune, O.M.J. Van 't Erve, Y.P. Kabanov, D. Rees, Y. Li, M.T. Suzuki, S. Patankar, M. Ikhlas, C.L. Chien, R. Arita, R.D. Shull, J. Orenstein, S. Nakatsuji, Large magneto-optical Kerr effect and imaging of magnetic octupole domains in an antiferromagnetic metal, *Nat. Photonics*. 12 (2018) 73–78. <https://doi.org/10.1038/s41566-017-0086-z>.
- [229] L.E. Kreilkamp, V.I. Belotelov, J.Y. Chin, S. Neutzner, D. Dregely, T. Wehls, I.A. Akimov, M. Bayer, B. Stritzker, H. Giessen, Waveguide-plasmon polaritons enhance transverse magneto-optical kerr effect, *Phys. Rev. X*. 3 (2014) 1–7. <https://doi.org/10.1103/PhysRevX.3.041019>.
- [230] H. Dötsch, N. Bahlmann, O. Zhuromskyy, M. Hammer, L. Wilkens, R. Gerhardt, P. Hertel, A.F. Popkov, Applications of magneto-optical waveguides in integrated optics: review, *J. Opt. Soc. Am. B*. 22 (2005) 240. <https://doi.org/10.1364/josab.22.000240>.
- [231] Y. Shiyu, J. Lousteau, M. Olivero, M. Merlo, N. Boetti, S. Abrate, Q. Chen, Q. Chen, D. Milanese, Analysis of Faraday effect in multimode tellurite glass optical fiber for magneto-optical sensing and monitoring applications, *Appl. Opt.* 51 (2012) 4542–4546. <https://doi.org/10.1364/AO.51.004542>.

- [232] M.G. Manera, A. Colombelli, R. Rella, A. Caricato, P.D. Cozzoli, M. Martino, L. Vasanelli, TiO₂ brookite nanostructured thin layer on magneto-optical surface plasmon resonance transducer for gas sensing applications, *J. Appl. Phys.* 112 (2012) 053524. <https://doi.org/10.1063/1.4751347>.
- [233] M. Buchmeier, R. Schreiber, D.E. Bürgler, C.M. Schneider, Thickness dependence of linear and quadratic magneto-optical Kerr effects in ultrathin Fe(001) films, *Phys. Rev. B - Condens. Matter Mater. Phys.* 79 (2009) 1–7. <https://doi.org/10.1103/PhysRevB.79.064402>.
- [234] K. Mok, C. Scarlat, G.J. Kovács, L. Li, V. Zviagin, J. McCord, M. Helm, H. Schmidt, Thickness independent magneto-optical coupling constant of nickel films in the visible spectral range, *J. Appl. Phys.* 110 (2011) 123110. <https://doi.org/10.1063/1.3672834>.
- [235] K. Mok, G.J. Kovács, J. McCord, L. Li, M. Helm, H. Schmidt, Magneto-optical coupling in ferromagnetic thin films investigated by vector-magneto-optical generalized ellipsometry, *Phys. Rev. B - Condens. Matter Mater. Phys.* 84 (2011) 1–6. <https://doi.org/10.1103/PhysRevB.84.094413>.
- [236] R. Schäfer, Magneto-optical domain studies in coupled magnetic multilayers, *J. Magn. Magn. Mater.* 148 (1995) 226–231. [https://doi.org/10.1016/0304-8853\(95\)00218-9](https://doi.org/10.1016/0304-8853(95)00218-9).
- [237] C. Hermann, V.A. Kosobukin, G. Lampel, J. Peretti, V.I. Safarov, P. Bertrand, Surface-enhanced magneto-optics in metallic multilayer films, *Phys. Rev. B - Condens. Matter Mater. Phys.* 64 (2001) 1–11. <https://doi.org/10.1103/PhysRevB.64.235422>.
- [238] H.Y. Feng, F. Luo, R. Arenal, L. Henrard, F. García, G. Armelles, A. Cebollada, Active magnetoplasmonic split-ring/ring nanoantennas, *Nanoscale*. 9 (2017) 37–44. <https://doi.org/10.1039/c6nr07864h>.
- [239] E.M. Larsson, J. Alegret, M. Käll, D.S. Sutherland, Sensing characteristics of NIR localized surface plasmon resonances in gold nanorings for application as ultrasensitive biosensors, *Nano Lett.* 7 (2007) 1256–1263. <https://doi.org/10.1021/nl0701612>.
- [240] H.Y. Feng, F. Luo, R. Kekesi, D. Granados, D. Meneses-Rodríguez, J.M. García, A. García-Martín, G. Armelles, A. Cebollada, Magnetoplasmonic nanorings as novel architectures with tunable magneto-optical activity in wide wavelength ranges, *Adv. Opt. Mater.* 2 (2014) 612–617. <https://doi.org/10.1002/adom.201400125>.
- [241] J.C. Banthí, D. Meneses-Rodríguez, F. García, M.U. González, A. García-Martín, A. Cebollada, G. Armelles, High magneto-optical activity and low optical losses in metal-dielectric Au/Co/Au-SiO₂ magnetoplasmonic nanodisks, *Adv. Mater.* 24 (2012). <https://doi.org/10.1002/adma.201103634>.
- [242] N. Maccaferri, M. Kataja, V. Bonanni, S. Bonetti, Z. Pirzadeh, A. Dmitriev, S. Van Dijken, J. Åkerman, P. Vavassori, Effects of a non-absorbing substrate on the magneto-optical Kerr response of plasmonic ferromagnetic nanodisks, *Phys. Status Solidi Appl. Mater. Sci.* 211 (2014) 1067–1075. <https://doi.org/10.1002/pssa.201300701>.

- [243] F. Freire-Fernández, M. Kataja, S. van Dijken, Surface-plasmon-polariton-driven narrow-linewidth magneto-optics in Ni nanodisk arrays, *Nanophotonics*. 9 (2020) 113–121. <https://doi.org/10.1515/nanoph-2019-0331>.
- [244] D. Erdem, N.S. Bingham, F.J. Heiligt, N. Pilet, P. Warnicke, L.J. Heyderman, M. Niederberger, CoFe₂O₄ and CoFe₂O₄-SiO₂ Nanoparticle Thin Films with Perpendicular Magnetic Anisotropy for Magnetic and Magneto-Optical Applications, *Adv. Funct. Mater.* 26 (2016) 1954–1963. <https://doi.org/10.1002/adfm.201504538>.
- [245] P. Varytis, P.A. Pantazopoulos, N. Stefanou, Enhanced Faraday rotation by crystals of core-shell magnetoplasmonic nanoparticles, *Phys. Rev. B*. 93 (2016) 1–7. <https://doi.org/10.1103/PhysRevB.93.214423>.
- [246] B.C. Choi, H. Xu, G. Hajisalem, R. Gordon, Localized surface plasmon resonance enhanced magneto-optical Kerr effect in Ni₈₀Fe₂₀ thin films coated with Au nanorods, *Appl. Phys. Lett.* 112 (2018) 022403. <https://doi.org/10.1063/1.5011980>.
- [247] M.G. Manera, A. Colombelli, A. Taurino, A.G. Martin, R. Rella, Magneto-Optical properties of noble-metal nanostructures: functional nanomaterials for bio sensing, *Sci. Rep.* 8 (2018) 1–12. <https://doi.org/10.1038/s41598-018-30862-3>.
- [248] T.H.J. Loughran, J. Roth, P.S. Keatley, E. Hendry, W.L. Barnes, R.J. Hicken, J.F. Einsle, A. Amy, W. Hendren, R.M. Bowman, P. Dawson, Design and fabrication of plasmonic cavities for magneto-optical sensing, *AIP Adv.* 8 (2018). <https://doi.org/10.1063/1.5021538>.
- [249] F. Galvez, J. del Valle, A. Gomez, M.R. Osorio, D. Granados, D. Pérez de Lara, M.A. García, J.L. Vicent, Plasmonic nanodevice with magnetic functionalities: fabrication and characterization, *Opt. Mater. Express*. 6 (2016) 3086. <https://doi.org/10.1364/ome.6.003086>.
- [250] E. Atmatzakis, N. Papasimakis, V. Fedotov, N.I. Zheludev, Giant kerr rotation enhancement in magneto-plasmonic metamaterials, *Opt. InfoBase Conf. Pap.* (2014) 1–2. https://doi.org/10.1364/cleo_si.2014.stu1h.6.
- [251] A. Chen, Z. Bi, Q. Jia, J.L. Macmanus-Driscoll, H. Wang, Microstructure, vertical strain control and tunable functionalities in self-assembled, vertically aligned nanocomposite thin films, *Acta Mater.* 61 (2013) 2783–2792. <https://doi.org/10.1016/j.actamat.2012.09.072>.
- [252] J.L. MacManus-Driscoll, A. Suwardi, H. Wang, Composite epitaxial thin films: A new platform for tuning, probing, and exploiting mesoscale oxides, *Mrs Bull.* 40 (2015) 933–942. <https://doi.org/10.1557/mrs.2015.258>.
- [253] W.R. Zhang, R. Ramesh, J.L. MacManus-Driscoll, H.Y. Wang, Multifunctional, self-assembled oxide nanocomposite thin films and devices, *Mrs Bull.* 40 (2015) 736–745. <https://doi.org/10.1557/mrs.2015.198>.

- [254] J. Huang, C.-F. Tsai, L. Chen, J. Jian, F. Khatkhatay, K. Yu, H. Wang, Magnetic properties of $(\text{CoFe}_2\text{O}_4)_x(\text{CeO}_2)_{1-x}$ vertically aligned nanocomposites and their pinning properties in $\text{YBa}_2\text{Cu}_3\text{O}_{7-\delta}$ thin films, *J. Appl. Phys.* 115 (2014) 123902. <https://doi.org/10.1063/1.4869217>.
- [255] A. Chen, H. Zhou, Z. Bi, Y. Zhu, Z. Luo, A. Bayraktaroglu, J. Phillips, E.M. Choi, J.L. MacManus-Driscoll, S.J. Pennycook, J. Narayan, Q. Jia, X. Zhang, H. Wang, A new class of room-temperature multiferroic thin films with bismuth-based supercell structure, *Adv. Mater.* 25 (2013) 1028–1032. <https://doi.org/10.1002/adma.201203051>.
- [256] J.J. Huang, L.G. Li, P. Lu, Z.M. Qi, X. Sun, X.H. Zhang, H.Y. Wang, Self-assembled Co-BaZrO₃ nanocomposite thin films with ultra-fine vertically aligned Co nanopillars, *Nanoscale*. 9 (2017) 7970–7976. <https://doi.org/10.1039/c7nr01122a>.
- [257] X. Wang, J. Jian, S. Diaz-Amaya, C.E. Kumah, P. Lu, J. Huang, D.G. Lim, V.G. Pol, J.P. Youngblood, A. Boltasseva, L.A. Stanciu, D.M. O’Carroll, X. Zhang, H. Wang, Hybrid plasmonic Au-TiN vertically aligned nanocomposites: A nanoscale platform towards tunable optical sensing, *Nanoscale Adv.* 1 (2019) 1045–1054. <https://doi.org/10.1039/c8na00306h>.
- [258] R.L. Paldi, X. Sun, X. Wang, X. Zhang, H. Wang, Strain-Driven In-plane Ordering in Vertically Aligned ZnO-Au Nanocomposites with Highly Correlated Metamaterial Properties, *ACS Omega*. 5 (2020) 2234–2241. <https://doi.org/10.1021/acsomega.9b03356>.
- [259] M. Kalaswad, D. Zhang, X. Gao, L.L. Contreras, H. Wang, X. Wang, H. Wang, Integration of Hybrid Plasmonic Au-BaTiO₃ Metamaterial on Silicon Substrates, *ACS Appl. Mater. Interfaces*. 11 (2019) 45199–45206. <https://doi.org/10.1021/acsami.9b15528>.
- [260] D. Zhang, S. Misra, L. Li, X. Wang, J. Jian, P. Lu, X. Gao, X. Sun, Z. Qi, M. Kalaswad, X. Zhang, H. Wang, Tunable Optical Properties in Self-Assembled Oxide-Metal Hybrid Thin Films via Au-Phase Geometry Control: From Nanopillars to Nanodisks, *Adv. Opt. Mater.* 8 (2020) 1–10. <https://doi.org/10.1002/adom.201901359>.
- [261] S. Kim, S. Park, S.Y. Kwon, W.T. Nichols, W. Il Park, Nanoscale metal pillar arrays on elastomeric substrates for surface-enhanced Raman spectroscopy platform, *Curr. Appl. Phys.* 15 (2015) 711–716. <https://doi.org/10.1016/j.cap.2015.03.019>.
- [262] K. Robbie, C. Shafai, M.J. Brett, Thin films with nanometer-scale pillar microstructure, *J. Mater. Res.* 14 (1999) 3158–3163. <https://doi.org/10.1557/JMR.1999.0423>.
- [263] B. Zhang, J. Huang, B.X. Rutherford, P. Lu, S. Misra, M. Kalaswad, Z. He, X. Gao, X. Sun, L. Li, H. Wang, Tunable, Room Temperature Multiferroic Fe-BaTiO₃ Vertically Aligned Nanocomposite with Perpendicular Magnetic Anisotropy, *Mater. Today Nano.* (2020) 100083. <https://doi.org/10.1016/j.mtnano.2020.100083>.

- [264] A. Tymoczko, M. Kamp, O. Prymak, C. Rehbock, J. Jakobi, U. Schürmann, L. Kienle, S. Barcikowski, How the crystal structure and phase segregation of Au-Fe alloy nanoparticles are ruled by the molar fraction and size, *Nanoscale*. 10 (2018) 16434–16437. <https://doi.org/10.1039/c8nr03962c>.

VITA

BRUCE ZHANG

Ph. D. Candidate

Department of Electrical and Computer Engineering
Purdue University

https://scholar.google.com/citations?user=4CZg_jUAAAAJ&hl=en

Education

Ph. D. Electrical and Computer Engineering, Purdue University August 2020
Thesis: Integration of Ferromagnetic Metals in Vertically Aligned Nanostructures for Spintronics
Specialization: Thin Film Fabrication and Characterization
Principle Advisor: Dr. Haiyan Wang

M. Eng. Electrical and Computer Engineering, Texas A&M University 2016

B. S. Electrical Engineering and Computer Science, University of California at Berkeley, 2014.

Fields of Interest

Ceramic Thin Films, Metal-Ceramic Nanocomposite Films, Material Property Characterization, Pulsed Laser Deposition, Ferromagnetic Thin Films, Spintronics, Tunnel Junctions, Vertically Aligned Nanocomposites.

Professional Memberships

American Ceramic Society, 2020 - Present

Publications and Presentations (21 papers with 90+ citations)

1. **Bruce Zhang**, Matais Kalaswad, Bethany X. Rutherford, Shikhar Misra, Zhihao He, Haohan Wang, Asley E. Wissel, Xiashan Xu, and Haiyan Wang. *Au-Encapsulated Fe Nanorods in Oxide Matrix with Tunable Magneto-Optic Coupling Properties*, Submitted, 2020.
2. **Bruce Zhang**, J. Huang, B. Rutherford, P. Lu, S. Misra, M. Kalaswad, Z. He, X. Gao, X. Sun, L. Li and H. Wang, *Mater. Today Nano*, 2020, 100083.
3. **Bruce Zhang**, Jijie Huang, Jie Jian, Leigang Li, Shikhar Misra, Xing Sun, and Haiyan Wang. *Tunable Coercive Field of Co-BZO Vertical Aligned Nanocomposites for Memory Devices Integration. Nanoscale Advances*, **1**, 4450-4458, 2019.
4. **Bruce Zhang**, Meng Fan, Leigang Li, Jie Jian, Jijie Huang, Han Wang, Matias Kalaswad, and Haiyan Wang. *Tunable magnetic anisotropy of self-assembled Fe nanostructures within a La0.5Sr0.5FeO3 matrix. Applied Physics Letters*, **112**, 013104, 2018.

5. **Bruce Zhang**, Laszlo Bela Kish, and Claes-Göran Granqvist. *Drawing from hats by noise-based logic*. **International Journal of Parallel, Emergent and Distributed Systems**, **32**, 244–251, 2017.
6. Xin Li Phuah, Han Wang, **Bruce Zhang**, Jaehun Cho, Xinghang Zhang, and Haiyan Wang. *Ceramic material processing towards future space habitat: Electric current-assisted sintering of lunar regolith simulant*. **Materials Letters**, Submitted, 2020.
7. Bethany Rutherford, **Bruce Zhang**, Xuejing Wang, Xing Sun, Zhimin Qi, Han Wang, and Haiyan Wang. *Strain effects on the growth of $\text{La}_{0.7}\text{Sr}_{0.3}\text{MnO}_3$ (LSMO) – NiO Nanocomposite Thin Films via Substrate Control*. **ACS Omega**, Submitted, 2020.
8. Binod Paudel, **Bruce Zhang**, Yogesh Sharma, Kyeong Tae Kang, H. Nakotte, Haiyan Wang, and Aiping Chen. *Anisotropic domain and antiferrodistortive-transition controlled magnetization in epitaxial manganite films on vicinal SrTiO_3 substrates*. **Appl. Phys. Letters**, Submitted, 2020.
9. Kyeong Tae Kang, **Bruce Zhang**, Yogesh Sharma, Binod Paudel, Haiyan Wang, Paul Dowden, and Aiping Chen. *Substrate oxygen sponge effect: a new parameter for epitaxial thin film growth*. **Adv. Mater.** Submitted, 2020.
10. Matias Kalaswad, **Bruce Zhang**, Xuejing Wang, Han Wang, Xingyao Gao, and Haiyan Wang. *Integration of highly anisotropic multiferroic BaTiO_3 -Fe nanocomposite thin films on Si towards device applications*. **Nanoscale Advances**, Submitted, 2020.
11. Leigang Li, Jianli Cheng, Hua Wang, Jijie Huang, Xingyao Gao, Xuejing Wang, Shikhar Misra, **Bruce Zhang**, Jie Jian, Aiping Chen, Ping Lu, Xiaofeng Qian, Kesong Yang and Haiyan Wang. *Interfacial Engineering Enabled Novel Bi-Based Layered Oxide Supercells with Modulated Microstructures and Tunable Physical Properties*. **Crystal Growth and Design**, **19**, 7088–7095, 2019.
12. Jijie Huang, Han Wang, Hua Wang, **Bruce Zhang**, Xiaofeng Qian and Haiyan Wang. *Superconducting Iron Chalcogenide Thin Films Integrated on Flexible Mica Substrates*. **IEEE Transactions of Applied Superconductors**, **29**, 1–4, 2019.
13. Aiping Chen, Zach Harrell, Ping Lu, Erik Enriquez, Leigang Li, **Bruce Zhang**, Paul Dowden, Chonglin Chen, Haiyan Wang, Judith L. MacManus-Driscoll and Quanxi Jia. *Strain Enhanced Functionality in a Bottom-Up Approach Enabled 3D Super-Nanocomposites*. **Advanced Functional Materials**, **1900442**, 1–8, 2019.
14. L. Li, P. Boullay, J. Cheng, P. Lu, X. Wang, G. Steciuk, J. Huang, J. Jian, X. Gao, **B. Zhang**, S. Misra, X. Zhang, K. Yang and H. Wang. *Self-assembled two-dimensional layered oxide supercells with modulated layer stacking and tunable physical properties*. **Mater. Today Nano**, **6**, 100037, 2019.

15. Jijie Huang, Zhimin Qi, Leigang Li, Han Wang, Sichuang Xue, **Bruce Zhang**, Xinghang Zhang, and Haiyan Wang. *Self-Assembled Vertically Aligned Ni Nanopillars in CeO₂ with Anisotropic Magnetic and Transport Properties for Energy Applications*. **Nanoscale**, **10**, 17182–17188, 2018.
16. Chaewoon Park, Rui Wu, Ping Lu, Hui Zhao, Jinbo Yang, **Bruce Zhang**, Weiwei Li, Chao Yun, Haiyan Wang, Judith L MacManus-Driscoll, and Seungho Cho. *Use of Mesoscopic Host Matrix to Induce Ferrimagnetism in Antiferromagnetic Spinel Oxide*. **Advanced Functional Materials**, 2018.
17. Meng Fan, Han Wang, Shikhar Misra, **Bruce Zhang**, Zhimin Qi, Xing Sun, Jijie Huang, and Haiyan Wang. *Microstructure, magnetic and magnetoresistance properties of La_{0.7}Sr_{0.3}MnO₃: CuO nanocomposite thin films*. **ACS applied materials & interfaces**, 2018.
18. Tiening Jin, Leigang Li, **Bruce Zhang**, Hao-Yu Greg Lin, Haiyan Wang, and Pao Tai Lin. *Real-Time and Label-Free Chemical Sensor-on-a-chip using Monolithic Si-on-BaTiO₃ Mid-Infrared waveguides*. **Scientific reports**, **7**, 5836, 2017.
19. Tiening Jin, Leigang Li, **Bruce Zhang**, Hao-Yu Greg Lin, Haiyan Wang, and Pao Tai Lin. *Monolithic Mid-Infrared Integrated Photonics Using Silicon-on-Epitaxial Barium Titanate Thin Films*. **ACS applied materials & interfaces**, **9**, 21848–21855, 2017.
20. Meng Fan, **Bruce Zhang**, Han Wang, Jie Jian, Xing Sun, Jijie Huang, Leigang Li, Xinghang Zhang, and Haiyan Wang. *Self-Organized Epitaxial Vertically Aligned Nanocomposites with Long-Range Ordering Enabled by Substrate Nanotemplating*. **Advanced Materials**, **29**, 2017.
21. Lazar L. Kish, **Bruce Zhang**, and Laszlo B. Kish. *Cracking the Liu key exchange protocol in its most secure state with Lorentzian spectra*. **Fluctuation and Noise Letters**, **9**, 37–45, 2010.

Research Projects

Research Assistant, Electrical and Computer Engineering, Purdue University, 2017-Present

- Grew and characterized two phased metal-oxide nanocomposite films for perpendicular magnetic anisotropy applications.
- Collaborated with researchers from throughout Purdue and the United States to perform characterization on a wide range of materials.
- Worked on optimizing different growth parameters for the different films to tune both the nanostructure and physical properties of the film.

Graduate Research Assistant, Center for Integrated Nanotechnology, Los Alamos National Lab, 2019

- Created and adjusted different deposition recipes for a variety of oxide materials that all had interesting ferromagnetic or electrical properties.
- Performed analysis using a whole host of instruments such as x-ray diffraction and the physical property measuring system.
- Prepared different samples in the cross-sectional and plan view for TEM analysis and later performed the imaging using TEM, STEM, and EDX in a Talos.

Research Assistant, Electrical and Computer Engineering, Texas A&M University, 2015

- Worked on a stochastic computing scheme based on random fluctuations of noise that helped reduce the computing complexity of the classic problem of drawing numbers from a hat.
- Programmed a simulation to demonstrate the successful parallelization of the algorithm using Java.

Conference Presentation

1. **Bruce Zhang**, Jijie Huang, Jie Jian, Leigang Li, Shikhar Misra, Xing Sun, and Haiyan Wang (2020). *Tunable Coercive Field of Co-BZO Vertical Aligned Nanocomposites for Memory Devices Integration*. Electronic Materials and Application 2020. Orlando, Florida. Oral.

2. Jijie Huang, Han Wang, Hua Wang, **Bruce Zhang**, Xiaofeng Qian and Haiyan Wang (2018). *Superconducting Iron Chalcogenide Thin Films Integrated on Flexible Mica Substrates*. Applied Superconductivity Conference 2018. Seattle, Washington. Poster.

Teaching and Mentoring Experience

1. Mentored and trained younger Ph. D students in various characterization techniques and helped design their experiments and publish their results. Aided in planning and developing projects for undergraduates in a Research Experience for Undergraduates (REU) at Texas A&M and directed project for an individual high school student project that utilized magnetic concepts for energy applications.

2. Held additional teaching sessions for over 60 students and developed test and homework rubrics in an undergraduate course of ECE 370 (Electronic Properties of Materials) at Texas A&M. Helped to develop test and quiz rubrics for the graduate course of ECE 440/640 (Introduction of Thin Film Science and Technology) at Texas A&M and MSE 640 (Introduction of Thin Film Science and Technology) at Purdue University.

Industry Experience

Device Engineer Intern, Lattice Semiconductors, San Jose, CA, 2014

- Characterized the current-voltage graphs of the MOSFETs using micro-probing stations.
- Studied and utilized BSIM to model the behavior of MOSFETs
- Performed reliability tests on the different transistors.
- Analyzed and extracted transistor parameters from the current-voltage sweeps.
- Measured the different characteristics and established a model for transistors using HSPICE.

Relevant Skills

- Proficient in Pulsed Laser Deposition, X-ray diffraction, Transmission Electron Microscopy, Sputtering, Scanning Electron Microscopy, and Physical Property Measuring System.
- Experienced in Java, Python, LT Spice, HSpice, Basic, LabView, Matlab, OriginPro, Microsoft Office.
- Worked with micro-probe stations, parameter analyzing, oscilloscopes, power supplies, wave function generators, and DC power supplies

Awards

- Purdue Graduate Student Government Travel Grant – 2020.

